AALBORG UNIVERSITY

DENMARK

Measurement, modelling and performance evaluation of the MIMO radio channel

Kermoal, Jean Philippe

Link to publication from Aalborg University

Measurement, Modelling and Performance Evaluation of the MIMO Radio Channel

JEAN-PHILIPPE KERMOAL

A thesis submitted in partial fulfilment of the requirements of Aalborg University for the degree of Doctor of Philosophy

August 2002

Center for PersonKommunikation - Aalborg University, Denmark

Supervisors

Research Professor Dr. Preben Mogensen, Aalborg University
Assistant Research Professor Dr. Laurent Schumacher, Aalborg University
Professor Dr.Techn. Jørgen Bach Andersen, Aalborg University

Distributor:

Center for PersonKommunikation,
Department of Communication Technology,
Institute of Electronic Systems,
Aalborg University,
Niels Jernes Vej 12, A6
Aalborg 9220,
Denmark

Don't EVER give up!

(Courtesy from [1])

iv

Preface and Acknowledgement

Over the three years of the PhD duration, I have been lucky to work with some of the most renowned researchers in the wireless community. I am extremely glad that I had the opportunity to perform a PhD having a daily contact with industry through Nokia Networks. When thinking back of my first day in Denmark and the achievement of todays work, I am beholden to a long list of research colleagues, friends and family.

First of all, it is to be clear and repeated that this work is the result of a team effort. This means that without the help of my research colleagues, the work would never have reached the quality presented here. I would like to thank my supervisors, Preben E. Mogensen for his vision, support and encouragement during these 3 years; Laurent Schumacher for his knowledge in mathematics, his accuracy and organisation; Jørgen B. Andersen for the few but very valuable discussions. I would also like to thank Søren H. Jensen who was part of my supervision team in the first year.

A special acknowledgement goes to Frank Frederiksen (now Nokia Networks) who provided me with the excellent engineering of the RF equipment and the control of the slide during the measurement campaign. I shall remember his tremendous help in operating the system, the numerous discussions, and his valuable Danish lessons. During the measurement campaign I was also assisted by Troels B. Sørensen, Laurent Schumacher, and Albert A. Escapa. Their help is deeply acknowledged.

The staff of the Radio Frequency lab who worked in the shadow and provided quality equipment, especially Tage Andersen (now retired), Peter B. Jensen, Peter Dissing, and Steen L. Larsen should be acknowledged. Special thanks to the staff from the Mechanical Department, Klaus Kjær, Leif Jepsen, and Daniel Jørgensen who provided some of the hardware equipment. The radiation pattern measurements of the sleeve dipole antennas are to be credited to Gert F. Pedersen.

A special appreciation is to be given to Juha Ylitalo for arranging my stay at Nokia Networks in Oulu (Finland) and also to Esa Tiirola, for their guidance during my presence among them and their warm welcome to sauna-land.

I am grateful to my colleagues and former colleagues, Troels B. Sørensen, Klaus I. Pedersen (now Nokia Networks), Persefoni Kyritsi for the valuable technical and sci-

entific discussions. Special thanks to Troels B. Sørensen, Persefoni Kyritsi, Thomas Klingenbrunn (now Qualcomm), Frank Frederiksen, Laurent Schumacher, Preben E. Mogensen and Jørgen B. Andersen for their comments on the PhD manuscript. Not to forget Charles Hoequist for proof reading this thesis.

I can only confess that I learned a lot during these three years, but this PhD made me realise that learning is an endless process, like the danaïdes filling up endlessly their bottomless barrel.

Last but certainly not least, I want to thank my family for their support, and definitely not the least, Rikke, for her patience and understanding during the tough time despite my moody Breton temper. You all did believe in me and I thank you for that.

Jean Philippe Kermoal

August 2002

About the author

Jean Philippe Kermoal was born in Paris, France, in 1972. He graduated from the Institut Universitaire de Technologie (IUT) in Rennes, France, in 1994. Later he received his B.Sc. in 1995 and his M.Phil. degree in 1998 from the University of Glamorgan, South Wales, UK. After a brief career as a conscript officer in the French Air Force, he started his Ph.D. programme on multi-element transmit and receive antenna arrays for wireless communication systems at Aalborg University, Aalborg, Denmark in 1999. His research interests include MIMO radio channel characterization, adaptive antenna array, indoor and outdoor mobile communication propagation at microwave and millimetre-wave bands and broadband wireless systems. As of November 2002, he is working as a research engineer at Nokia Research Center, Helsinki, Finland.

Abstract

The performance of a new technology known as MIMO (Multi Input Multi Output), which involves a state-of-the-art combination of MEAs (Multi Element Array) and digital signal processing, is introduced to achieve higher spectral efficiency compared to the conventional SISO (Single Input Single Output) technology currently deployed in wireless communication systems.

The MIMO concept is defined as a radio link with M elements at one end and N elements at the other end. The main benefits of using the MIMO technology lie in the creation of $min(M, N)$ orthogonal information subchannels, the combination of Tx and Rx diversity, and the increased antenna gain. The performance of the MIMO technology is directly dependent on the correlation properties of the MIMO radio propagation channel and the BPR (Branch Power Ratio) at the MEAs.

This new technology is investigated in this thesis considering the radio propagation channel aspect. The objective of this study is to provide extensive MIMO measurement campaigns in order to extract propagation parameters from the measured data. Consequently, the propagation radio channel can be understood and the performance of the MIMO technology interpreted. In addition, the measured data are used to validate a stochastic MIMO radio channel model for both the spatial and the polarization domain in the narrowband condition. Another objective of this study is to evaluate the performance of the MIMO technology by means of theoretical Shannon capacity results derived from measured and simulated data.

Conclusions and recommendations are proposed in order to implement the MIMO technology in the most efficient manner. The MIMO technology works in two ways: the diversity MIMO and the information MIMO. At low SNRs, MIMO systems only provide a combined Tx and Rx diversity because only the strongest eigenvalue is excited whereas at high SNRs, the MIMO technology fully benefits from parallel subchannelling, i.e., more than one eigenvalue is excited. Therefore, the MIMO technology is very well suited for adding diversity gain and increasing coverage, however at the expense of not providing a high bit rate. When high peak data rate is desired, a combination of large numbers of decorrelated elements at both MEAs (with equal BPR) and large SNR is necessary.

Dansk Resumé

Der indføres en ny teknologi, som kaldes MIMO (Multi Input Multi Output). Den omfatter en meget avanceret kombination af MEAs (Multi Element Array) og digital signal-behandling, således at man opnår højere spektral-effektivitet sammenlignet med den konventionelle SISO (Single Input Single Output) teknologi, som nuværende radiokommunikationssystemer anvender.

MIMO konceptet defineres som et radiolink med M elementer i den ene ende og N elementer i den anden ende. Den største fordel ved at bruge MIMO teknologien ligger i at skabe min (M,N) uafhængige informations-underkanaler, kombinere Tx og Rx variationen og forøge antenne-forstærkningen. Udførelsen af MIMO teknologien afhænger direkte af korrelationsegenskaberne af MIMO radio-udbredelses-kanalen.

Denne nye teknologi undersøges her, hvor man tager radio-udbredelses-kanalen i betragtning. Formålet med denne undersøgelse er at sørge for en omfattende MIMO målekampagne, således at udbredelses-parametrene kan uddrages af de målte data. Følgelig kan radio-udbredelses-kanalen forstås, og potentialet af MIMO teknologien fortolkes. Desuden bruges de målte data til at efterprøve en stokastisk MIMO radiokanal model for både det rumlige og polariserings-domænet i smalbånds-tilfældet. Et andet formål med denne undersøgelse er at skaffe kapacitetsresultater fra målte og simulerede data. Konklusioner og anbefalinger er foreslået med henblik på at implementere MIMO teknologien på den mest effektive måde.

MIMO teknologien virker på to måder: diversity MIMO og information MIMO. Ved lave signal-til støj (SNR) niveauer giver MIMO systemer kun en kombineret Tx og Rx variation fordi det kun er den højeste eigenværdi der magnetiseres, og ved høje SNR-niveauer nyder MIMO teknologien fuldt ud gavn af den parallelle underkanal, dvs. alle eigenvædier magnetiseres. Derfor er MIMO teknologien meget velegnet til at tilføje variationsforøgelse og højere dækning, dog giver den ikke en høj bit hastighed. Med hensyn til "high peak" informationshastighed, er det nødvendigt at have en kombination af et stort antal dekorrelerede elementer ved begge MEA'er (med samme BPR) og et højt SNR-niveau.

Oversættelse: Jytte Larsen og Rikke Severinsen

Table of Contents

Notation

Notation and acronyms used in this thesis have been listed below for the reader's convenience. They are also defined in the thesis at their first occurence.

Acronyms

3GPP	3rd Generation Partnership Project
AAU	Aalborg University
ACTS	Advanced Communications Technologies and Services
AoA	Angle of Arrival
AS	Azimuth Spread
ASILUM	Advanced SIgnal processing schemes for Link capacity increase in UMts - IST European project
BLAST	Bell Laboratories Layered Space-Time
BPR	Branch Power Ratio
BS	Base Station
CDF	Cumulative Distribution Function
CPK	Center for PersonKommunikation
CSys	Cellular System Group
DoA	Direction of Arrival
DoD	Direction of Departure
EM	Expectation Maximization
EVD	EigenValue Decomposition
FDD	Frequency Division Duplex
FT	Fourier Transform
I-METRA	Intelligent Multi Element Transmit and Receive Antenna - IST European project
i.i.d	Independent, identically distributed
IR	Impulse Response
ISM	Industrial, Scientific, and Medical
IST	Information Society Technologies
LOS	Line-of-Sight

MEA   Multi Element Array
METRA   Multi Element Transmit and Receive Antenna - IST European project
MIMO   Multi Input Multi Output
MISO   Multiple Input Single Output
MS   Mobile Station
NB   NarrowBand
NLOS   Non-Line-of-Sight
PAS   Power Azimuth Spectrum
PDS   Power Delay Spectrum
RF   Radio Frequency
RMS   Root Mean Square
Rx   Receiver
SAGE   Space-Alternating Generalized EM
SATURN   Smart Antenna Technology in Universal bRoadband wireless Net-
                    works - IST European project
SIMO   Single Input Multiple Output
SISO   Single Input Single Output
SNR   Signal to Noise Ratio
std   Standard Deviation
SUNBEAM   Smart UNiversal BEAMforming - ACTS European Project
SVD   Singular Value Decomposition
TDD   Time Division Duplex
TSUNAMI II   Technology in Smart antennas for UNiversal Advanced Mobile In-
                    frastructure 2 - ACTS European Project
Tx   Transmitter
UMTS   Universal Mobile Telecommunications System
UPS   Un-interruptable Power Supply
WB   Wideband
WCDMA   Wideband Code Division Multiple Access
WLAN   Wireless Local Area Network
WSS   Wide Sense Stationarity
XPD   Cross-Polar Discrimination

Mathematical Operators

$.^{*}$ Complex conjugate operation
$[\cdot]^{H}$ Hermitian transpose operation
$[\cdot]^{T}$ Transpose operation
$\mathbf{E}[\cdot]$ Expectation over time (or distance)
$\equiv$ identical to
$\langle .,. \rangle$ Correlation coefficient operation
$\mathbf{Re}$ Returns the real part of the complex argument
$\otimes$ Kronecker product
$\overset{(u)}{=}$ Uniform power allocation scheme
$\overset{(w)}{=}$ Water-filling power allocation scheme

$\{.\}$	Set of variables
$det(.)$	Determinant
log_{10}	Logarithm base 10
log_2	Logarithm base 2
$M \times N$	M by N matrix dimension
$max(.)$	Return the maximum of the argument
$min(\cdot)$	Return the minimum of the argument
$Rank(\cdot)$	Return the rank of a matrix
$std(.)$	Return the standard deviation
$\mathbf{A} \times \mathbf{B}$	Element by element multiplication of the matrices $\mathbf{A}$ and $\mathbf{B}$

Symbols

$\alpha_{b2b}^{wb}(t, \tau_l)$	Measured back-to-back complex IR
$\alpha_{mn\ mean}^{wb}(\tau_l)$	Averaged of the measured complex IR
$\alpha_{mn}(t)$	Complex NB transmission coefficient
$\alpha_{mn}^{wb}(t, \tau_l)$	Measured complex IR between the mth and the nth MEA element
γ_k	kth eigenvalue
λ	Wavelength
λ_k	Normalized kth eigenvalue
Ω	Number of linear elements in the MEA along broadside
$\overline{X}$	mean operation of X
$\phi_m(t)$	Phase shift between the MEA elements m
ρ	Correlation coefficient
ρ_{cplx}	Correlation coefficient: Complex domain
ρ_{env}	Correlation coefficient: Magnitude (envelope) domain
ρ_{power}	Correlation coefficient: Power domain
ρ_P	Correlation coefficient: Polarization domain
$\rho_{R\&P\&S_{\Delta i}}$	Correlation coefficient: joint pattern-spatial-polarization domain
$\rho_{S_{\Delta i}\&P}$	Correlation coefficient: joint spatial-polarization domain
$\rho_{S_{\Delta i}}$	Correlation coefficient: spatial domain with a spatial distance Δi
σ	RMS delay spread
σ_k	kth Singular value
σ_n^2	Noise power
$\sigma_{[X\ dB]}$	RMS delay spread considering a $X\ dB$ threshold
$\sigma_{channel}$	RMS delay spread of the channel
σ_{system}	RMS delay spread of the measurement system
τ	Delay
τ_a	Average delay
τ_l	Delay value at index l
ζ	SNR
ζ_k	SNR per kth subchannel
$BW_{[3dB]}$	Half power beamwidth
C	Capacity normalized to the system bandwidth
d	Actual element separation

d_o	Spatial Nyquist criteria
f_o	Nyquist criteria
f_{max}	Highest frequency component in the signal
K	Number of parallel subchannels
k	Index of the parallel subchannel
M	Number of MEA elements at the BS
m	Index of MEA elements at the BS
N	Number of MEA elements at the MS
n	Index of MEA elements at the MS
$s_n(t)$	Transmitted signals
t	Time
$y_m(t)$	Received signals
$\mathbf{y}(t)$	Received signal vector
$\mathbf{H}$	NB MIMO channel transfer matrix
$\mathbf{R}$	Instantaneous correlation matrix
$\mathbf{s}(t)$	Transmitted vector signal
$\mathbf{U}$	Left unitary matrices
$\mathbf{u}$	Left singular vector
$\mathbf{V}$	Right unitary matrices
$\mathbf{v}$	Right singular vector
D	Effective aperture of the MEA
X,Y,Z	Euclidean coordinates
K-factor	Ricean factor

Units

b/s/Hz	bit per second per Hertz
cm/s	centimeter per second
Hz	Hertz
m	metre

Chapter 1

Introduction

In conventional communication systems, one antenna at the transmitter (Tx) and one at the receiver (Rx)—a so called SISO (Single Input Single Output) antenna system—creates a bottleneck in terms of capacity. Whatever the modulation scheme used, the coding strategy employed, or other system artifacts, the radio channel will always set the limit for the telecom engineers. This situation is rather critical in the current wireless communication market since the user demand for higher bit-rates is becoming stronger. For instance, the wireless Internet connection is the next step for the users to be connected to the web but keeping their freedom of movement. To increase the capacity of wireless systems, three possibilities are offered: more base stations (BS), more bandwidth, and/or higher spectral efficiency.

More BS involves the deployment of new cells which is a very onerous way of increasing the capacity. Also some believe that the answer to high bit data rates is in the millimetre wave frequency band because more bandwidth is available. This technology is still expensive and furthermore the actual wireless market today is between UMTS[1] system [2] and WLAN[2] [3] which are at microwave band, e.g., about 2 GHz for UMTS and the ISM (Industrial, Scientific, and Medical) frequency bands, i.e., 2 and 5 GHz, for WLAN technology. As a result, the use of higher frequencies is not the answer to the currently needed wireless systems.

The motivation of this PhD is to present the capacity performance of a new technology referred to as MIMO (Multi Input Multi Output), which involves a state-of-the-art combination of MEA (Multi Element Array) and digital signal processing so that higher spectral efficiency is achieved. Claude E. Shannon (1916-2001) derived a formula to describe the information theory capacity C normalized with respect to the bandwidth, for one transmission channel, expressed in $b/s/Hz$ as a function of the

---

[1]UMTS: Universal Mobile Telecommunications System
[2]WLAN: Wireless Local Area Network

signal to noise ratio (SNR), ζ , $C = log_2 \left(1 + \zeta\right)$ meaning that a 3 dB increase in SNR results in an enhancement of the capacity by 1 b/s/Hz.

In a single user scenario, the SNR is basically related to the thermal noise and one method to increase it and subsequently the capacity, is by increasing the Tx power. This solution is, however, not recommended not only for health reasons [4], due to the exposure to electromagnetic radiation, but also higher transmit power would require linear operation of power amplifiers in higher regime which is a difficult task for the hardware designer, and the heat dissipation due to a higher Tx power should also not be forgotten. In a cellular scenario the noise floor is due to the other users, usually higher than the thermal noise, and increasing the Tx power would not help increasing the capacity.

Another method to increase the capacity would be to improve the received SNR by using diversity techniques along with some optimum combining technique. For some years, the use of MEAs at the Rx, namely the fixed terminal, considering one single element at the Tx was the subject of a lot of research activity, [5], [6] among others, and was designated as SIMO (Single Input Multiple Output) system. Similarly at the Tx, the UMTS WCDMA[3] standards support transmit diversity using a single element at the Rx, which is equivalent to a MISO (Multiple Input Single Output) system [7].

The natural evolution of the SIMO and MISO technologies is to provide MEAs at both ends of the radio link, hence creating a MIMO system. Telatar [8] showed that a huge capacity gain compared to SISO can be achieved using the generalised form of the Shannon equation when considering MIMO technology. The benefit of using the MIMO technology lies in the creation of orthogonal information channels, the combination of Tx and Rx diversity and the increase in the antenna gain.

The objective of the PhD thesis is to document the three years of research related to the MIMO technology. The content is intended for engineers with an interest in multiple element antenna systems, therefore conclusions and recommendations are applicable for engineering system implementation. A preknowledge of the basic radio propagation characteristics and digital signal processing will ease the reading and understanding of the thesis. The ambition in writing the thesis is to keep its size to a readable thickness. The results presented in the manuscript are a selection of the most interesting and pertinent graphs. The most suitable set of measurements have been described and the rest disregarded.

---

[3] WCDMA: Wideband Code Division Multiple Access

1.1 Contribution to METRA and the 3GPP Standardisation

The PhD programme started in June 1999 and was finalised in August 2002 at CPK[4], Aalborg University (AAU). This study has been strongly connected to the IST[5] METRA (Multi Element Transmit and Receive Antenna) European project [9] since it started only few months before the launch of the METRA project. I also spent 5 months in the facilities of Nokia Networks in Oulu (Finland) as part of the PhD programme at the beginning of autumn/winter 2001.

The METRA consortium involved 5 industrial and academic partners:

① Vodafone Limited, a network supplier (Newbury, United Kingdom).

② Nokia Mobile Phone, a mobile phone manufacturer (Oulu, Finland).

③ Nokia Networks, a mobile network manufacturer (Oulu, Finland).

④ University Polytechnic of Catalunya (Barcelona, Spain).

⑤ Aalborg University (Aalborg, Denmark).

The AAU team, i.e., the CSys[6] group members of CPK involved in METRA, had been assigned the task of characterising the MIMO radio channel in a UMTS system perspective, meaning that these propagation measurements are bandwidth limited. AAU provided MIMO measurement data and a stochastic MIMO radio channel model for the other partners to carry out link and system level work.

One of the goals of the METRA project was to give input to standardisation bodies concerning the MIMO technology. During the year 2000, the MIMO technology was being discussed in the 3rd Generation Partnership Project (3GPP) and it was decided to present the AAU MIMO model with the Nokia label [10] [11]. 3GPP is a collaboration between a number of telecommunication standard bodies [12] set to produce global technical specifications for the 3rd generation wireless system. Under the influence of third parties some modifications were made to the AAU MIMO model to achieve consensus, but essentially the model remained intact [13].

The PhD programme was financially sponsored by three bodies

① The Faculty of Engineering and Science at AAU,

② Nokia Networks, and

---

[4]CPK: Center for PersonKommunikation
[5]IST: Information Society Technologies
[6]CSys: Cellular System

③ The European Commission through the METRA project and its follow up the IST I-METRA (Intelligent Multi Element Transmit and Receive Antenna) European project[14].

1.2 The Author's Contribution to the MIMO Work

This thesis documents three years of research related to the state-of-the-art MIMO technology. As acknowledged in the preface, the overall work is the result of a team effort. Nevertheless, below is mentioned what I believe to be my personal contributions to this MIMO work:

☞ The design of the dipole array antenna, the design and development of the dragon in Chapter 3.

☞ The organization of the logistic, location finding and the actual execution of the measurement campaign in Chapter 3.

☞ The characterization of the radio channel based on the measured data in Chapter 4.

☞ The empirical validation of the MIMO model in Chapter 5.

☞ The performance evaluation analysis based on the measured and simulated data in Chapter 6.

1.3 Publications

Some of the materials of this thesis have been published elsewhere as listed below.

The first publication was dedicated to the first MIMO measurement campaign, presented in Chapter 3, and some of the microcell capacity results from Chapter 6.

> J. P. Kermoal, P. E. Mogensen, S. H. Jensen, J. B. Andersen, F. Frederiksen, T. B. Sørensen and K. I. Pedersen, "Experimental Investigation of Multipath Richness for Multi-Element Transmit and Receive Antenna Arrays", *in Proc. Vehicular Technology Conf.*, Tokyo, Japan, May 2000, pp. 2004-2008.

The METRA preliminary results, i.e., measurement setup (Chapter 3), correlation coefficient analysis (Chapter 4) and capacity results (Chapter 6), were published in

> J. P. Kermoal, L. Schumacher, K. I. Pedersen and P. E. Mogensen, "Experimental Investigation of Correlation Properties of MIMO Radio Channels for Indoor Picocell Scenarios", *in Proc. Vehicular Technology Conf.*, Boston, USA, September 2000, pp. 14-21.

J. P. Kermoal, L. Schumacher, P. E. Mogensen, K. I. Pedersen and F. Frederiksen, "METRA: Experimental Investigation of MIMO Radio Channels for Indoor Picocell Scenarios", *in Proc. IST Mobile Summit*, Galway, Ireland, October 2000, pp. 509-514.

Some aspects of the polarization diversity treated in Chapter 4 and Chapter 6 especially when considered at the BS, were published in

J.P. Kermoal, L. Schumacher, F. Frederiksen and P.E. Mogensen, "Experimental Investigation of the Joint Spatial and Polarisation Diversity for MIMO Radio Channel", *in Proc. Wireless Personal Multimedia Communications Conf.*, Aalborg, Denmark, September 2001.

The validation of the model in the polarization domain, i.e., when polarization diversity technique is employed at both ends of the link, treated in Chapter 5, was published in

J.P. Kermoal, L. Schumacher, F. Frederiksen and P.E. Mogensen, "Polarization diversity in MIMO Radio Channels: Experimental Validation of a Stochastic Model and Performance Assessment", *in Proc. Vehicular Technology Conf.*, Atlantic City, USA, October 2001.

The experimental work and the validation of the MIMO model, treated in Chapter 3 and Chapter 5, was published in

J.P. Kermoal, L. Schumacher, K.I. Pedersen, P.E. Mogensen and F. Frederiksen, "A Stochastic MIMO Radio Channel Model with Experimental Validation", *IEEE J. Select. Areas Commun.*, Vol. 20, no. 6, pp. 1211-1226, August 2002.

I was also co-author of several published documents listed chronologically below

P.E. Mogensen, K.I. Pedersen, J.P. Kermoal and T.B. Sørensen, "Deliverable D411 - 2D Radio Channel Study", *ACTS SUNBEAM AC347*, July 1999, pp. 1-65.

K.I. Pedersen, J.B. Andersen, J.P. Kermoal and P.E. Mogensen, "A Stochastic Multiple-Input Multiple-Output Radio Channel Model for Evaluation of Space-Time Coding Algorithms", *in Proc. Vehicular Technology Conf.*, Boston, United States, September 2000, pp. 893-897.

L. Schumacher, K.I. Pedersen, J.P. Kermoal, P.E. Mogensen, "A Link-Level MIMO Radio Channel Simulator for Evaluation of Combined Transmit/Receive Diversity Concepts within the METRA Project", *in Proc. IST Mobile Summit*, Galway, Ireland, October 2000, pp. 515-520.

L. Schumacher, J.P. Kermoal, K.I. Pedersen and P.E. Mogensen, "Simulating Polarisation Diversity and Power Allocation in MIMO Channels", *in Proc. European Personal Mobile Communications Conf.*, Session 15, February 2001.

L. Schumacher, J.P. Kermoal, F. Frederiksen, K.I. Pedersen, A. Algans and P.E. Mogensen, "MIMO Channel Characterisation", *IST Project IST-1999-11729 METRA Deliverable 2*, February, 2001.

Javier R. Fonollosa, et.al., "The IST METRA Project", *IEEE Communications Magazine*, Vol. 40, no. 7, pp. 78-86, July 2002.

1.4   A Crowded MIMO Community

The purpose of this section is to give a broad overview of the activity in the MIMO technology field and present the main research teams who contributed to the MIMO work. For an accurate account of their work, the reader should consult the original papers. Further, this review is restricted to selected work related to MIMO radio propagation channel measurement and modelling, and therefore non-exhaustive. Finally, this section indicates the geographical location of the various research teams in Europe (Figure 1.1) as well as in North America (Figure 1.2).

At the beginning of the PhD programme in 1999, MIMO propagation measurement results and MIMO modelling were starting to be the focus of research teams world-wide. The theoretical work on space-time architecture by Telatar [8], Foschini [15], Raleigh and Cioffi [16] or on the array gain and capacity offered by the MIMO technology by Andersen [17], the laboratory results of the V-BLAST (Vertical-Bell Laboratories Layered Space-Time) concept [18] were among the available documents related to the MIMO technology at that time. MIMO capacity results were extracted from simulation and assuming totally decorrelated radio link, i.e., i.i.d. (independent, identically distributed), channels which is the optimal MIMO scenario, but not necessarily the most realistic in terms of radio channel propagation characteristics. Therefore, two basic questions came to mind; *What is the real behavior of the MIMO radio channel?*, and *How to model it?*

Rapidly, propagation measurement campaigns and modelling results from several academic or industrial research teams around the world virtually bloomed. A technical overview of the most recent MIMO publications on measurements and modelling has been published in [19].

1.4.1   MIMO Propagation Measurements

A table summarizing the different MIMO measurement campaigns has been taken from [19] and is presented in Table 1.1 to provide an overview of the different MIMO field-trials. The work described in this thesis is also reported in the table as [20]. These measurement campaigns, documented world-wide, varied with respect to 6 items:

☞ The type of polarization used—single or dual,

☞ The number of elements in the MEA topology,

☞ The spacing between the elements of the array antenna,

☞ The carrier frequency—UMTS or WLAN frequency band,

☞ The bandwidth of the system—NB or wideband (WB) system,

☞ The type of propagation environment, i.e. picocell, microcell and macrocell.

Pola-risation	Refer-ence	Set-up	Spacing		Car-rier	Band-width	Time reso-lution	Environment
			Tx [λ]	Tx [λ]	[GHz]	[MHz]	[ns]	
Single	[21]	$n \times 8$[7]	-	-	1.7	30	-	Outdoor micro- and macro-cells
	[22]	8×8	n.a.	0.5	5.2	120	15	LOS/NLOS indoor micro-cells
	[23]	$n \times 8$[8]	-	0.5	5.2	120	15	LOS/NLOS out-door
	[24]	3×21[9]	6	0.25	5.8	400	-	NLOS indoor
	[25]	8×8	0.5	0.5	5.2	120	-	LOS/NLOS indoor
	[26]	4×12	6	-	2	5	-	Outdoor urban
	[27]	4×12	1	-	2	5	-	Outdoor urban
	[28, p. 24]	4×4	3-7	1-3	0.9	35	11	Subway
	[28, p. 17]	17×9[10]	0.25	0.25	5.2	250	4	Indoor
						62.5	4	Outdoor
Dual	[20][11]	4×4	0.4	1.5	2.05	5	122	Outdoor-to-indoor micro-cells, indoor pico-cells
	[29]	4×4	0.5	20	1.9	0.03	-	Outdoor-to-outdoor and outdoor-to-indoor suburban
	[30]	12×15	0.5	0.5	1.95	0.03	-	Indoor
	[31]	16×64	0.718	-	2.154	-	33	Outdoor-to-indoor
	[32]	4×4	40	1	-	3.5	-	Urban/suburban, hilly areas
	[28, p. 27]	4×8	-	-	2	120	-	Urban outdoor

Table 1.1: Description of the MIMO measurement campaigns which have been reported in the literature (Source: [19]. The numbering of the references has been altered to fit the bibliography of this thesis)—List non-exhaustive.

In Europe, three projects were supported by the European Commission, METRA [9], SATURN [12] [33] and ASILUM[13] [34]. In the SATURN project, several partners reported propagation measurements: University of Bristol [35][36], France Telecom [37],

---

[7]Directional MEA at the transmitter

[8]Single moving antenna at the transmitter

[9]Single moving antennas at both connection terminations. SISO measurements post-processed to generate MIMO channels

[10]Single moving omni-directional antenna at the transmitter

[11]Second set-up

[12]SATURN: Smart Antenna Technology in Universal bRoadband wireless Networks

[13]ASILUM: Advanced SIgnal processing schemes for Link capacity increase in UMts

KTH Royal Institute of Technology [38]. For the ASILUM project, IMST GmBh was involved in the measurement campaign [39]. A summary of the measurement campaigns of these three European projects has been reported in [28] as part of a European cluster on adaptive antennas.

Further in Europe, joint efforts between different institutions like the Vienna University of Technology and Ilmenau University of Technology resulted in numerous contributions, [40] [41] among others. Helsinki University used their knowledge on angle of arrival estimation when they reported their MIMO results [31]. Also within AAU different teams have developed other MIMO measurement set-ups [42][43][44].

Figure 1.1: Academic and industrial research teams in Europe involved in the MIMO concept—List non-exhaustive.

In the USA, AT&T Bell laboratories were among the first to report propagation measurement results [29][45]. Later Lucent Technology presented propagation measurement results [46] and showed a special interest in the key-hole concept[47] with respect to the BLAST concept. Stanford University, with the support of Lucent Technology in the hardware measurement set-up, also reported some propagation measurement results [48][49]. Other institutes like Brigham Young University [50][51] provided measurement results. Also worth noting are industrial contributors like Agere [52] (a former Lucent technology division) and Arraycomm [53]. As summarized in [54], in the context of the 3GPP standardisation, Motorola [26] and Qualcomm [55] were
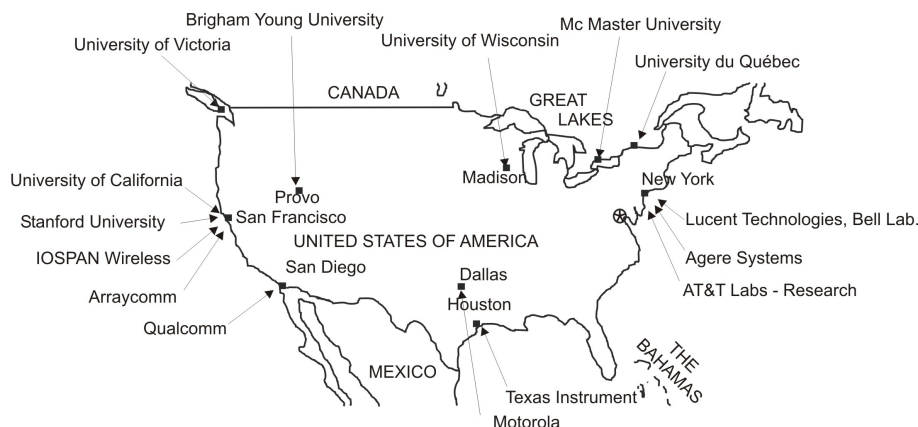
Figure 1.2: Academic and industrial research teams in the USA and Canada involved in the MIMO concept—List non-exhaustive.

also involved in MIMO propagation measurements.

In Japan, a MIMO channel sounder was reported in [56]. It is to be noted that due to the constant growth of the MIMO community it is difficult, as of this writing, to provide an exhaustive list.

1.4.2 MIMO Modelling

In addition to the propagation measurement of the MIMO radio channel, different MIMO models have been proposed in the open literature and Table 1.2 provides a non-exhaustive list of these models. The mathematical framework for the stochastic MIMO radio channel model presented in this thesis was reported in [57].

Category	Nature	References
Deterministic	Double-Directional Channel	[23]
	Ray-tracing technique	[58][59][60]
Stochastic	Spatial or Geometrically based Parametric	[61][39][62][63][64][65] [66][67]
	Correlation-Based Models	$\left\{\begin{array}{l}[68][13][69][70][71]\\ [72][73][47][74][57]\end{array}\right.$
	Scattering	[75][76]

Table 1.2: MIMO models reported in the literature—List non-exhaustive

In the context of 3GPP, at the beginning of 2001, a fantastic race took place among industrials often subcontracting academic institutes [77][10][62]. As of this writing, the outcome of the 3GPP discussions is a correlation based model being the result of a consensus between Lucent Technology, Nokia, Siemens and Ericsson [13].

In the early 2002, a spatial channel modelling AdHoc group started in connection with the third generation partnership project 2 (3GPP2) [78] where new discussions on MIMO channel modelling were initiated. As of this writing, the result of the discussions has not been finalised.

1.5   Outline of the Thesis

Chapter 2 presents the technical as well as the theoretical background on the efficiency of the MIMO system compared to the SISO system. The eigenvalues are presented as a quantitative approach to the parallel subchannelling concept along with capacity formula derived for the MIMO technology. Definitions of correlation coefficient, and branch power ratio (BPR) are presented. Finally, a glossary of the main terminology used in this thesis is provided.

Chapter 3 explains the measurement campaigns undertaken during the PhD programme. Two measurement set-ups which were employed to characterise the MIMO radio channel are presented. Also covered is a description of the investigated environments along with pictures taken during the measurement campaigns.

Chapter 4 addresses the characterization of the radio channel. This chapter presents the analysis of the measured data with respect to SISO and SIMO antenna topologies in order to understand the propagation properties of the radio channel. It includes the study of the statistical distribution in terms of the Ricean *K-factor* and a characterisation of the direction of arrival (DoA). A detailed analysis of the power correlation coefficient is performed so that the performance of the MIMO technology developed later in the thesis can be explained. Finally, several measured paths are selected and their properties listed so they can be used as reference scenarios in the rest of the thesis.

Chapter 5 describes the model developed by the CSys team with an emphasis on its empirical validation. The validation was based on the comparison between measured and simulated eigenvalue results; the simulated results are being based on the characterisation of the measured environment.

Chapter 6 provides theoretical Shannon capacity results, where two power allocation strategies are compared, for different types of environments, using different diversity techniques and antenna setups. The impact of the BPR at the MEAs on the MIMO technology performance is also addressed. Conclusions and recommendations are presented assuming a single-user scenario.

Finally, **Chapter 7** presents a summary of the concluding remarks made in the previous chapters and discusses future research topics.

Chapter 2

General Background Information

2.1 Introduction

The purpose of this chapter is to provide a basic understanding of the MIMO technology, necessary for the reading of the thesis, with a special emphasis on antenna array and digital signal processing. At first, a general description of the MIMO structure is given. The concept of parallel subchannelling is then introduced by mean of eigenanalysis, followed by its engineering interpretation. The antenna and diversity gains are also discussed in the context of MIMO technology.

The major motivation for the increasing interest in the MIMO technology, i.e., the capacity aspect, is discussed versus the capacity offered by conventional SISO technologies. This introduces two different power allocation schemes; the water-filling and the uniform power allocation strategy.

The correlation coefficient, which has a major influence in relation to the MIMO technology, is also defined in this chapter; it is used extensively throughout the thesis. Another important aspect to consider in the MIMO technology is the BPR thereby its definition in this chapter.

Finally a mini-glossary gathering the different MIMO propagation terminologies used in this thesis is presented.

2.2 General MIMO Structure

The MIMO concept is defined, throughout this thesis, as a radio link with M elements at the BS and N elements at the mobile station (MS) as pictured in Figure 2.1. For uplink the Tx is at the MS and the Rx at the BS while for downlink, the roles are reversed.

In this thesis, the actual role (Tx/Rx) of the MS and the BS is not important with regard to the conclusion made on the MIMO technology. The distinction is only needed to be coherent with the measurement equipment presented later in Chapter 3.

The term *element* is used instead of *antenna* to avoid potential confusion when dealing with polarization diversity since sometimes an antenna can be dual polarized with two elements as presented in Chapter 3.
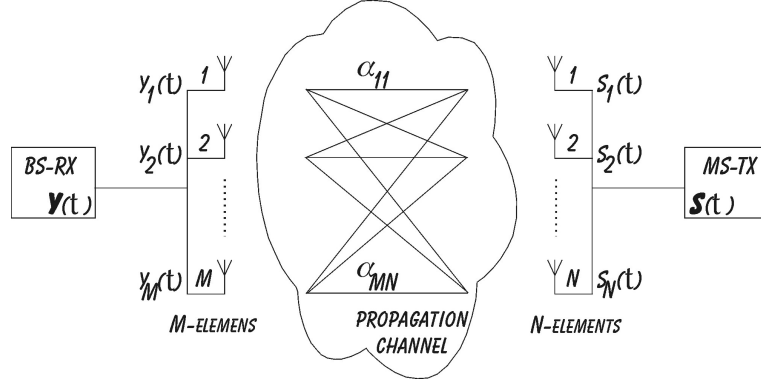

Figure 2.1: Two antenna arrays in a scattering environment. Representation of an uplink situation.

The received signal vector $\mathbf{y}(t)$ at the BS antenna array is denoted by

$$\mathbf{y}(t) = [y_1(t), y_2(t), \ldots, y_M(t)]^T \ , \tag{2.1}$$

where $y_m(t)$ is the signal at the mth antenna element and $[\cdot]^T$ denotes the transpose operation. Similarly, the transmitted signals at the MS, $s_n(t)$, define the vector $\mathbf{s}(t)$

$$\mathbf{s}(t) = [s_1(t), s_2(t), \ldots, s_N(t)]^T \ . \tag{2.2}$$

The vectors $\mathbf{y}(t)$ and $\mathbf{s}(t)$ are related by the following expression

$$\mathbf{y}(t) = \mathbf{H}(t)\mathbf{s}(t) + \mathbf{n}(t) \ , \tag{2.3}$$

where $\mathbf{n}(t)$ is additive white Gaussian noise and $\mathbf{H}(t) \in \mathbb{C}^{M \times N}$ is the instantaneous narrowband (NB) MIMO radio channel matrix. $\mathbf{H}(t)$ describes the connections between the MS and the BS and can be expressed as

$$\mathbf{H}(t) = \begin{bmatrix} \alpha_{11}(t) & \alpha_{12}(t) & \cdots & \alpha_{1N}(t) \\ \alpha_{21}(t) & \alpha_{22}(t) & \cdots & \alpha_{2N}(t) \\ \vdots & \vdots & \ddots & \vdots \\ \alpha_{M1}(t) & \alpha_{M2}(t) & \cdots & \alpha_{MN}(t) \end{bmatrix} \tag{2.4}$$

where $\alpha_{mn}(t)$ is the complex NB transmission coefficient from element n at the MS to element m at the BS.

The term "instantaneous" refers to a snap-shot of the radio propagation channel. In the context of mobile measurement, one snap-shot is equivalent to one sample of the recorded multipath in time (or distance). In the rest of the thesis, in order to keep the reading simple, the explicit time dependency (t) of $\mathbf{H}(t)$ and $\alpha_{mn}(t)$ is dropped.

2.3 The Eigenanalysis Method and Interpretation

The motivation for deploying MIMO technology in wireless systems is the possibility to achieve orthogonal subchannels between the two ends of the path in a rich scattering environment and subsequently to increase the offered capacity. The concept of orthogonality emphasizes the strength of the MIMO system since it indicates that these multiple channels are independent from each other. The MIMO technology is also beneficial in increasing the antenna gain and in providing combined Tx/Rx diversity.

Mathematically, the number of independent subchannels between two terminals can be estimated by using the singular value decomposition (SVD) of the matrix $\mathbf{H}$ or the eigenvalue decomposition (EVD)[17] of the instantaneous correlation matrix $\mathbf{R}$ defined as

$$\mathbf{R} = \mathbf{H}\mathbf{H}^H \text{ or } \mathbf{R} = \mathbf{H}^H\mathbf{H} \tag{2.5}$$

where $[\cdot]^H$ represents Hermitian transposition, i.e. the transpose conjugate.

The derivation of the parallel independent channels is summarized below where $\mathbf{U}$ and $\mathbf{V}$ are unitary matrices, $\mathbf{\Sigma}$ and $\mathbf{\Gamma}$ are diagonal matrices and $\mathbf{u}$ and $\mathbf{v}$ are the left and right singular vectors, respectively. There is an important relationship between the SVD of $\mathbf{H}$ and the EVD of $\mathbf{R}$ such that $\sigma_k^2 = \gamma_k$ where σ_k is the kth singular value and γ_k is the kth eigenvalue and where K is the the maximum number of eigenvalue as defined later in (2.15). $\mathbf{\Gamma}_{ij}$ denotes the elements of the matrix $\mathbf{\Gamma}$.

$$\boxed{\text{SVD}} \qquad\qquad\qquad \boxed{\text{EVD}}$$
$$\downarrow \qquad\qquad\qquad\qquad \downarrow$$

$$\mathbf{H} = \mathbf{U}\mathbf{\Sigma}\mathbf{V}^H \quad (2.6) \quad \Big| \quad \mathbf{H}\mathbf{H}^H = \mathbf{U}\mathbf{\Gamma}\mathbf{U}^H \text{ or } \mathbf{H}^H\mathbf{H} = \mathbf{V}\mathbf{\Gamma}\mathbf{V}^H \quad (2.7)$$

$$\mathbf{\Gamma}_{ij} = \mathbf{\Sigma}_{ij}^2$$

where $\qquad\qquad\qquad\qquad$ where

$$\mathbf{\Sigma} = diag(\sigma_1, ..., \sigma_K) \quad (2.8) \quad \Big| \quad \mathbf{\Gamma} = diag(\gamma_1, ..., \gamma_K) \quad (2.9)$$

$$\sigma_1 \geq \sigma_2 \geq ... \geq \sigma_K \geq 0 \quad (2.10) \quad \Big| \quad \gamma_1 \geq \gamma_2 \geq ... \geq \gamma_K \geq 0 \quad (2.11)$$

with $\qquad\qquad\qquad\qquad\qquad$ with

$$\searrow \qquad\qquad\qquad\qquad \swarrow$$

$$\mathbf{U} = [\mathbf{u}_1, ..., \mathbf{u}_M] \in C^{M \times M} \quad (2.12)$$
$$\mathbf{V} = [\mathbf{v}_1, ..., \mathbf{v}_N] \in C^{N \times N} \quad (2.13)$$

In the rest of the thesis, the normalized kth eigenvalue λ_k is used instead of γ_k. Unless otherwise mentioned, the normalization is made with respect to the mean power $|\alpha_{mn}|^2$ between all the single MS and the single BS element so that λ_k is defined as

$$\lambda_k = \frac{\gamma_k}{\mathbf{E}\left[\frac{1}{MN}\sum\limits_{m=1}^{M}\sum\limits_{n=1}^{N}|\alpha_{mn}|^2\right]} \ . \qquad (2.14)$$

where $\mathbf{E}[.]$ denotes the expectation over time (or distance). In order to keep the reading simple, the explicit term *normalized* is dropped.

Irrespective of the numerical method used to perform the analysis, a channel matrix $\mathbf{H}$ may offer K parallel subchannels with different power gains, λ_k, where

$$K = Rank(\mathbf{R}) \leq min(M, N) \ , \qquad (2.15)$$

and the functions $Rank(\cdot)$ and $min(\cdot)$ return the rank of a matrix and the minimum value of the arguments, respectively [17].
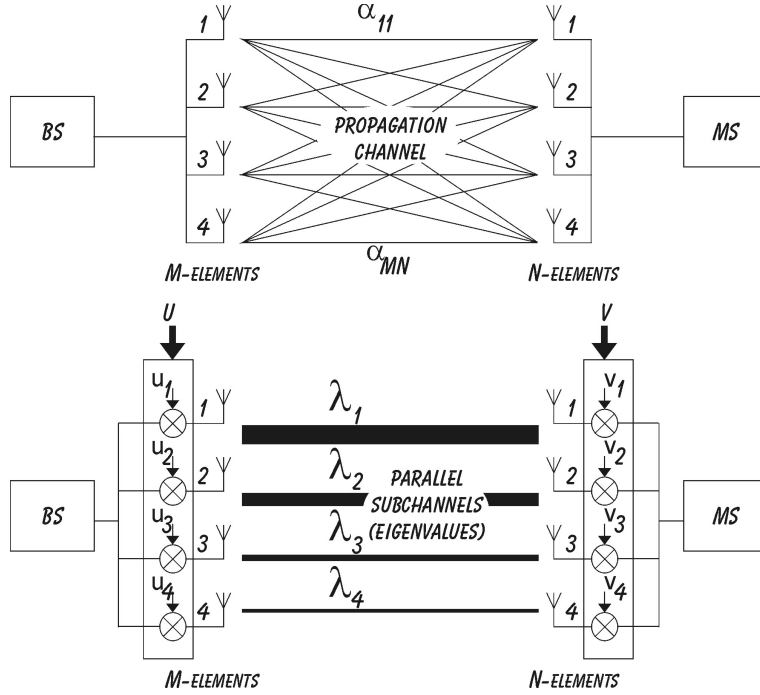

Figure 2.2: *Illustration of parallel subchannels for a 4×4 MIMO MEA topology.*

In engineering terms, $\mathbf{u}$ and $\mathbf{v}$ are also referred to as the weight vectors while the kth eigenvalue can be interpreted as the power gain of the kth orthogonal subchannel [17]. This is illustrated in Figure 2.2 for a 4×4 MIMO antenna topology. In such a configuration, $MN = 16$ radio links, α_{mn}, are created, but only 4 orthogonal subchannels

with power gain λ_1 to λ_4 are available. The difference in the thickness of the lines emphasizes the difference in gain of the parallel subchannels so that

$$\lambda_1 \geq \lambda_2 \geq ... \geq \lambda_K \geq 0. \tag{2.16}$$

To get the weight vectors, it is numerically more convenient to use the SVD of $\mathbf{H}$ while to obtain the eigenvalue it is easier to use the EVD. The EVD technique is the optimal way to extract the power gain of the MIMO subchannels. However, if this technique is to be optimal in a practical system implementation, the proper unitary matrix $\mathbf{U}$ and $\mathbf{V}$ must be applied at the respective ends of the link. Consequently, the EVD method is only useful when the channel is known, i.e., when the information of the radio channel is available at both the Tx and the Rx; a situation which can be assumed reasonable for time division duplex (TDD) systems while for frequency division duplex (FDD) systems significant feedback information is required.

2.4 The MIMO Propagation Scenarios

This section presents the different MIMO propagation scenarios which have been extensively studied to date in the MIMO literature. Before enumerating them, the notion of angular dispersive channels is needed at this stage of the thesis [79]. The angular power density distribution of the environment, i.e., the power at each angle of arrival, fully describes the angular spreading of the signal. This is also often referred to as the Power Azimuth Spectrum (PAS). It is shown in [80], that the Fourier transform of the spatial correlation function is a function of a three-dimensional parameter. In the case where the plane wave assumption holds, i.e. the impinging waves can be assumed to be plane, the spectrum of the spatial correlation function is restricted to the unit sphere (described in [80]) in the sense that it vanishes outside this sphere. When only the azimuth is considered, this sphere collapses into a circle. The restriction of the spectrum on the circle coincides with the PAS.

The Azimuth Spread (AS) is defined as the root second central moment of the PAS [5, p. 34]. The PAS is closely related to the spatial correlation at the MEA, i.e., depending on the spatial separation between the element of the MEA, a low AS is equivalent to a high spatial correlation coefficient and vice versa. Expressions of the spatial correlation function have been derived in the literature assuming that the PAS follows a cosine raised to an even integer [81], a Gaussian function [82], a uniform function [83], a Laplacean function [84] and the sine of the angle of arrival is shown to be Student's t-distributed as reported in [85]. A summary of these procedures to obtain theoretical correlation coefficients for uniform linear array in a MIMO concept has been reported in [86].

Three MIMO scenarios, each exhibiting different propagation characteristics, are listed below:

① Uncorrelated Scenario. In a rich scattering environment, the elements of $\mathbf{H}$ are

fully decorrelated. This corresponds to a full rank scenario where the maximum number eigenvalues is achieved.
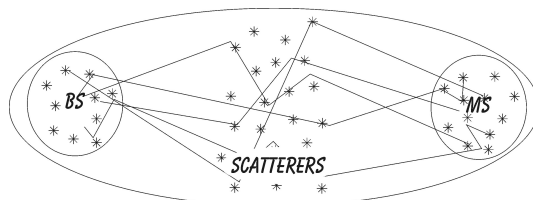
② Correlated scenario. In a situation with Line-of-Sight (LOS) or low AS at one or both ends of the radio link, the elements of **H** exhibit a certain correlation which results in a low rank scenario hence providing a lower number of eigenvalues.
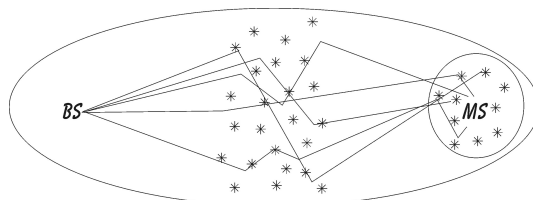
③ The pin-hole [71] or keyhole [87] is a scenario where the signals at the MEAs at both the Tx and Rx are decorrelated but the rank of **H** is one. This is analogue to a propagation scenario where the radio link is interrupted by an infinite metallic plate with a hole in the middle which is the only way for the signal to pass through, subsequently creating only one subchannel.
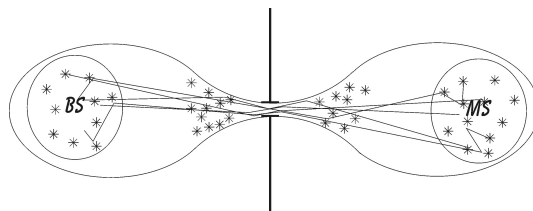
Practically, this would be the case when Tx and Rx are on opposite sides of a mountain and the signal can only pass through a tunnel. Another practical interpretation was reported in [47] where a diffraction-induced keyhole could appear. However, as conceived by the same authors, such a scenario may be very rare and difficult to encounter. Moreover, the pin-hole effect has also been considered for situations with large Tx-Rx separation, a situation where the low SNR would anyway degenerate MIMO capacity. In [88] and [46], the concept of keyhole embraces the three scenarios presented above where the first and third scenarios are extreme cases.

2.5 The Antenna and Diversity Gain Aspect

The enhancement in the radio link from the MIMO technology can be expressed in terms of antenna gain, diversity order and throughput performance. As already presented by Andersen in [89], the antenna gain and the diversity order obtained from a MIMO system depend on the scattering environment and especially on the AS at each end of the MIMO radio link. These findings are summarized in Table 2.1 since they outline MIMO performance very well for different scenarios. In Table 2.1, the antenna radiation pattern of each element of the MEA is assumed isotropic and the mean gain $\boxed{!}$ is the strongest eigenvalue λ_1.

AS at the MS	AS at the BS		Scenario	Mean gain	Diversity order
low	low	$\Rightarrow$	correlated	MN	1
low	high	$\Rightarrow$	correlated	MN	M
high	low	$\Rightarrow$	correlated	MN	N
high	high	$\Rightarrow$	decorrelated	$\sim (\sqrt{M} + \sqrt{N})^2$	MN

Table 2.1: *Antenna gain and diversity order in a MIMO context for different scenarios (Source: [89]).*

2.5.1 Temporal Illustration of the Eigenvalue

A quantitative description of the MIMO gain performance is the temporal representation of the eigenvalues. Figure 2.3 (i) presents the behavior of the eigenvalues derived from a measured 4×4 MIMO setup where the AS is high at both the BS and MS whereas Figure 2.3 (ii) presents a situation where the AS is low at the BS and high at the MS.

The behavior of the eigenvalues can be summarized in two items: they fluctuate with time and the strength of each λ_k strongly varies depending on the propagation scenario, i.e., correlated or uncorrelated.

2.5.2 Antenna Gain

Another method to present the eigenvalues is by using their cumulative distribution function (cdf). Throughout the rest of the thesis, unless otherwise mentioned, the cdf is computed over time. The logarithm of the cdf is shown to be coherent with the original eigenvalue representation reported in [17].

Figure 2.4 presents the empirical cdf of the normalized eigenvalues compared to a Rayleigh SISO channel. The graphs should read as follows. At the 10%[1] level a power gain of 19 dB is achieved using MIMO compared to a SISO set-up. The 10% cdf level is often used in this thesis, since it is a typical measure for system-level performance. The mean value of the strongest eigenvalue of Figure 2.4 is 11 dB which is in line with the value of 10 dB from [89] for a fully decorrelated 4×4 case.

[1]10% is equivalent to $log_{10}(0.1) = -0.1$
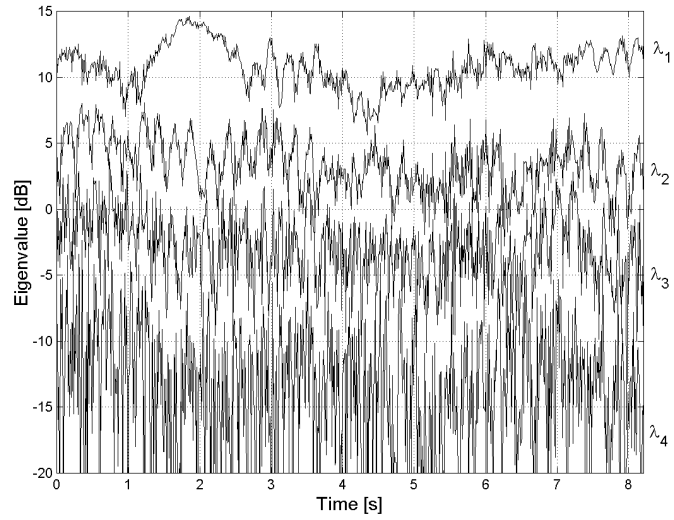
(i) Decorrelated scenario ⇒ AS-BS:high -MS:high.
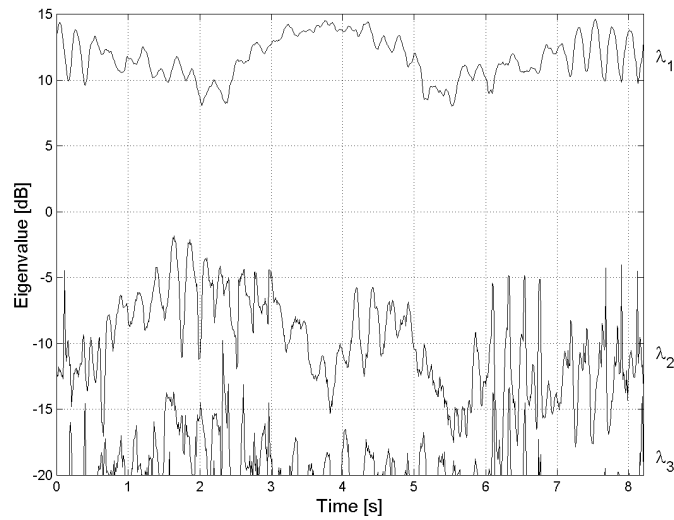
(ii) Correlated scenario ⇒ AS-BS:low -MS:high.

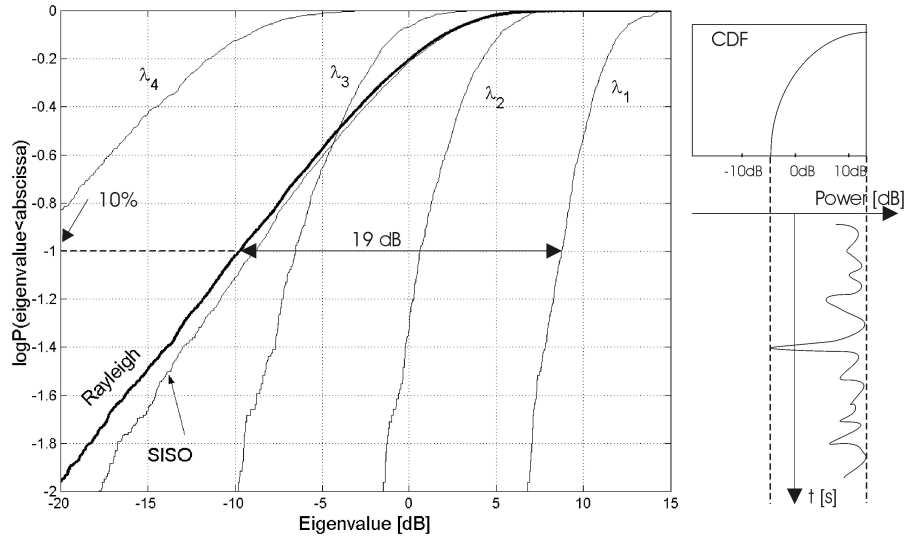Figure 2.3: Variation of the eigenvalues over time.

Figure 2.4: Cdf of the eigenvalues. The slope is an indication of the amplitude of the eigenvalue fluctuations. Same decorrelated scenario presented in Figure 2.3 (i).

The cdf representation is also very useful when interpreting the diversity performance in a MIMO system. The steepness of the slope of the cdf reflects the diversity order. The steeper the slope, the less amplitude of the fluctuation in the signal, i.e, the fades due to the multipath are less deep, and therefore a higher degree of diversity is obtained as shown in Figure 2.4.

2.5.3   Diversity Gain

Figure 2.5 illustrates the improvement in antenna gain and diversity order from a measured MIMO system for a correlated scenario, i.e., low AS at the BS and a high AS at the MS. Three different M×N antenna set-ups are compared: 1×1, 1×4 and 4×1. Recall the following notation:

$$\text{BS} \quad \rightarrow \quad \text{M} \quad \times \quad \text{N} \quad \leftarrow \quad \text{MS}$$

A simulated Rayleigh curve is plotted and compared to the measured 1×1 radio link suggesting that the 1×1 measured signal is Ricean distributed since its curve is steeper than the Rayleigh curve. Relative to this measured SISO case a gain of 6 dB at 10% level is achieved for a 4×1 set-up. This is the classical gain of $10log_{10}(M)$ with M=4 at the BS, i.e. no Rx diversity gain is obtained, the slope of the 4×1 is the same as

for the 1×1 situation.

However, the slope is steeper for a 1×4 topology, the diversity gain at the MS is added to the array gain, and 9 dB gain is achieved at 10% level. In the 4×1 case, the 4 antenna elements at the BS act as a single high gain antenna while in the 1×4 case the 4 antenna elements at the MS are uncorrelated and therefore they achieve both antenna gain and diversity.
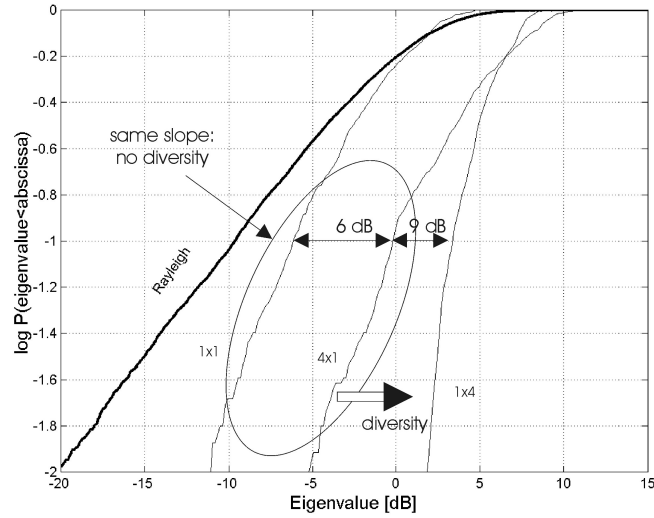

Figure 2.5: Empirical illustration of the antenna gain and the diversity gain for different spatial antenna array configuration set-ups for the correlated scenario. AS-BS:low -MS:high.

2.6   The Capacity Aspect

The concept of orthogonal subchannels is now understood. This permits to introduce the capacity concept that MIMO systems can offer compared to a conventional SISO system. This section defines the spectral efficiency of MIMO channels based on the channel capacity as defined in information theory [90][61]. This is the theoretical maximum amount of information that can be transmitted over a bandwidth limited channel for which error-free transmission is possible in the context of Gaussian channel [91, p. 652].

In real system implementation, the achievable capacity is limited due to coding, detection, constellation size among others [92], therefore the capacity results presented along the thesis are to be seen as upper bound values. This study is limited to a single-user scenario where two power allocation strategies are compared: the water-filling and the uniform power allocation strategies. The Shannon's formula for a SISO

radio channel is expressed as:

$$C = log_2 (1 + \zeta) \ , \tag{2.17}$$

recall from page 2, that ζ is the SNR.

For the MIMO technology, Telatar [8] presented the total Shannon's capacity, for uniform power allocation strategy, as

$$C = log_2 \left(det \left(\mathbf{I} + \mathbf{QH}^H \mathbf{H} \right) \right) \tag{2.18}$$

where $\mathbf{I}$ is the identity matrix, $\mathbf{Q}$ is the signal covariance matrix , $det(.)$ is the determinant and log_2 is the logarithm base 2. This formulation is often used by the MIMO community.

Equation (2.18) can be rewritten so as to emphasize the influence of the K parallel subchannels [17] and the total Shannon's capacity is defined as

$$C = \sum_{k=1}^{K} log_2(1 + \zeta_k) \tag{2.19}$$

where ζ_k is the SNR for the kth subchannel and is defined as

$$\zeta_k = \lambda_k \frac{P_k}{\sigma_n^2} \tag{2.20}$$

where P_k is the power assigned to the kth subchannel and σ_n^2 is the noise power. Hence, (2.19) can be rewritten as

$$C = \sum_{k=1}^{K} log_2(1 + \lambda_k \frac{P_k}{\sigma_n^2}) \ . \tag{2.21}$$

Depending on the power allocation scheme employed, the total transmitted power is distributed in a different manner between subchannels.

When considering the total capacity offered by the MIMO set-up, the total mean SNR per Rx antenna is defined as

$$SNR = \frac{\mathbf{E}[P_{Rx}]}{\sigma_n^2} = \frac{\mathbf{E}[P_{Tx}]}{\sigma_n^2} \tag{2.22}$$

where the time-averaged channel power gain is assumed 0 dB so that there is no loss in average between P_{Tx} and P_{Rx}.

2.6.1 Water-filling Power Allocation

When the channel is known, i.e., when the information of the radio channel is available at the Tx, it is possible to apply the EVD and the kth eigenvalue can be extracted.

Given the set of normalized eigenvalues $\{\lambda_k\}$, the power P_k allocated to each kth subchannel is determined so as to maximize capacity. This solution is known from Gallager's water filling theorem [17] in which each subchannel is filled up to a common level D defined as

$$\frac{1}{\lambda_1} + P_1 = \cdots = \frac{1}{\lambda_K} + P_K = D \ , \tag{2.23}$$

with a constraint on the input power such that

$$\sum_{k=1}^{K} P_k = P_{Tx} \ , \tag{2.24}$$

P_{Tx} is the total transmitted power. This means that the subchannel with the highest gain, i.e. the strongest eigenvalue, is allocated the largest fraction of power. In the case where $1/\lambda_k > D$, $P_k = 0$. Given (2.18) this is achievable when $\mathbf{Q}$ is diagonal and the optimal diagonal entries are computed from the water filling theorem.

Hence, (2.19) can be rewritten as

$$C \overset{(\mathrm{w})}{=} \sum_{k=1}^{K} log_2(1 + \lambda_k \frac{P_k}{\sigma_n^2}) \ , \tag{2.25}$$

where $\overset{(\mathrm{w})}{=}$ denotes the water-filling power allocation scheme.

2.6.2   Uniform Power Allocation Scheme

In the situation where the channel is unknown, i.e., when the information of the radio channel is not available at the Tx, the uniform distribution of the power is the most reasonable power allocation scheme to use. In practice, the total transmitted power P_{Tx} is equally split among the N elements of the array at the Tx [17] and is independent of λ_k so that

$$P_n = \frac{P_{Tx}}{N}, \quad \forall \ n = 1 \ldots N \ . \tag{2.26}$$

For simplicity in this thesis, it is assumed [61] that the Tx power is distributed evenly to the subchannels so that given (2.18), $\mathbf{Q}$ is diagonal and its entries are defined as

$$P_n = P_k. \tag{2.27}$$

Therefore, equation (2.19) can be rewritten as

$$C \overset{(\mathrm{u})}{=} \sum_{k=1}^{K} log_2(1 + \lambda_k \frac{P_n}{\sigma_n^2}) \tag{2.28}$$

where $\overset{(\mathrm{u})}{=}$ denotes the uniform power allocation scheme.

2.7 Correlation Definition

Up to now in this thesis (see pages 15, 17 and 19), the terms correlation or decorrelation have been largely used to emphasize the importance of the correlation properties between MEAs' element. This section defines the correlation coefficient which is addressed through this work. The basic statistical definition of the correlation coefficient ρ used in this thesis is given by

$$\rho = \langle a, b \rangle = \frac{\mathbf{E}[ab^*] - \mathbf{E}[a]\mathbf{E}[b^*]}{\sqrt{(\mathbf{E}[|a|^2] - |\mathbf{E}[a]|^2)(\mathbf{E}[|b|^2] - |\mathbf{E}[b]|^2)}} \qquad (2.29)$$

where $.^*$ and $\langle .,. \rangle$ are the complex conjugate and the correlation coefficient operations. Depending on the nature of both a and b, three different correlation coefficients can be defined: complex, envelope or power. The differences between the three correlation coefficient definition based on measured data is presented in Appendix G. Consider two complex variables x and y.

☞ Complex, $a = x$ and $b = y$, ρ_{cplx} :

$$\rho_{cplx} = \langle x, y \rangle \qquad (2.30)$$

☞ Envelope, $a = |x|$ and $b = |y|$, ρ_{env} :

$$\rho_{env} = \langle |x|, |y| \rangle \qquad (2.31)$$

☞ Power, $a = |x|^2$ and $b = |y|^2$, ρ_{pow} :

$$\rho_{pow} = \left\langle |x|^2, |y|^2 \right\rangle \qquad (2.32)$$

In the context of modelling, the complex correlation coefficient carries the full information (amplitude and phase) required to model properly the radio channel; this explains why the complex correlation coefficient is used in Chapter 5 where the MIMO radio channel modelling is treated.

The envelope and the power correlation coefficients, however, have a clearer engineering interpretation than the complex correlation coefficient. In the 1970-80s, the analysis of the correlation was often performed on an envelope correlation basis [81] [93] [82]. This choice was motivated by the limitations of the measurement system itself, since it could only provide the amplitude or the power of the measured signal and not its phase. Also, engineers found it easier to handle the power correlation coefficient rather than the envelope correlation coefficient as reported in [94] since typical values of $\rho_{pow} \leq 0.7$ [95, p. 309] or $\rho_{pow} \leq 0.5$ [96, p. 198] are sufficient to achieve significant diversity gain. Nevertheless, the concept of the complex correlation coefficient was already addressed theoretically in the late 1950s [97] and early 1960s [98]. It is shown in these references that the two definitions (2.30) and (2.32) are linked to each other by the relationship

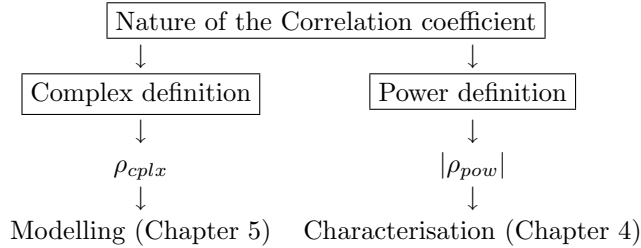$$\rho_{pow} = |\rho_{cplx}|^2 \,, \qquad (2.33)$$

for Rayleigh distributed signals [98] and

$$\rho_{pow} = \frac{|\rho_{cplx}|^2 + 2\mathbf{Re}\{\rho_{cplx}\}\sqrt{K_a K_b}}{\sqrt{(2K_a + 1)(2K_b + 1)}} \; , \tag{2.34}$$

for Ricean distributed signals [97] where $K_{a,b}$ are the *K-factors* of the complex signals a and b, and $\mathbf{Re}$ returns the real part of the complex argument. The definition in (2.32) for ρ_{pow} is restricted to the interval $[-1, 1]$ while ρ_{pow} in (2.33) is confined to $[0, 1]$. This discrepancy can be alleviated considering the fact that a correlation value of -1 is equivalent to a signal being totally correlated with another but shifted by π, like for a sine wave; for simplicity's sake in handling the measured data and comparing the correlation results with published work, the correlation coefficient analysis presented in Chapter 4 is based on the absolute power definition $|\rho_{pow}|$.

Studies on the envelope and power correlation coefficient corrupted by additive white Gaussian noise [99] indicate that for Rayleigh signals exhibiting a SNR lower than 20 dB, the correlation value is negatively biased and a corrective factor is needed. For Ricean signals, the degradation of correlation estimation is a second order function of both the SNR and the *K-factors*. The magnitude of the corrective factor is 0.05 when $10 \; dB \leq SNR \leq 20 \; dB$ for Rayleigh signals, 0.07 when $SNR \geq 20 \; dB$ and 0.25 when $SNR = 10 \; dB$ for Ricean signals of *K-factors*=5 dB. The need for correction was not necessary in this study since the majority of the SNRs achieved during the measurement campaigns were higher than 20 dB.

The difference in the nature of the correlation coefficient studied in different chapters of this thesis due to their applications is summarized below.

$$\boxed{\text{Nature of the Correlation coefficient}}$$
$$\downarrow \qquad\qquad\qquad\qquad \downarrow$$
$$\boxed{\text{Complex definition}} \qquad \boxed{\text{Power definition}}$$
$$\downarrow \qquad\qquad\qquad\qquad \downarrow$$
$$\rho_{cplx} \qquad\qquad\qquad |\rho_{pow}|$$
$$\downarrow \qquad\qquad\qquad\qquad \downarrow$$
$$\text{Modelling (Chapter 5)} \quad \text{Characterisation (Chapter 4)}$$

2.8   Branch Power Ratio

An important parameters to take into account when implementing the MIMO technology is the BPR. In this thesis the BPR is defined as the ratio between the powers P_n on the nth element's branches of the MEA.

$$BPR_{ij} = \frac{P_i}{P_j} \; , \tag{2.35}$$

Therefore an equal, or balanced, mean BPR ($\overline{BPR}$), i.e. the ratio between the mean powers, indicates that the average power on each branch is equal which can be written as

$$\overline{P_1} = \overline{P_2} = \ldots = \overline{P_N} \ , \tag{2.36}$$

$$\overline{BPR} \simeq 0 \ dB. \tag{2.37}$$

In this thesis, a $\overline{BPR} = 0.22 \ dB$ is considered equal. An unequal or unbalanced $\overline{BPR}$ means that the

$$\overline{P_1} \neq \ldots \neq \overline{P_N} \ , \tag{2.38}$$

$$\overline{BPR} \ll 0 \ dB. \tag{2.39}$$

Based on measured data, it is shown in this thesis that even though the correlation coefficient values are very low ($\rho \leq 0.2$), the MIMO technology is not optimal when the mean BPR is unequal as shown in Chapter 6. Unless otherwise mentioned all the MIMO results are presented considering an equal mean BPR.

2.9 Mini-glossary of MIMO Terminology

This section presents a mini-glossary of the MIMO propagation terminology applied in the rest of the thesis along with an illustration in Figure 2.6.
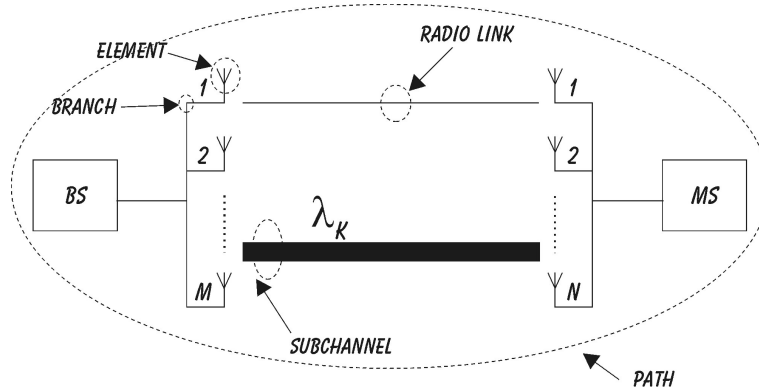

Figure 2.6: *Illustration of the MIMO propagation terminology applied in the rest of the thesis.*

Radio link A radio link is defined as the radio connection between two single elements of the two MEAs, also referred as α_{mn}.

Path A path is defined as the radio connection between the two MEAs of a MIMO configuration. In the case of measurement campaign, this is also equivalent to the pair (MS,BS) of a measurement location. In a path there are MN radio links.

Subchannel A subchannel, i.e. the eigenvalue, is equivalent to a virtual link between the two MEAs.

Branch A branch is the output of an element.

2.10   Summary and Interim Conclusion

This chapter presented the necessary background to fully understand the MIMO antenna technology. A general description of the MIMO structure, i.e. M antenna elements at the BS and N antenna elements at the MS, was given. The concept of parallel subchannelling was introduced by mean of eigenanalysis. Three MIMO propagation scenarios are identified: the uncorrelated scenario, the correlated scenario and the pin-hole effect.

The antenna and diversity gains in the context of MIMO technology was discussed. The normalized eigenvalues λ_k represent the power gain of the kth parallel subchannel. The antenna gain of the MIMO system is the strongest eigenvalue λ_1, and the slope of the cdf of the eigenvalues illustrates the degree of diversity in the MIMO system.

The major motivating factor in the MIMO technology is the high spectral efficiency offered compare to the conventional SISO technology. The theoretical capacity performance of MIMO technology was defined from the generalised Shannon equation and was shown to be related to the parallel subchannels. Definitions of two different power allocation schemes were presented, the water-filling and the uniform power allocation strategies.

The correlation coefficient, which has a major influence in relation to MIMO technology and which is used extensively throughout the thesis, was also defined in this chapter. In the context of modelling, the complex correlation coefficient is more suited and therefore used in Chapter 5, whereas the power correlation coefficient, providing a clearer engineering interpretation of the propagation analysis, is used in Chapter 4. The BPR which has also a major influence in relation to the performance of the MIMO technology has been defined in this chapter.

Finally a mini-glossary has been presented to gather the different MIMO propagation terminology used in this thesis.

Chapter 3

Experimental Work

3.1   Introduction

This chapter presents the measurement campaigns performed to obtain WB measurement data of the MIMO radio channel at UMTS band. These measurement campaigns benefited from the experience gained and the equipment developed during the two ACTS[1] TSUNAMI II[2] [100] and SUNBEAM[3] [101] projects. Some of the RF (Radio Frequency) equipment was reused for the MIMO investigations.

The first preliminary MIMO experiment was done as part of the European ACTS SUNBEAM project. Subsequently, the involvement in the IST European METRA project lead the PhD programme into a vast measurement field trial with the purpose of investigating the MIMO concept in real environments. This gave CPK the opportunity to be among the first research groups to provide measurement results of the MIMO radio propagation channel [102], [103].

The desired outcomes of the measurement campaigns were two-fold: (i) measured data to empirically validate the MIMO radio channel model developed during the course of the PhD programme, and (ii) the extraction of parameters from the measurement data to characterize the MIMO radio channel environments.

There are two main parts in this chapter. The first is a description of the two measurement systems, i.e., RF and mechanical hardware while the second is a description of the environments to be investigated in a MIMO perspective. In this chapter, pictures of the measurement campaign are presented to well illustrates the equipment and measurement set-up. For convenience in reading this chapter, Figure 3.18 to Figure 3.20

---

[1]ACTS: Advanced Communications Technologies and Services
[2]TSUNAMI II: Technology in Smart antennas for Universal Advanced Mobile Infrastructure 2 - ACTS European Project
[3]SUNBEAM: Smart Universal BEAMforming - ACTS European Project

are located at the end of the chapter due to their sizes.

3.2 The MIMO Experimental Equipment

Two MIMO measuring systems were developed and employed during the PhD programme. They are denoted according to the name of the project for which they were designed:

① SUNBEAM, and

② METRA measurement set-up.

   The experience gained from employing the SUNBEAM set-up was very useful for developing the METRA set-up so that the measured data could empirically validate the MIMO model.

This thesis reports mobile measurements, meaning that one MEA was mobile while the second MEA was stationary. In both set-ups, the mobile transmitter (Tx) was at the MS and the stationary receiver (Rx) was located at the BS. The differences in the two set-ups were: the motion of the Tx and the MEA topology employed. The SUNBEAM set-up is a SIMO configuration from which MIMO results can be derived using a synthetic MEA generated in a post-processing stage [102], whereas the METRA set-up is a MIMO set-up [103] from which a post-processing is applied so that to obtain the desired MIMO antenna topology to investigate different MEAs configuration. Table 3.1, on the next page, summarizes the difference in the measurement set-ups.

3.2.1 The RF Stand Alone Testbed

The equipment developed for TSUNAMI II and SUNBEAM was reused and the operating frequency band changed to provide UMTS experimental results. A thorough description of the testbed (i.e. Rx and Tx) is given in [104]. Part of the BS and the MS measuring equipment is shown in Figures 3.15 and 3.16 on page 45.

For the measurements reported in this thesis, the sounding signal that was transmitted by the Tx was a MSK-modulated carrier generated from a linear shift register sequence of length 127 chips and clocked at a chip rate of 4.096 Mcps. The channel sounding was performed within a window of 14.6 μs (120 samples), with a delay sampling resolution of 122 ns ($1/(2\times4.096)$) using an oversampling factor of 2, and an excess delay resolution of 1.5 chips, to obtain an estimate of the complex impulse response (IR). The IR was estimated by correlating with the known PN sequence. At the BS, the Rx consisted of eight duplicated hardware parallel receive branches. The phase of the system is locked on a Rubidium standard.

MIMO Measurements

SUNBEAM project	METRA project
↓	↓
SIMO	MIMO
↓	↓
Post-Processing	Post-Processing
↓	↓
MIMO	MIMO

Fc=1.71 GHz $\lambda/2$

20λ

synthesised approach

0.4λ Fc=2.05 GHz

switch approach

11.8λ

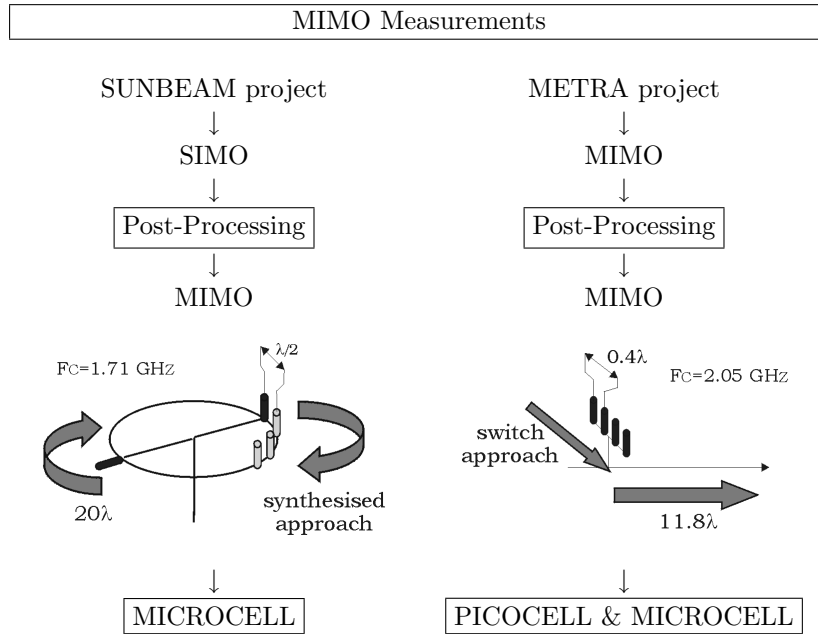| ↓	↓
MICROCELL	PICOCELL & MICROCELL

Table 3.1: Summary of the two measurement set-ups.

The mean SNR (averaged over time, MEA elements and paths per environment) observed during the measurement is summarized in Table 3.2 , on page 44. Note that the instantaneous SNR of the system is limited to 31 dB due to correlation noise from the PN sequences. The mean SNR was 31 dB in the majority of the measurement location, except for some rare occasions where it dropped to 10 dB.

The system was calibrated using back-to-back measurements to characterise the IR of the measurement testbed. The phase reference of each element was recorded such that angle of arrival (AoA) analyses could be performed. Before each measurement, the phase stability of the system and the stationarity of the channel were checked by visual inspection of a live display of the received complex impulse responses.

3.2.2 The SUNBEAM Measurement Set-up

At the MS (Tx), two standard dipole antennas diametrically opposite to each other, one vertically polarized and the other horizontally polarized, see Table 3.1, were mounted on a rotating bar to trace a circumferential distance of 20 wavelengths, λ (3.5 m) at a speed of 40.5 cm/s. The two dipoles were connected to a mechanical relay such that after one and a half revolutions, the RF signal was switched from the vertical to the horizontal dipole and therefore only one antenna was transmitting at a time. Then another one and a half revolution was performed. For this measurement campaign, the operating frequency was 1.71 GHz. The transmitted power was 38 dBm

at the output of the mechanical relay.

At the BS, 8 parallel Rxs were connected to the elements of a linear MEA with 4 dual polarized $\pm 45°$ elements and spaced by 0.45λ. From this SIMO experiment, a MIMO configuration was created in a post-processing analysis by selecting arbitrary antenna separations from the circumferential trace. In the thesis, a spatial separation of $0.5\ \lambda$ is considered.

The purposes of the measurement trials were

  ① the evaluation of the spatial correlation which exists between several elements of an MEA and also

  ② the extraction of realistic MIMO radio channelparameters for later analysis as part of the requirement of the METRA project.

The spatial correlation could easily be extracted from experimental results where a dipole would describe a circular motion, but this method would fail to provide any information on the AoA with respect to the Doppler spectrum, if a simple FT (Fourier Transform) routine would be applied on the full scan of the dipole at once, since the AoA is a function of the Doppler information of the recorded signal [95] and the AoA changes as the dipole rotates . Therefore, a linear motion of the MEA was preferred to a circular motion.

3.2.3   The METRA Measurement Set-up

The main part of the work reported in this thesis is related to the experimental equipment developed and utilized in the context of the METRA project.

After selecting the motion of the Tx MEA as being linear, a second alteration to the MEA set-up was decided. In the METRA project a switching approach was selected to create the MEA at the transmitting end although as evident from [19], [42] and [44], this technique was not the only one to characterise the MIMO radio propagation channel. With this switching approach, a common RF signal at the Tx, is sent to a 1-to-4 RF switch which selects one element at a time, with a switch time of 50 μs, thus providing isolation from the remaining elements. Since the switching was relatively fast, within 200 μs, it approximates a parallel transmission for low mobile speeds. Each of the four PN segments had a number associated which made it possible to distinguish from which element the sounding signal was transmitted. The carrier frequency was tuned to 2.05 GHz (UMTS band) and the transmitted power was 25 dBm measured after the switch. The low output power was sufficient for the indoor-to-outdoor experiment due to the short transmission paths and the subsequent low path loss.

3.2.3.1 Mechanical Hardware at the MS

For the METRA set-up, the MS consisted of two trolleys; one trolley contained all the RF hardware of the Tx, as shown in Figure 3.16 on page 45, and the other trolley, later referred to as the *dragon*, was equipped with a linear slide carrying the Tx MEA as shown in Figure 3.17 on page 46 and moved at a speed of 42.3 cm/s ($f_{doppler}$=2.9 Hz).

The two trolleys were connected by 10 m coaxial and control signal cables as shown in Figure 3.19 and Figure 3.20 on page 47. The use of a 10 m cable could be considered as a rather large radiator compared to the small antenna size (described in the next section) used during the measurement. The potential influence of this long coaxial cable could be thought as correlating the signal through leakage (therefore the use of bazooka ballon explained in Section 3.2.4). However, the analysis of the correlation coefficient of the measured radio channel data indicates a rather decorrelated behavior as shown later in this thesis. It can be therefore safely assumed that potential leakages from the coaxial cable has had no significant impact on the measurement set-up.

The purpose of using two trolleys was to reduce the influence of the voluminous RF equipment. The dragon exhibited low impact on the RF signal since the metallic parts of the linear slide were covered by a layer of microwave absorbers—therefore the resemblance to a dragon. It can be argued that the use of microwave absorbers has an intrusive influence on the environments, i.e. absorbing 'waves' that should have been there. This is correct, but considering a reflective system would create more scatterers in the measured environment than the environment itself and would provide a 'better' richness of the scatterers than the actual environment. The interest in using the absorbtive solution, is that it provides a 'worst' case scenario when the richness of the scatterers is to be investigated. The ideal solution would be to design a slide entirely composed of non-reflective materials. This is however a very expensive solution. A cheaper solution would be to lower down the slide to ground level so that the ground reflection is combined with the slide reflection, but this solution obliges the mast to be taller. An additional mechanical constraint would hence be introduced due to the jitter of the mast in motion. Considering all these electromagnetic and mechanical constraints, the use of microwave absorbers is a trade-off between the influence of the measurement equipment and the reflection from the ground being hidden by the microwave absorbers. Figure 3.1, graphically illustrates the positioning of the two trolleys during a measurement campaign.

Two main constraints on the mechanical hardware were to be considered: the vibration of the mast and the actual size of the dragon. The solution to these problems were:

① A slide driven by a plastic belt minimized the vibrations.

① The length of the slide had to be chosen according to the layout of the environment. For instance, the size of lifts and door frames, the presence of furniture, resulted in mechanical constraints and should fulfill the Wide-Sense Stationary (WSS) requirement when being used to record the radio channel.
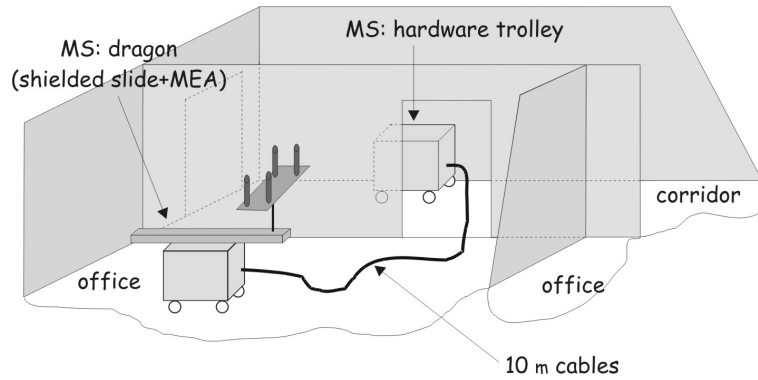
Figure 3.1: Representation of the measurement setup which reduces the influence from the metallic casing on the on the RF equipment.

WSS radio channels defined in Parsons [105], have the property that their fading statistics are invariant over a short interval of time. Some authors like [106] and [107] relate the WSS to the geometrical scatterers. They indicate that a spread or variation in the Doppler domain during the recording would indicate that scatterers would be illuminated and/or obstructed which would affect the stationarity of the recorded signal as illustrated in Figure 3.2. Therefore, as a rule of thumb, it can be assumed that the scatterers should be at a distance 10 times the distance travelled by the MS, which is equivalent to about 20 m in the present case. Therefore a slide which was too long would not be adequate considering the selected environments.
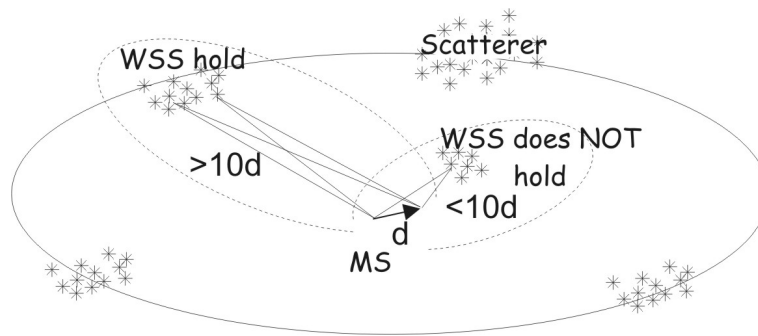
Figure 3.2: Illustration of the WSS condition. Here d is the travelled distance by the MS.

The length of the slide and the determination of the spatial correlation interact. Therefore, a Monte Carlo analysis of the power correlation coefficient with respect to the slide's length was undertaken. The actual size of the slide was dictated from the range of slide commercially available. The selection of the slides is determined by the results of the standard deviation (std) analysis performed on the power correlation coefficient between two uncorrelated Rayleigh channel which is computed over 1,000 realisations

for different slide lengths. As presented in Figure 3.3, a distance of 11.8λ exhibits a std of the power correlation coefficient lower than 0.09. This result is believed acceptable considering that a length much greater than 20λ to achieve a significantly lower std. Consequently, a slide of length 11.8λ, i.e., 1.7 m was selected.
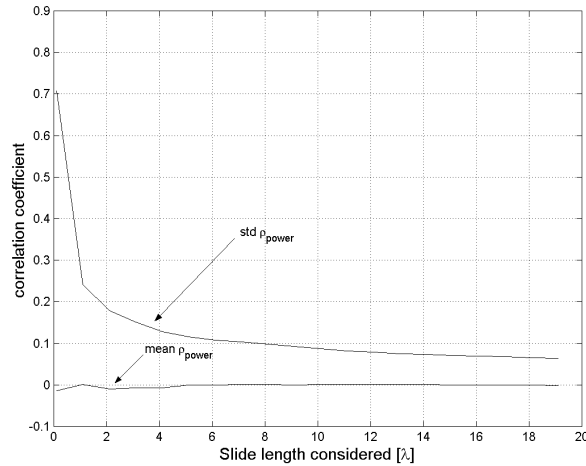

Figure 3.3: Standard deviation of the power correlation coefficient from Monte Carlo simulations over 1,000 realisations of a Rayleigh channel.

3.2.3.2 Power Supply Constraint

The mains power supply was used at the MS since the equipment was always indoors. Nevertheless, when moving from one office to another, the equipment would have to be unplugged and with potential loss of the phase reference. This was unacceptable and consequently, it was decided to use a simple computer 520 W UPS (Un-interruptable Power Supply). This simple trick provided the Tx with 15 minutes of self contained power.

At the Rx, the power supply was either provided from the mains socket in case of picocell measurements, or from the inverter of the Fiat van for the microcell measurements.

3.2.4 Antenna Topologies - METRA Programme

Commercial antennas at the time of the field trial were not available for the UMTS frequency band used in the METRA measurement campaign. The scope of the PhD was to investigate the correlation coefficient which exist between several element of a MEA considering far-field condition, i.e. no near-field terminal effect were consider,

to later validate a MIMO model with respect to its assumptions. Therefore, vertical and horizontal polarized sleeve dipoles, with an average return loss of approximately 14 dB and a XPD (cross-polar discrimination) of 20 dB, were manufactured at the RF laboratory of CPK and used during the measurement campaign. Measurement set-ups including scenarios of typical small terminals [44] were not considered in this study.

The sleeve dipoles, seen in Figure 3.4, has a $1/4\lambda$ bazooka balun to reduce electrical leakage in the coaxial cable [108, p. 480], thereby decreasing the influence of the feed cables on the radiation characteristic of the dipole. A balun was preferred to a ferrite since the operating frequency was higher than 1 GHz [109].
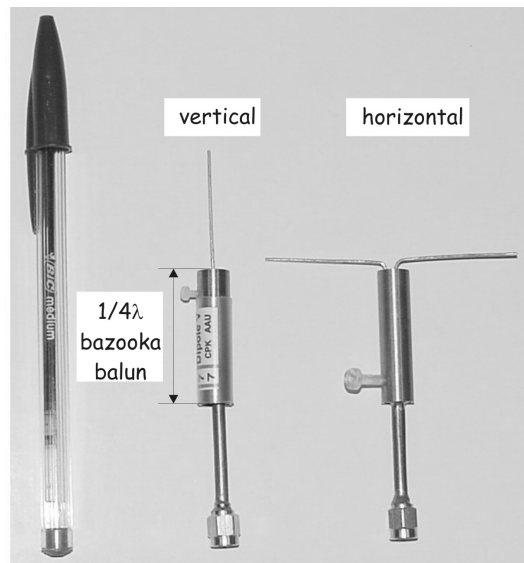
Figure 3.4: Customised sleeve dipoles (vertically polarized to the left and horizontally polarized to the right) using a $1/4\lambda$ bazooka balun.

3.2.4.1   Mutual Coupling in the MEAs at the MS

While the sleeve dipoles provided omnidirectional radiation patterns when used as single elements, the use of these antennas in a MEA raised the issue of a mutual coupling for small element separation as addressed n the following.

Figure 3.5 presents the measured and simulated co-polarized radiation patterns of a sleeve dipole in the azimuth plane for two MEAs configuration: a linear MEA and an interleaved MEA.

Figure 3.5(i-a) illustrates a 4-element linear MEA with 0.5λ separation. The MEA is simulated using AWAS$^{©}$ [110] which is a numerical analysis tool of wire antennas and scatterers. A good match exists between the simulation and the measured radiation

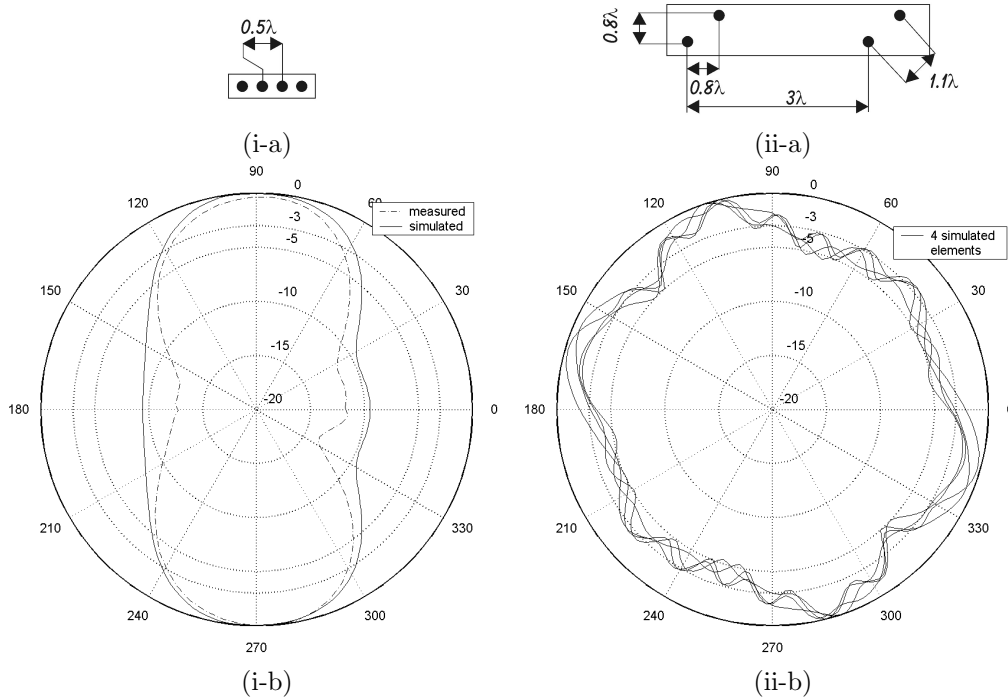pattern as seen in Figure 3.5(i-b).

Figure 3.5: (i-a) Linear MEA set-up. (i-b) Coupling effect on measured and simulated co-polarized radiation patterns in azimuth of one of the four elements of a linear MEA with 0.5λ separation. Notice the squeezing effect on both measured and simulated radiation patterns.(ii-a) Interleave MEA set-up. (ii-b) Simulated co-polarized radiation patterns in azimuth of the four elements of the MEA.

The effect of mutual coupling has a large impact on the shape of the radiation pattern with the measurement showing a reduction in gain of 10 dB for rays coming from either 0° or 180°. Such variations in the radiation pattern would impact the spatial correlation coefficient if no post-processing compensation were made. It was essential to use a MEA topology having elements with an omnidirectional characteristic so that the correlation properties of the MIMO radio channel could be measured directly.

3.2.4.2 Interleaved MEA at the MS

Having identified the mutual coupling issue at the MS, a further constraint which has to be considered is the separation of the elements of the MEA. In order to provide DoA analysis at the MS, it was decided to use a separation of 0.4λ between the elements. This spacing is justified in connection with the DOA analysis presented later in Section 4.3 on page 54. Using AWAS©, different antenna scenarios were investigated to provide a MEA with elements exhibiting omnidirectional radiation patterns. A solution to the two requirements of omnidirectionality and 0.4λ separation, is to use

an interleaved MEA as shown in Figure 3.5(ii-a).

The interest of using an interleaved MEA is that it provides an actual separation of 1.1λ between the elements compared to a traditional linear MEA. Furthermore, the 3λ separation cancels the coupling between the two pairs of elements. Figure 3.5(ii-b) illustrates the simulated co-polarized radiation patterns in the azimuth plane of the four elements of the MEA used during the measurement campaign. The influence of the mutual coupling is significantly reduced due to the interleaved MEA. The influence of the compensated radiation pattern on the correlation coefficient is discussed in Appendix B.

Two linear MEA, with 0.4λ separation, are generated from the interleaved MEA after post-processing as shown in Figure 3.6.
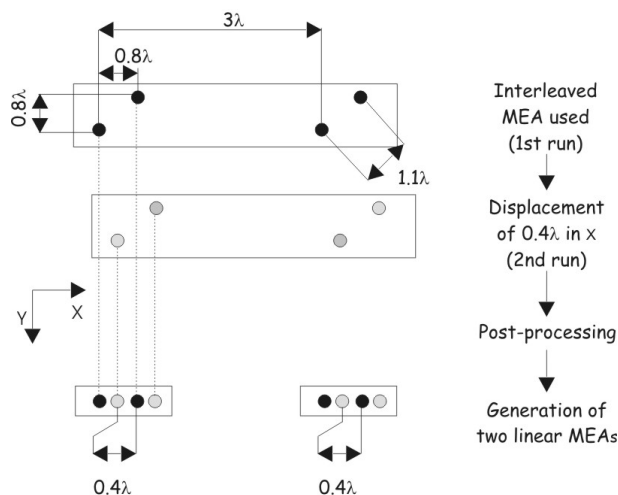
Figure 3.6: Top view drawing of the MEA used during the measurement campaign and the effect of post-processing to generate two linear MEAs at the MS.

3.2.4.3 Linear MEA at the BS

At the other end of the transmission path, the BS consists of two linear separate 4-element MEAs. The first MEA is a uniform, linear MEA with four vertically polarized sleeve dipoles separated by 1.5λ. Contrary to the MS, DoA analyses are not considered at the BS which explains the larger spacing used to avoid mutual coupling.

The second linear MEA consists of two dual polarized $\pm 45°$ patch antennas. Depending on the environment the patches are either at $\pm 45°$ or $90°/0°$ with respect to the vertical as shown in Figure 3.7 and summarized in Figure 3.11 on page 40. The orientation of the patch antenna is very important since the BPR considers simultaneously the XPD of the antenna and the radio channel. As an example, empirical results

showed that the average BPR for patch MEAs varied from 0 dB ($\pm 45°$) down to -8 dB ($90°/0°$). Patch antenna samples were tested and a XPD $\geq$ 15 dB was measured. The radiation patterns of the $+45°$ and $-45°$ branches were measured in the XZ and YZ plane. They exhibit relatively similar radiation patterns which indicates a reasonable rotational symmetric behaviour [111, p.167-168]. However no actual 3-D measurement was performed.
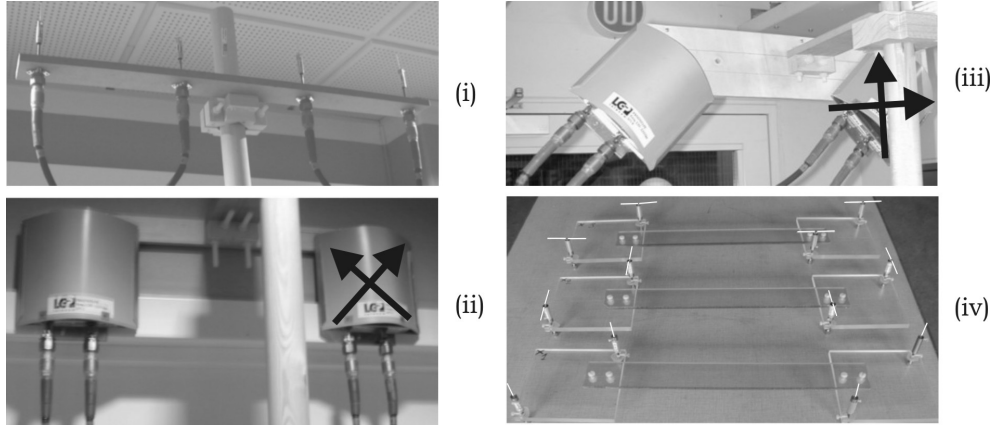

Figure 3.7: Antennas used in the METRA project at the BS (i) vertical dipole (ii) patch antenna ($\pm 45°$) (iii) patch antenna ($90°/0°$), (iv) at the MS.

3.2.4.4 The METRA Experimental Procedure

An explanation is given here, on how two uniform linear MEAs, each having four elements separated by 0.4λ, can be derived from the interleaved MEA. The experimental procedure is described as follows. A 4-element interleaved MEA support, made of a Plexiglas plate, is mounted on the mast of the dragon slide, see Figure 3.8. This support is necessary since it is decided to use three different MEA arrangements during the measurement campaign to investigate polarization diversity at the Tx. These MEAs are referred to as vertical, horizontal1, and horizontal2.

vertical   horizontal 1   horizontal 2
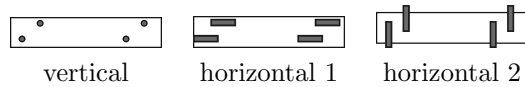
☞ The MEA denoted as vertical consists of four vertical polarized sleeve dipoles.

☞ Horizontal1 and horizontal2 both used four horizontal polarized sleeve dipoles and differ only in the orientation of their elements as shown above and in Figure 3.7(iv).

The measurement procedure in connection with Figure 3.8 is explained below:

① The four elements of each MEA are locked on the Plexiglas support to fix the elements during the measurement campaign and to maintain the same spatial reference between the different MEAs for AoA analysis.

② For a stationary position of the dragon, the MEA moves forward along the Y-axis, during 5 s (i.e. from A to B) while the received signals is being recorded.

③ When the MEA reaches the end of the slide (B), it moves backward while the slide was moved over a distance of 0.4λ perpendicularly to the motion of the MEA. This displacement is feasible since the slide itself is mounted on two rails, see Figure 3.8.

④ Starting from C, a new set of measurements is then collected (C to D).

⑤ The MEA is replaced and a new measurement is taken.
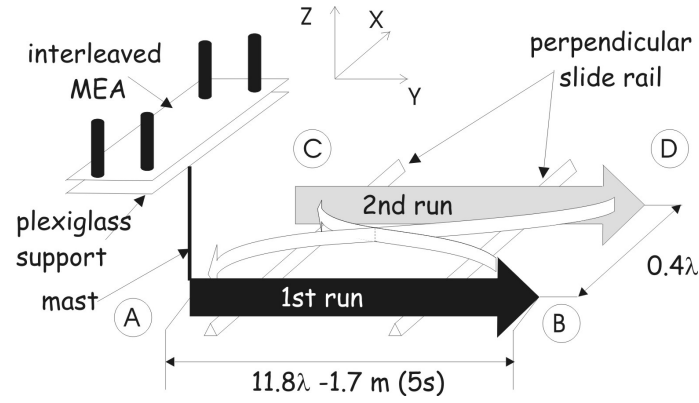
Figure 3.8: 3-D representation of the measurement procedure at the MS.

This procedure is completed within 20 s as an attempt to have a time stationary radio channel. Then the MEA is changed and the procedure repeated twice to have the two polarizations investigated. Therefore, in total three measurements (with three different MEAs at the MS) were made for each path, and for each MEA, two sets of measured data were obtained.

The acceleration and deceleration phases of the MEA moving along the slide were compensated and post-processed in the measurement analysis. Figure 3.9 presents the effective slide length which could be used during the analysis of the measured data due to the synthetical displacement of 0.8 λ in Y, for the post-processing implementation of a linear MEA.

3.2.4.5   The Radiation Pattern Impact

The correlation coefficient results presented in this thesis are based on measured data. Consequently the spatial selectivity introduced by the antenna characteristics is con-
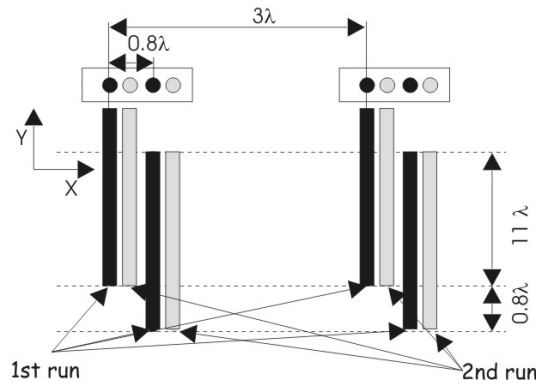
Figure 3.9: *Effective displacement of the linear MEA during the analysis of the measured data.*

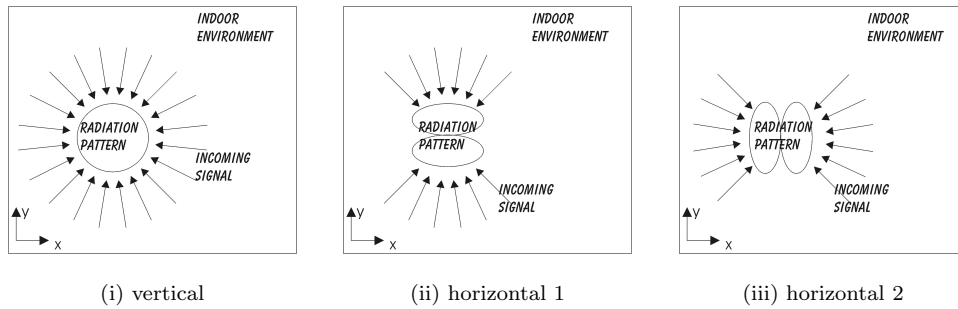sidered in this thesis with respect to the impact of the radiation pattern, introducing the pattern diversity.

| (i) vertical | (ii) horizontal 1 | (iii) horizontal 2 |

Figure 3.10: *Top view of a simplified indoor environment. Illustration of the radiation pattern effect on the ray selection of the radio channel.*

The type of antenna, and therefore the radiation pattern, used to record the data is an important parameter to consider when analysing measured data. When employing the horizontal MEA elements, the correlation coefficient reflects only part of the radio channel since a certain spatial selectivity occurs in the azimuth plane as illustrated by the three sketches of Figure 3.10.

Constraints on the radiation pattern are a practical reality when implementing the MIMO technology. To date, perfect omnidirectional aerials, i.e., most commonly loop antennas, in the horizontal plane are very difficult to apply and are not commercially available. Its use in pattern diversity is introduced later in the thesis.

A summary of the different antenna topologies used in the measurements reported in the thesis is presented in Figure 3.11. Pictures of some of the MEA used during the measurement campaign are illustrated in Figure 3.7.
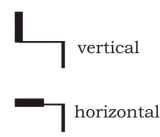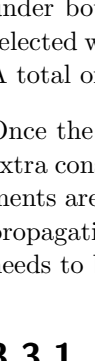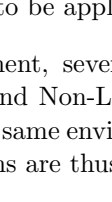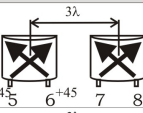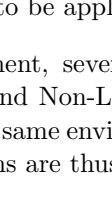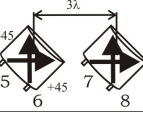
SUNBEAM measurement programme	Environment	MS		BS	
		height (m)	MEA set-up (side view)	height (m)	MEA set-up (side view)
	novi2- microcell	1.69	vertical / horizontal	9.0	1 5 2 6 3 7 4 8

METRA measurement programme	Environment	MS		BS (dipole)		BS (patch)	
		height (m)	antenna set-up (top view)	height (m)	antenna set-up (side view)	height (m)	antenna set-up (side view)
	novi2 - picocell	1.69	vertical	2.34		2.34	
	novi3 - picocell	1.69		2.34		2.34	
	nokia - picocell	1.69	horizontal 1	2.34	3λ	2.34	
	fb7b2 - picocell	1.69		2.04		1.93	
	Airport - picocell	1.69	horizontal 2	2.53	1 2 3 4	2.35	
	frb7-microcell	1.69		5.7		5.7	

Figure 3.11: *Summary of the different antenna topologies used for SUNBEAM and METRA.*

3.3 The Choice of Environments

The selection of the environments to be investigated is based on the ambition to provide general and realistic examples on the MIMO technology performances. Several buildings offered the opportunity to investigate picocell and microcell environments: the University campus due to the proximity and logistical reasons, and the Aalborg International airport, both of which presented realistic environments where MIMO systems are likely to be applied.

For each environment, several MS locations are selected to provide measurements under both LOS and Non-Line-of-Sight (NLOS) scenarios. Several BS locations are selected within the same environment to increase the amount of statistical information. A total of 114 paths are thus investigated within 7 environments.

Once the decision is made with regard to the location of the measured environment, extra constraints are imposed on the experimental programme. For instance, measurements are to be performed during night-time as an attempt to operate in a stationary propagation channel. Therefore, special permission to get access to the different offices needs to be granted.

3.3.1 Picocell

A total of 5 environments were considered suitable for picocell measurements. In this thesis, the term picocell describes an indoor-to-indoor transmission path. They are denoted after the different building names, as novi2, novi3, nokia, fb7b2 and airport.

They all differed in size, internal structure or layout. A description of the different picocell layouts is given below and to visualize the environment, a floor plan of each environment with pictures taken during the measurement campaign is presented in Appendix A.

novi2 offered an example of a building with several small offices on the same floor, as shown on the top view plan of Figure 3.12. The arrows illustrate the direction of displacement of the MS (1 to 7). The layout and size of novi2 are suitable to identify three locations for the BS. In total 21 measured paths were investigated in this environment.
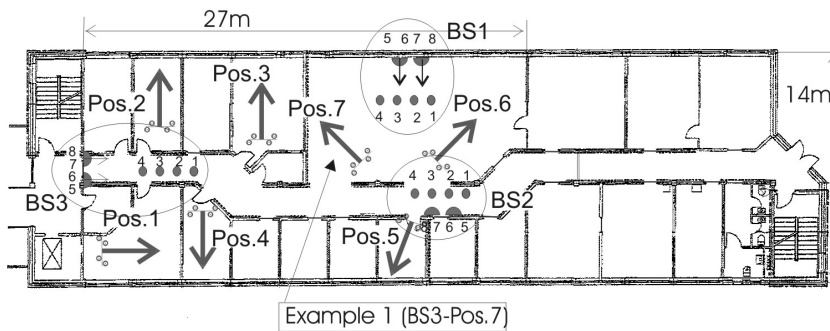

Figure 3.12: novi2. The arrows represent the direction of the displacement of the MS (1 to 7). The 3 encircled areas represent the different positions of the BS. In total 21 measurement paths were investigated in this environment.

The outside windows are so-called energy windows, meaning that they are metallically shielded reflecting electromagnetic waves. The building structure of the indoor environment is presented in Figure 3.13. The walls are made of plaster board on metallic studs. Also, between the ceiling tiles, made of fiberboard, and the concrete ceiling lies a complex air-conditioning pipe system made of metal. This environment is also used for the microcell measurements which are discussed later in Section 3.3.2.

nokia (illustration on page 125) is of the same size as novi2 but contrary to novi2, as shown in Figure A.1, it provides a typical, modern open office environment. The outside windows of the building are also metallically shielded.

novi3 (illustration on page 126) is a large foyer as shown in Figure A.2 and Figure A.3. It provides a large open indoor environment with two floors, which could also represent a conference hall or a shopping center scenario. Again, the outside windows of the building are metallically shielded.

fb7b2 (illustration on page 128) also provides an example of a building with several small offices on the same floor, but its outside windows are not metallically shielded. This environment is illustrated in Figure A.4. It is also used for the microcell measurements, see Section 3.3.2 below.
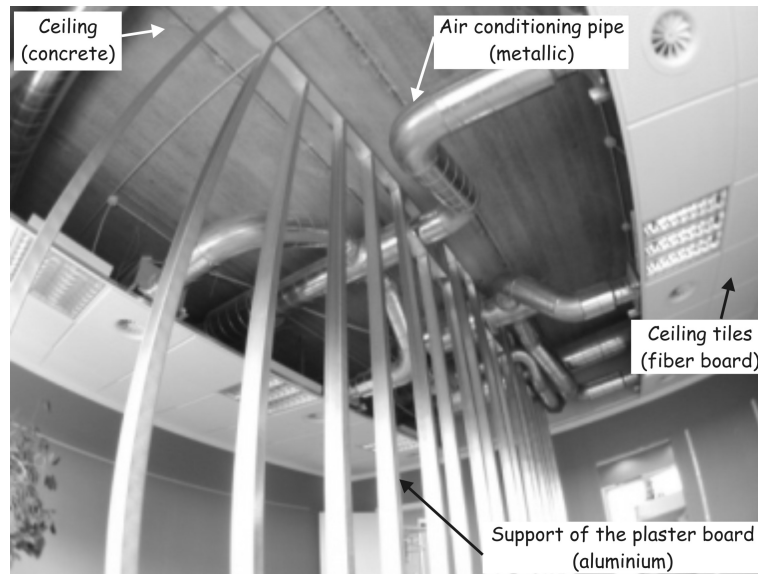
Figure 3.13: Indoor structure of the building. The picture indicates that the metallic studs are hidden behind the plaster wall.

airport (illustration on page 130) is a middle size international airport situated in Aalborg. It provides relatively large open areas for an indoor environment, see Figure A.5 and Figure A.6. This is an interesting environment due to its size and is likely to host business users with applications suitable for the capacity enhancement of MIMO based services. One side of the building is mainly composed of energy windows as shown in Figure A.6 (i).

3.3.2   Microcell

The microcell investigation considered 2 environments. In this thesis, the term microcell describes an indoor-to-outdoor path. Reasonable path loss consideration motivated the selection of these two sites. Figure 3.14 provides an overview of the microcell field trial. The MS was inside the building while the BS was located outside. The two buildings investigated are denoted novi2 and fb7b2. During the microcell measurement campaign, a laboratory van was equipped with the BS equipment.

novi2 (illustration on page 132) The first microcell measurement campaign is undertaken during the SUNBEAM project in novi2. The indoor environment has been presented in the previous section on page 40. It was decided to select 15 different locations of the MS in the building.

At the other end of the transmission path, a parking, 300 m away from the building, is used to positioned the van with its the BS. The MEA is mounted on
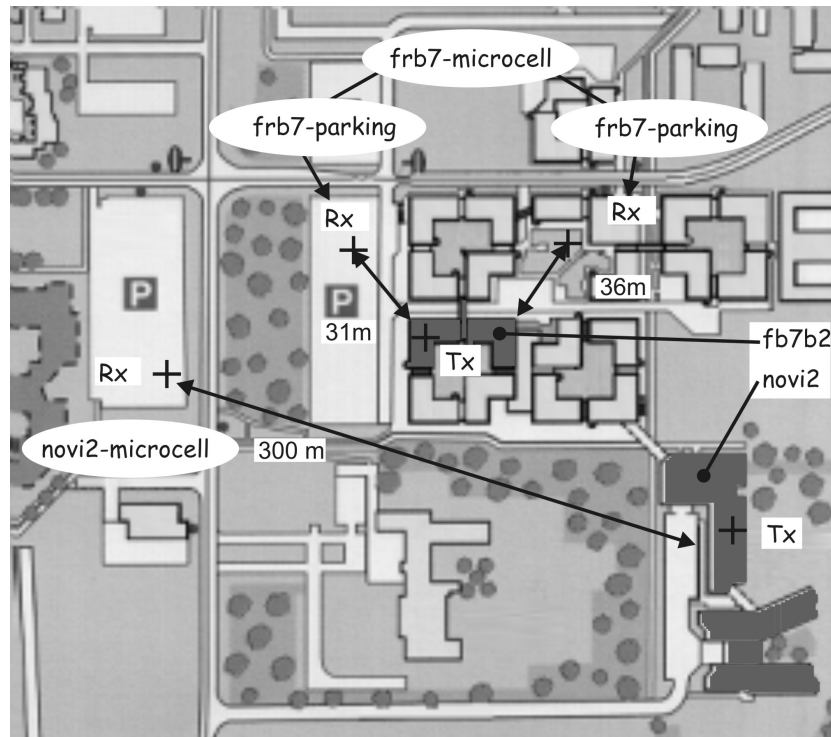
Figure 3.14: Illustration of the two microcell environment setups.

a crane and elevated above roof top level, i.e., 9 m, to provide direct LOS to the building while the RF equipment is secured in the van.

frb7 (illustration on page 131) The interest in a microcell measurement campaign is not only the cell size, but also the density of the scattering environment surrounding the BS. After a survey of the university campus, the building fb7b2 is selected to host the MS. The BS is positioned on two separate locations as shown in Figure 3.14: The first case is a courtyard providing an example of a closed environment (high density of local scattering). The second case is a parking area with an open environment (moderate scattering). The MEAs are placed on a mast below roof top level at a height of 5.7 m (see the mast in Figure 3.18 on page 46). The distance between the BS and the MS is 36 m and 31 m for the first and second case, respectively. A picture of the environment is given in Figure A.7.

Table 3.2 presents the environments investigated, the number of measured paths and the measured mean SNR per path for the two projects. It indicates that the link budget was very good since the mean SNR is limited by the correlation noise of the PN sequences of the system. Only in a minority of the paths, the mean SNR was as

low as 10 dB.

Environ-ment	Building identi-fication	Number of BS locations	Number of MS locations	Number of paths	Mean SNR per path in dB	Project
Picocell	Novi2	3	7	21	31	METRA
	novi3	1 1	9 3	12	31	METRA
	Nokia	3	5	18	31	METRA
	fb7b2	2	8	16	best-31 /worst-10	METRA
	airport	2	6	12	30	METRA
Microcell	Novi2	1	15	15	31	SUNBEAM
	frb7	1 1	8 5	13	best-31 /worst-15	METRA
Total number of investigated paths				107		

Table 3.2: Number of paths with their respective mean SNR.

3.4   Summary and Interim Conclusion

This chapter presented a description of the experimental work which paved the way for the beginning of the PhD programme. Two main parts were identified: a description of the RF equipment and the environment investigated.

Two measurement set-ups namely SUNBEAM and METRA have been developed for the MIMO investigation of the radio channel. Suitable measured environments were identified to provide realistic propagation environments for picocellular and microcellular wireless system where the MIMO technology is likely to be implemented. The measurement set-up only considered MEA wich were not under near-field's influences. Measurement set-up including scenarios of typical small terminals were not considered in this study.

WB MIMO measurement campaign have been performed during the PhD programme using the UMTS bandwidth of 5 MHz. Microcell and picocell environments have been investigated using different type of MEA configurations. Spatial, polarization and hybrid spatial-polarization diversity set-up can be extracted from the MIMO measurement data.

The MIMO measurement campaigns presented in this chapter are among the first MIMO radio propagation channel results reported in the MIMO community.

Figures 3.18 to 3.20 show pictures taken during the measurement campaign, of the experimental equipment and environment, to illustrate the level of detail in terms of design, planning, environment considerations and hardware logistics.

Figure 3.15: BS stand alone testbed. All the equipment is mounted on wheels to provide high mobility during the set-up. The duplicated Rx branches can be seen on the left hand side of the picture.

Computer to operate the BS and store the measured data set
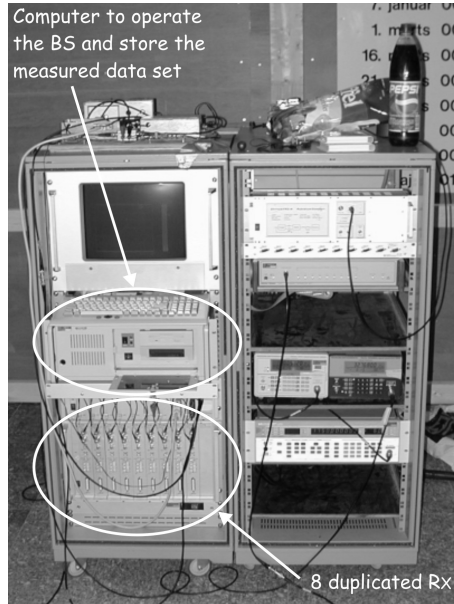
8 duplicated Rx

Figure 3.16: At the other end of the transmission path: the 1st trolley of the MS with the voluminous RF equipment placed on large wheels to ease transportation. The connecting cable to 2nd trolley (the dragon) can be seen lying on the floor.

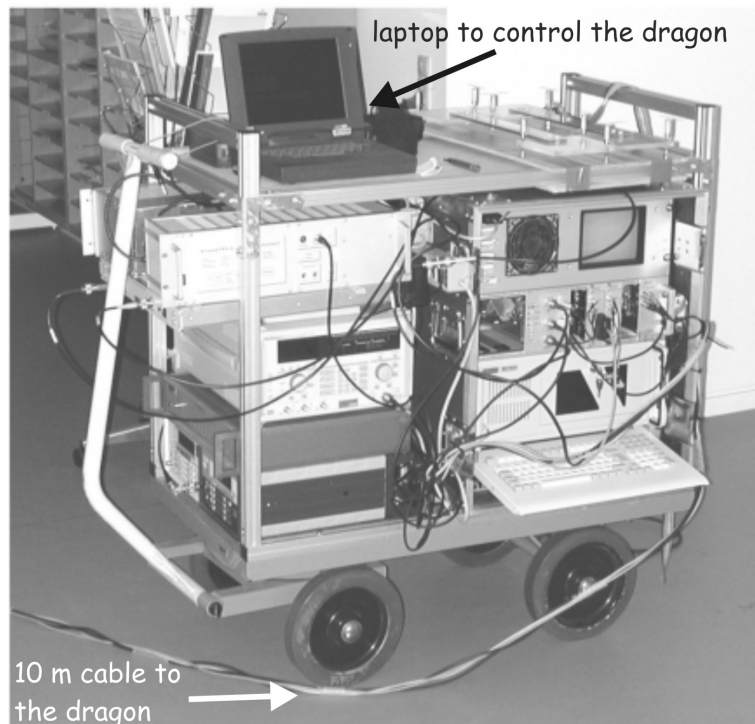laptop to control the dragon

10 m cable to the dragon

Figure 3.17: METRA project. The MS appears in the foreground with the dragon and its absorbers while the BS stands in the background.
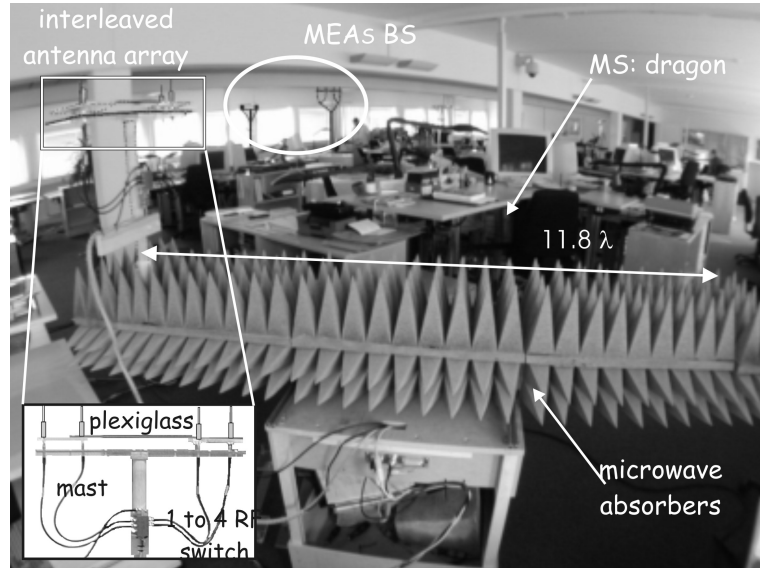

Figure 3.18: Illustration of the measurement equipment at the BS in the courtyard of the frb7 microcell environment (picture taken by night).
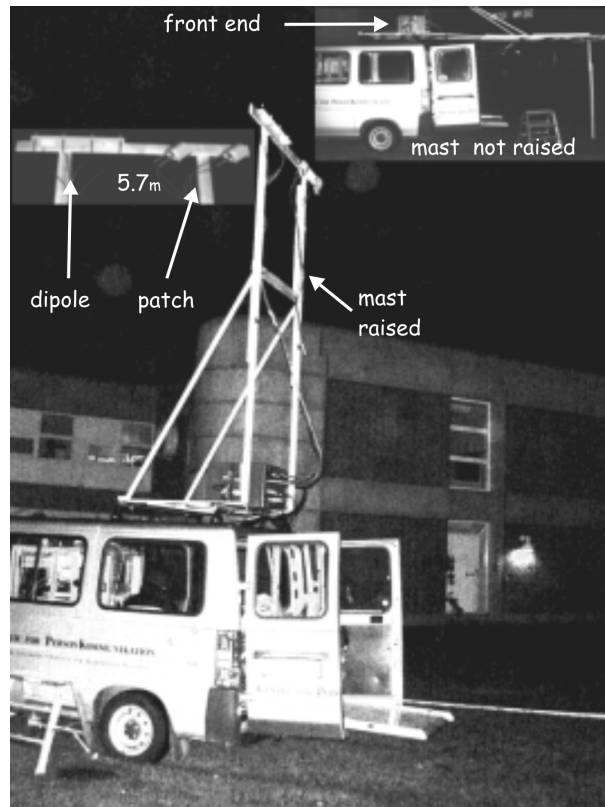
Figure 3.19: First example of a MIMO radio channel measurements, novi3. As described in Section 3.3.1 on page 40, this environment can also represent a conference hall or shopping center. The BS MEAs (dipole and patch) are located on the first floor. Notice the two trolley of the MS; the RF trolley is next to the stairs and the dragon is in the bottom right corner of the picture.

Figure 3.20: Second example of a MIMO radio channel measurements, fb7b2. The dragon is positioned in the middle of the room. Notice the space limitations to fit the dragon inside the office. The other trolley with all the RF equipment was in the corridor as illustrated in Figure 3.1.

Chapter 4

Characterisation of the Radio Channel

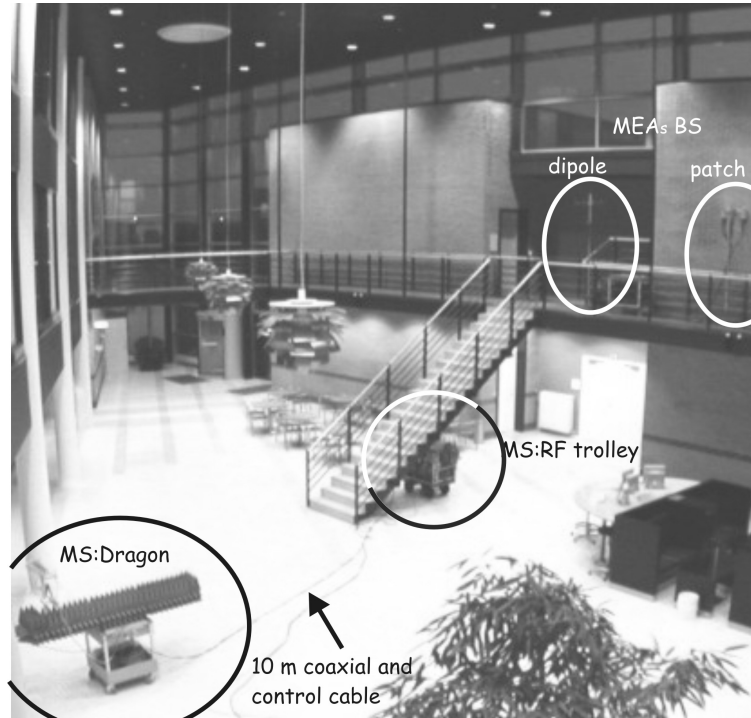The analysis of the measured data has been divided into two parts. The first part is presented in this chapter and deals with the propagation characteristics of the measured environment with respect to SISO and SIMO antenna topologies. The second part of the analysis is presented in Chapter 6, where MIMO system performance in terms of theoretical Shannon capacity is addressed.

This chapter is dedicated to the extraction of channel parameters from the measured data. The channel parameters are obtained from the NB information of the WB measured data. It includes the study of the statistical distribution in terms of the Ricean *K-factor* and a characterisation of the direction of arrival DoA. The two informations are used together to categorise the environment investigated in terms of their LOS/NLOS and low/high AS characteristics. Conclusions on the angular distribution of the wave in indoor are drawn based on the DoA analysis applied to the measured data. A cluster type of distribution rather than a uniform one is shown. Furthermore, the DoA analysis allows to draw conclusions on whether the WSS requirement holds for the measured data. It is shown that some measurement paths do not hold such a requirement.

Study of the power correlation coefficient is addressed based on measured data for different cell environments, i.e., picocell and microcell, and different antenna configurations. The analysis considers the spatial correlation coefficient, the polarization correlation coefficient, the joint spatial-polarization correlation coefficient, and the joint pattern-spatial-polarization correlation coefficient.

Finally, a summary of some measurement paths is proposed at the end of this chapter. They are selected for their propagation characteristics, and are specifically used in the

rest of this thesis as examples of the performance of the MIMO technology.

4.1   From Wideband to Narrowband

The measurement campaign provided MIMO sounding radio channel data. A simple
algorithm called CLEAN, originally developed for processing astronomical images [112]
and recently used to estimate the dispersion of the radio channel [113][114] was selected
to extract the high resolution complex information from the WB measured data [1]. This
algorithm, presented in Appendix D, performs fairly well when the temporal dispersion
is sufficiently large compared to the resolution of the measurement system. In large
microcells, i.e., the microcell investigated during the SUNBEAM project, the CLEAN
algorithm would be efficient. However, for picocells or microcells of smaller size, like
the one investigated as part of the METRA project, the resolution of the measurement
signal was too low to identify any time dispersion in the radio communication channel
without error from the CLEAN algorithm. Due to this reason, the CLEAN algorithm
was not used in the analysis presented in the thesis.

The RMS (Root Mean Square) delay spread, σ, is used in this section to quantify the
low time dispersion of the indoor channel. The extraction procedure of σ from a WB
received signal is presented in Appendix E. The RMS delay spread of the channel
$\sigma_{channel}$, can be extracted from the relationship which links the RMS delay spread of
the measurement system $\sigma_{system} = 0.0946 \mu s$ derived from the *back-to-back* measured
IR, and the recorded $\sigma_{measured}$. This relation is based on the variance subtraction
operation, i.e.,

$$\sigma^2_{channel} = \sigma^2_{measured} - \sigma^2_{system} \, , \tag{4.1}$$

and is applicable when assuming decorrelated scatterers [117], [94] or non coherent
voltage addition [118].

The cdf of $\sigma_{channel}$ was computed for all the measured paths and is presented in Fig-
ure 4.1. The sampling resolution of the measurement system was $0.122 \mu s$, whereas
the excess delay resolution was 1.5 chip $= 0.366 \mu s$ so no significance can be attributed
to details between 0 and $0.366 \mu s$. However, it illustrates that for 98% of the paths
in the picocell environments, $\sigma_{channel}$ is less than $0.366 \mu s$. This is in good agreement
with [117][119] among others for indoor scenarios. For the investigated microcell envi-
ronments, it is observed that only 25% of the paths provide a larger time dispersion.
Based on these results, it was decided to use the NB information in the subsequent
analysis since the limited excess delay resolution did not make it possible to resolve
the multipath components in typical indoor environment.

The complex NB information $\alpha_{mn}(t)$, defined in Section 2.2 on page 12 is computed
from the measured WB signal $\alpha^{wb}_{mn}(t, \tau_l)$ where t and τ are time and delay respec-
tively. This operation is equivalent to selecting one specific frequency component in

---

[1]Note that this method is very similar to the "direct convolution" method as reported in [115]
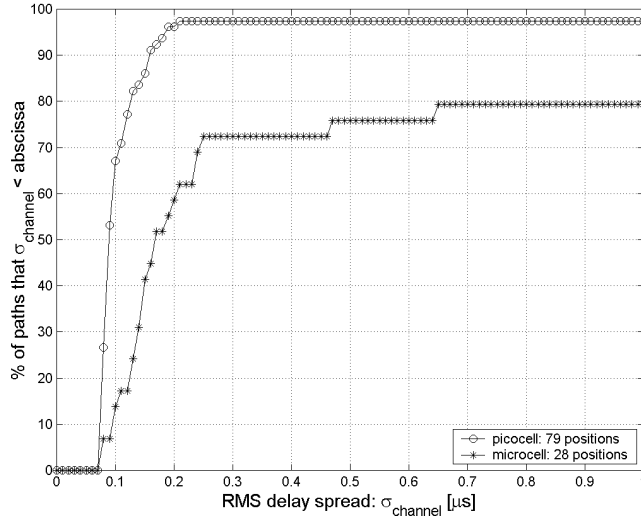[116].

Figure 4.1: *cdf of* $\sigma_{channel}$ *for picocell and microcell environments.*

the frequency domain, i.e., $f = 0$ at baseband, of the WB measured signals [94] and so that

$$\alpha_{mn}(t) = \frac{1}{L} \sum_{l=1}^{L} \alpha_{mn}^{wb}(t, \tau_l) \tag{4.2}$$

where $1/L$ is used as a scaling factor. For the computation of $\alpha_{mn}(t)$, a square window is applied on the $\alpha_{mn}^{wb}(t, \tau_l)$, meaning that only a part of the WB measured data is used in the average process, hence filtering out part of the noise.

4.2 Statistical Distribution of the NB Signal

For a more comprehensive characterization of the radio channel based on the measured data, it is necessary to know the statistical nature, i.e., the Ricean *K-factor*, of the postprocessed measured NB signal; the result of this analysis is useful for the categorization of the paths when the correlation coefficient is investigated.

Often radio paths are categorized as LOS or NLOS. In this thesis LOS is defined as a path where there is no obstruction between the two ends of the radio path. LOS scenario are often associated with the Rice distribution, since a strong signal component (the actual LOS) and smaller components (the reflected waves) compose such a distribution, while in a Rayleigh distribution, the LOS component disappears and only the reflected waves are existent.

For the microcell environments, the concept of LOS is inadequate since the outdoor

wall of a building lies between the two ends of the radio path. However the existence of a strong direct path in such a scenario would still results in a Rice distribution too. This strong direct path would be the result of the energy being narrowbeamed due to a low AS at one or both end of the paths. Subsequently, the value of the *K-factor* should rather be attributed to the spatial dispersion of the waves; the AS was used as a reference to interpret the behavior of the *K-factor*.

A classification of the interpretation of the estimated *K-factor* is shown in Table 4.2 where environment, size, structure and cell type are dependent parameters.

Cell	*K-factor*	
type	$\in [0, 2[$ (Rayleigh-like)	$\in [2, \infty]$ (Rice-like)
Picocell	NLOS	LOS
Microcell	high AS	low AS (at BS)

Table 4.1: Classification of the K-factor.

The method used to estimate the *K-factor* is based on the work reported in [120] and is presented in Appendix F. The analysis considers a 4×4 antenna setup so that the SISO amount of statistics on the received signal is increased by a factor of 16. Equivalently, the *K-factor* is estimated over a distance of about $188\lambda = 16 \times 11.8\lambda$.

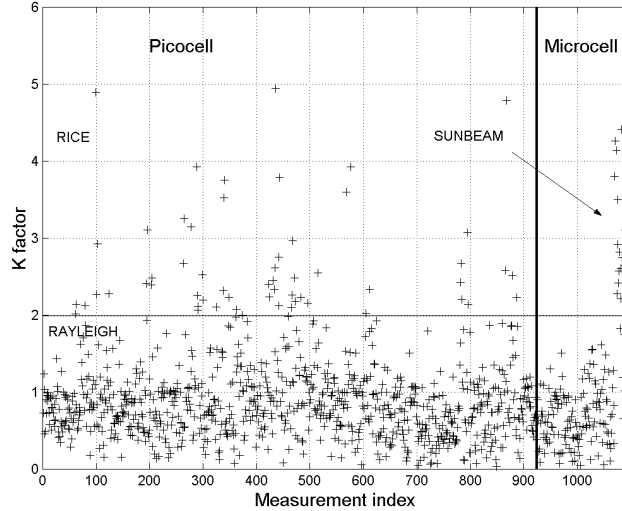

Figure 4.2: K-factor *value for all the picocell and microcell environments for all the transmit and receive antenna configurations.*

Figure 4.2 presents the estimated *K-factor* including all the picocell and microcell environments and all the transmit and receive antenna configurations. The graph has been divided into two zones: the picocell and the microcell and the estimated *K-factor*

indicates a fluctuation from 0 to 6. It is difficult to set a strict boundary between Rice and Rayleigh distributed signals. The value of 2 is believed to be reasonable considering the uncertainty of the measured data and the inherent errors in the estimation process. Therefore, a low value of the *K-factor*, i.e., $K < 2$, is regarded equivalent to a Rayleigh-like distributed radio channel while for larger value of *K-factor*, i.e., $K \geq 2$, the radio channel is said to be Ricean distributed.

For the picocell environments, the majority of the *K-factor* values are lower than 2, indicating that the signals are Rayleigh-like distributed for LOS and NLOS scenarios. For the microcell environments, two measurement set-ups with two different element spacings have been used at the BS; therefore, it is preferred to investigate the microcell per measurement set-up. The SUNBEAM project indicates a majority of the scenario being Ricean distributed (Only 2 paths are identified with Rayleigh distributed signals), while for the METRA project, the microcell environment exhibits Rayleigh distributed signals.
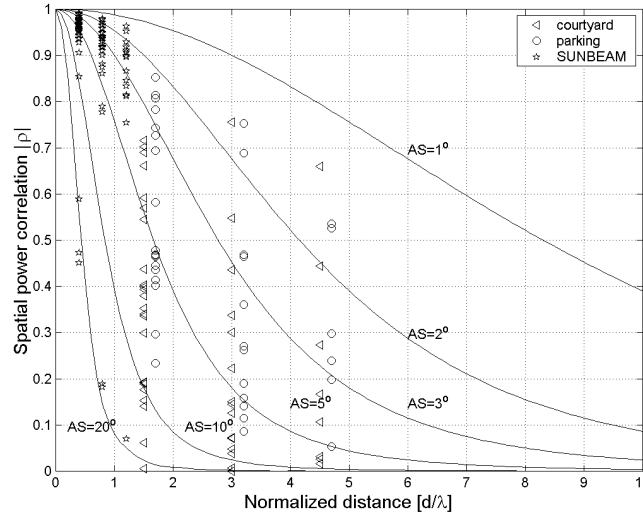

Figure 4.3: Spatial correlation function assuming Laplacean distribution. Measured spatial correlation coefficients for all the microcells plotted per antenna separation.

Figure 4.3 presents the spatial power correlation versus the element separation at the MEA for both the SUNBEAM and the METRA measurements. On the same graph, the spatial correlation function assuming a Laplacean PAS function [84] is plotted. The AS is derived by matching the spatial correlation value to the PAS function.

The measurements performed as part of the SUNBEAM project exhibit 14 paths out of 15 with a low AS in the range of 1° to 5°, and one path having a higher AS equal to 20°. Large values of the *K-factor*, i.e.,*K-factor*$\geq$ 2, were observed for this measurement

campaign when comparing with Figure 4.2.

The two METRA microcell environments indicate higher AS values in Figure 4.3, with some cases where the spatial power correlation is about 0.8 (for the parking measurement, this is due to the lower density of scattering), which is in agreement with the fluctuation of the range of the *K-factor* from 0 to 2.

4.3   Analysis of the Direction of Arrival

In addition to the knowledge of the statistical distribution of the radio channel, DoA analyses are performed at the MS. For the specific application of this thesis, the meaning of arrival in DoA is understood in a large sense and the term departure as direction of departure (DoD) could have also been used since the DoA analysis could be performed at only one end of the path. Recall that DoA could not be performed at the BS since the spacing between the MEA elements was too large. There are several motivations for performing the DoA analysis at the MS:

① The possibility of verifying whether the radio channel satisfies the WSS condition in the investigated indoor environments. The DOA analysis can provide an illustration of the PAS at the MEA in order to test the implicit WSS assumption of the model.

② The nature of the incoming rays when *indoor-to-indoor* and *outdoor-to-indoor* communication links are considered. Indeed, the results of the DoA analysis would confirm, or not, the usual assumption that for a picocell environment the rays are uniformly distributed in an angle around the MS. It was found in [121] that in an outdoor-to-indoor scenario the main contribution to the signal energy is in the direction of the windows.

| ! | DoA analysis has not been performed on any of the measured data collected during the SUNBEAM project due to the measurement set-up employed. Only the vertically transmitted scenarios of the METRA measurement campaigns are considered in the DoA analysis. However the DoA analysis result is constrained to the limitation of the measurement equipment and a 3-D spherical MEA would be usefull to investigate the influence of the ground and ceiling on the total DoA results when indoor-to-indoor propagation scenario are considered.

4.3.1   Geometrical Constraint

There is a large variety of MEA structures used for the DoA estimation. The most common structures are the linear MEA, the square MEA [122],[108], and the circular MEA [123]. A recently proposed antenna structure using a spherical MEA [124][31] was used to perform 3-D radio channel characterisation at the MS.

4.3.1.1   Far-Field and Spatial Nyquist Criteria

When performing practical measurements, two important constraints have to be considered in DoA analysis: the far-field and the spatial Nyquist criteria.

① The **far-field** [125, p. 396] distance is to be respected if the received signal has to be assumed as composed of plane waves. This is particularly an issue when considering the measurements made in the small offices since the nearest scatterer is relatively close to the MEA. This constraint limits the size of the effective aperture and consequently the number of effective elements when equidistant separation is implemented.

As a rule of thumb [108, p. 480] the far-field distance is equivalent to $2D^2/\lambda$ where λ is the wavelength and D is the largest linear dimension of the MEA, i.e., the effective aperture, as shown in Figure 4.4 for both linear and square MEAs.

② The **spatial Nyquist criteria** is to be considered when sampling the signal in the spatial domain. This is very similar to the sampling process in the time or frequency domain. As shown in [126] among others, the spatial Nyquist criteria is necessary to avoid aliasing and grating lobe effects. The duality, when the MEA elements are isotropic, can be presented as

$$f_o = 2f_{max} \longleftrightarrow d_o = \frac{\lambda}{2} \ , \tag{4.3}$$

where f_o is the Nyquist criteria with f_{max} as the highest frequency component in the signal, and d_o the spatial Nyquist criteria among the MEA elements. This means that the spacing d between the elements of the MEA should be **less or equal** than half a wavelength ($d \leq d_o$).

4.3.1.2   Square over Linear MEA

In DoA estimation, the scanning range of a linear MEA, see Figure 4.4, is limited since any *end-fire*[2] signal cannot be seen by the MEA with the same pattern as it would be if the signal were *broadside*; the radiation pattern gets worse when it is steered from broadside to end-fire therefore a linear MEA can not provide a full 360° scan. To overcome this problem, a synthetic planar square MEA was used. The term planar indicates that the MEA elements are all lying on the same horizontal plane. In the rest of the thesis, it is simply referred to as the square MEA.

The square MEA configuration allows a full 360° scan in the azimuth plane. Furthermore, equi-distant spacing between the antenna elements, i.e., 0.4λ, is selected so that signals coming from the *back* can be distinguished from the *front* when they are either broadside or end-fire which is not the case when the spacing is equal to $\frac{\lambda}{2}$.

---

[2]The term *end-fire* refers to the side of the MEA where the signal is impinging parallel to the MEA while *broadside* refers to the side where the signal is coming perpendicularly to the MEA [127][108]
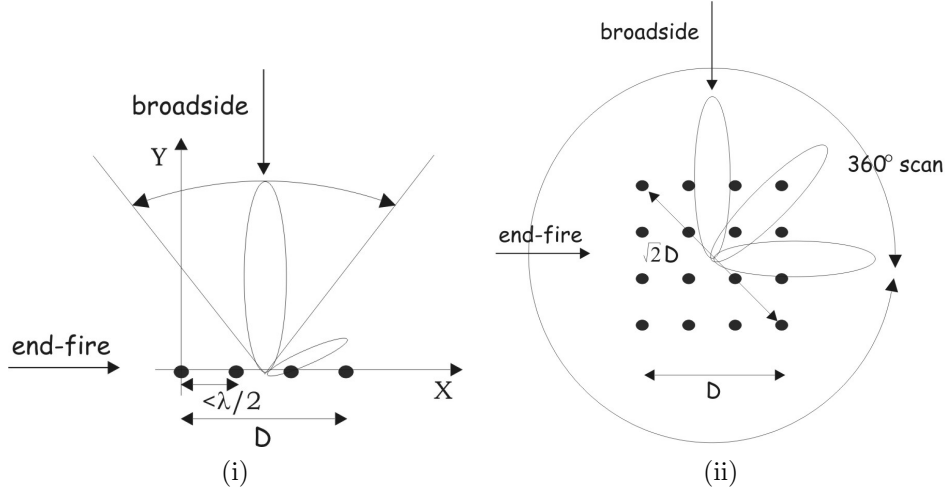
Figure 4.4: Illustration of the scanning possibilities of the (i) linear MEA and (ii) the square MEA.

4.3.1.3   Spatial Filtering Artifacts

The complete 360° scan is not as trivial as it may appear. The beamwidth of an MEA depends on the effective aperture of the MEA. The beamwidth at half power, i.e., at 3dB, $BW_{[3dB]}$, is generally defined as [128]

$$BW_{[3dB]} = arcsin\left(\frac{0.886\lambda}{\Omega d}\right) \ , \tag{4.4}$$

where Ω is the number of linear elements in the MEA along broadside and $d \leq d_o$ is the spacing between the elements in wavelengths. The effective aperture D is defined as

$$D = \Omega d \ , \tag{4.5}$$

meaning that the larger D, the narrower the beamwidth and vice versa.

Figure 4.5, illustrates that when the signal reaches the square MEA at broadside, or similarly end-side, the effective aperture of the antenna is D but at an incident angle of 45° the effective aperture becomes $\sqrt{2}D$. Consequently, the beamwidth at 45° of the MEA is supposedly narrower than the beamwidth at broadside; this is, however, not the case as explained below.

The windowing effect is a well known phenomena in the frequency-time domain analysis [129, p. 450][130, p. 294]. In the spatial domain, this effect occurs when using a square MEA as illustrated in Figure 4.5. At broadside, the measured complex signal is subject to a square window while when arriving at 45° incident angle, it is subject to a Bartlett–or triangular–window.

The windowing effect is illustrated quantitatively in Figure 4.6 where the beamwidth
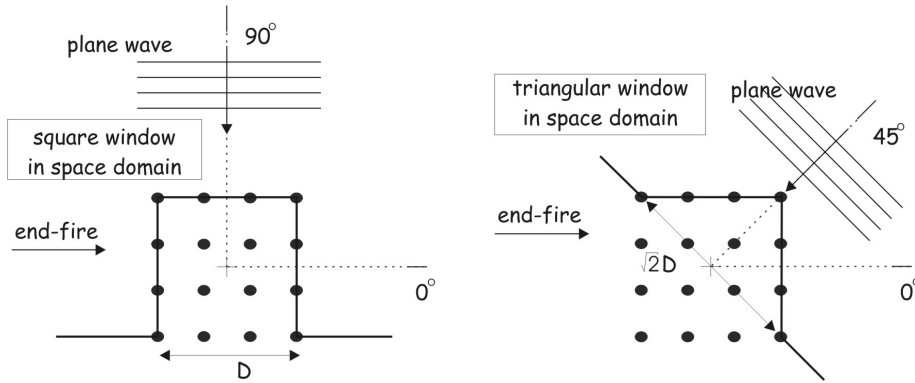
Figure 4.5: Illustration of the windowing effect of the square MEA in the DoA process.

of the square window for $\sqrt{2}D$ is narrower than the square window with D, but as soon as the Bartlett window is applied with $\sqrt{2}D$, the beamwidth is similar (within a 1° accuracy) to the beamwidth computed from a square window with D as an effective aperture. So despite a larger effective aperture at 45° incident angle, it is possible to keep the scanning beamwidth constant at about 33° in the whole azimuth plane.
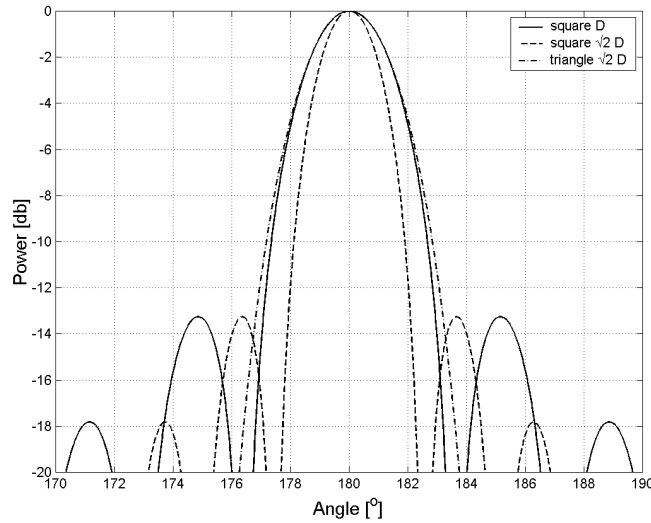

Figure 4.6: Quantitative illustration of the windowing effect of the square MEA in the DoA process.

The differences between the simulated radiation patterns of a linear MEA and square MEAs are illustrated in Figure 4.7 for the cases when an incoming wave is incident at 0° (*end-fire*), 35°, 90° (*broadside*) and 240°.
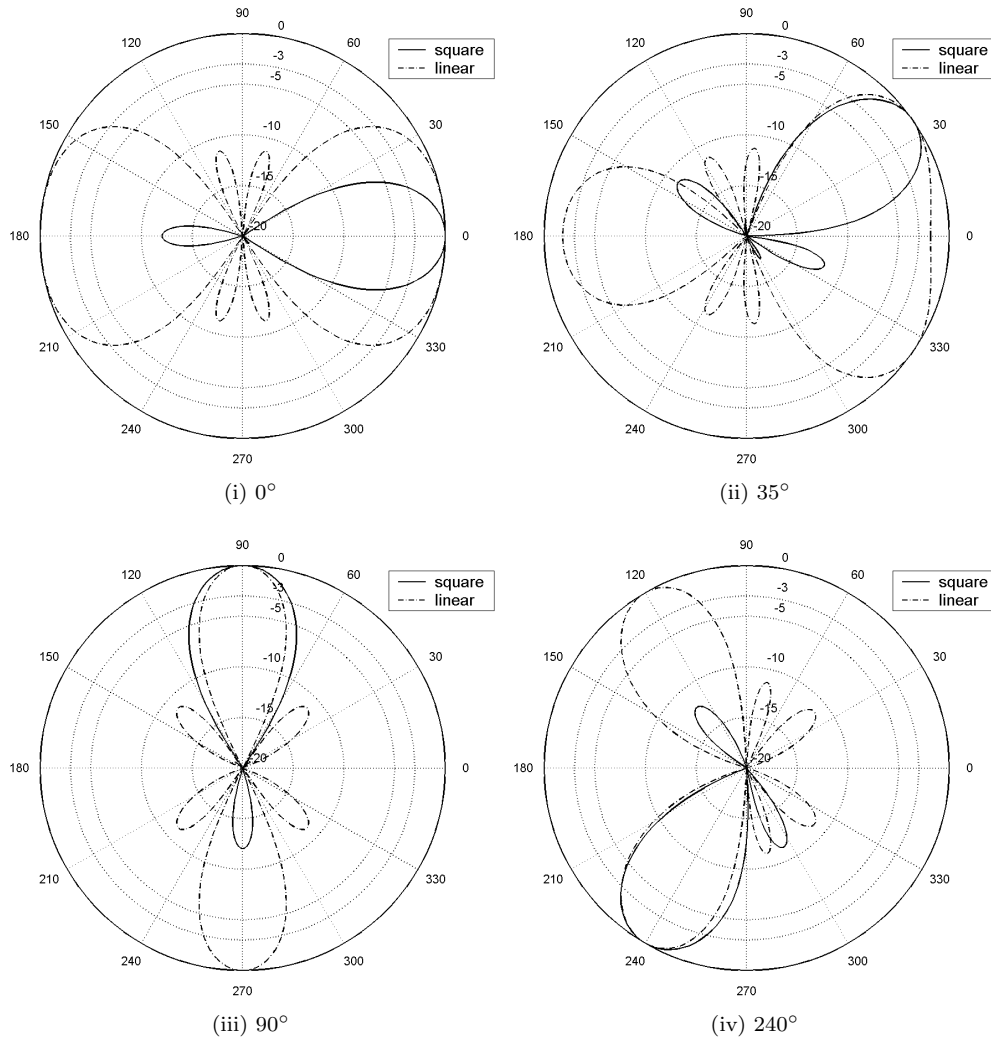
Figure 4.7: Four examples of simulated scanning possibilities when a ray is incident at 0°, 35°, 90° and 240°.

Figure 4.7 (i) presents the DoA results from the linear and square MEAs when the wave are impinging with an incident angle of 0° which is equivalent to an end-fire situation. This figure indicates that the beam of the square MEA points to the desired direction with a half power beamwidth of 33° whereas the linear MEA does not distinguish whether the wave is coming from 0° or 180°, furthermore the beamwidth is much greater than the square MEA beamwidth.

In the case when the incident wave impinges at 35°, Figure 4.7 (ii) indicates that the square MEA points to the desired direction with the same beamwidth as before whereas the beam of the linear is totally distorted.

For the 90° situation, i.e., a broadside, the beamwidth of the linear MEA is optimal but it can not distinguish a wave coming from the front (90°) to a wave impinging from the back (270°). The square MEA however still points to the desired direction with the same beamwidth as before.

And finally, for the 240° situation the square MEA still points to the desired direction with a constant beamwidth.

The characteristics of the linear and square MEAs are summarized in Table 4.2.

Geometrical configuration	Linear MEA	Square MEA	Square MEA
d in X	0.5λ	0.5λ	0.4λ
d in Y	-	0.5λ	0.4λ
Number of elements	4	16	16
Element radiation pattern	omni-directional	omni-directional	omni-directional
Beamwidth[3dB]	26°	26°	33°
Back-to-front determination	no	no	yes
Beam as a function of θ	change	no change	no change
Far-field	4.5λ	9λ	5.8λ
360° scan	no	no	yes

*Table 4.2: Summary of the pros and cons of using linear and square MEAs.*

4.3.2   A Conventional Beamforming DoA Algorithm

There is a large volume of literature devoted to the different types of DoA estimation algorithms, [131][127] among others. The selection of the DoA algorithm is based on [128, p. 61] where different methods like Fourier method, Capon Estimator, MUSIC algorithm, and Widrow algorithm are compared for the estimation of the angular power spectrum. It was found that the Fourier method (also known as the classical or conventional beamformer) was considered as the best trade-off between resolution, accuracy, and complexity.

Therefore, the Fourier method is selected in this work as a simple tool for the DoA study keeping in mind that the resolution of this technique is limited. The mathematical description of the algorithm applied to the specific square MEA is presented in Appendix H.

At the MS, the DoA was estimated from the processed NB signal for each measurement path. In Section 3.2.4.4 on page 37, the procedure to obtain two linear MEA from

the interleaved MEA was presented. From these linear MEAs, two square MEAs (separated by 3λ) were created synthetically from the snapshot along the displacement of the slide. For each of the two square MEAs, 8 DoA estimation analyses were produced for each of the 8 elements of the 2 linear MEAS at the BS.
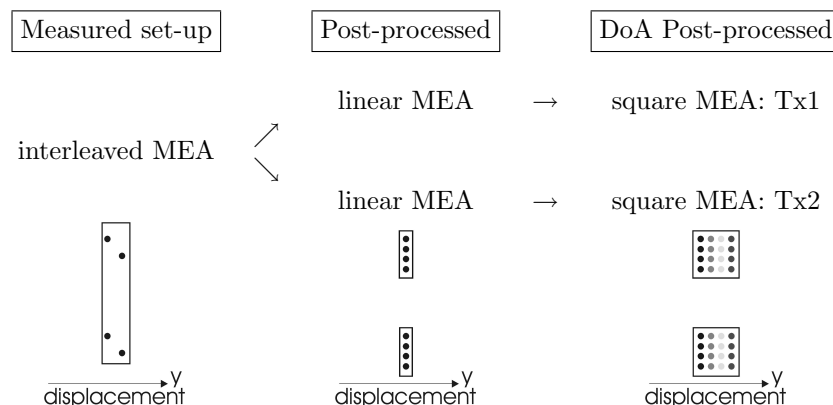
4.3.3 DoA Results Characterisation

This section presents three important results of the DoA analysis. The first results present an example of the characterisation of the spatial nature of the radio channel for a measured environment with respect to the *K-factor* results presented earlier. The two last results give examples of the spatial nature of the radio channel during the measurement with respect to the WSS requirement.

4.3.3.1 Spatial Nature of the Radio Channel

An example of the spatial nature of the radio channel is given in Figure 4.8, i.e., the small office scenario of novi2 presented in Figure 3.12 on page 40. The DoA analysis results are plotted on polar grids for each measurement path. The results are normalized to their maximum for each path and down limited to -13 dB so that the sidelobe contributions shown in Figure 4.6 are not considered.

At the MS, the first square MEA, Tx1, is considered and at the BS, BS1, one of the vertical dipoles of the MEA is chosen. Considering this example, the assumption of uniformly distributed scatterers does not hold for this indoor-to-indoor radio channel. It appears that in some cases the DoA presents a multi clustered behavior and therefore, it is difficult to obtain a meaningful value of PAS.

Furthermore, Figure 4.8 presents an example of the classification of the measured paths, i.e., a LOS or NLOS situation. From the 7 different paths of the MS, different *K-factor* values were computed and the classification performed. Each path is presented
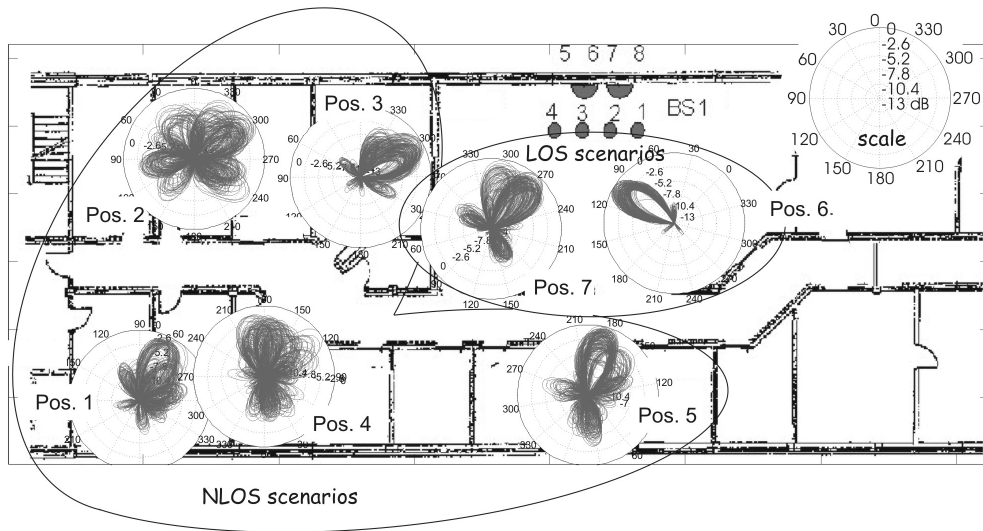
Figure 4.8: *Illustration of the NLOS (Pos. 1 to 5) and LOS (Pos. 6 to 7) classification for novi2, small indoor offices illustrated in Figure 3.12.*

in Table 4.3 along with the corresponding classification.

The DoA analysis, mapped on to the office plan, indicates that Pos.6 and Pos.7 are in a LOS situation and as expected exhibit the highest *K-factor*. Note that Pos.3 indicates high *K-factor* for a NLOS scenario since the wall does not provide a strong obstruction to the direct signal. For indoor environment, the *K-factor* cannot be expected to be of a very high value in a LOS situation since in small offices the magnitude of the direct signal is only marginal to the magnitude of the reflected signal especially in environments with small offices.

Paths	Propagation scenarios	K-factor	
		MEA: Tx1-BS$_{dipole}$	MEA: Tx2-BS$_{dipole}$
Pos. 1	NLOS	0.7	1.2
Pos. 2	NLOS	0.6	0.9
Pos. 3	NLOS	0.9	1.4
Pos. 4	NLOS	0.5	0.6
Pos. 5	NLOS	0.8	0.5
Pos. 6	LOS	2	2.1
Pos. 7	LOS	1.4	1

Table 4.3: *Propagation selection (LOS, NLOS) with their respective* K-factor.

4.3.3.2   Situation where WSS Hold

Figure 4.9 presents 16 illustrations of the DoA estimation versus the displacement of the square MEAs for a LOS scenario measured at the airport. The rows represent the DoA estimation from the two square MEAs at the MS (Tx1 and Tx2) and the columns represent the elements of the two MEAs. Columns {1-4} are the vertical dipoles of the first linear MEA and columns {5-8} represent the patch antennas, i.e., {5,7}: vertical (90°) and {6,8}: horizontal (0°).

For each graphic, the Y-axis represents the angle of arrival in degrees, i.e., from 0° to 360° and the X-axis represents the distance d traveled by the square MEA in wavelengths, i.e., $0.6\lambda \leq d \leq 10.4\lambda$. The reference point is taken from the center of the square MEA. The results of each graphic are normalized to the maximum value of the dipole and patch MEAs for column {1-4} and {5-8} respectively so that the difference in the BPR is taken into account. The results are limited down to -13 dB in the illustration due to the appearance of the first side lobe shown in Figure 4.6.
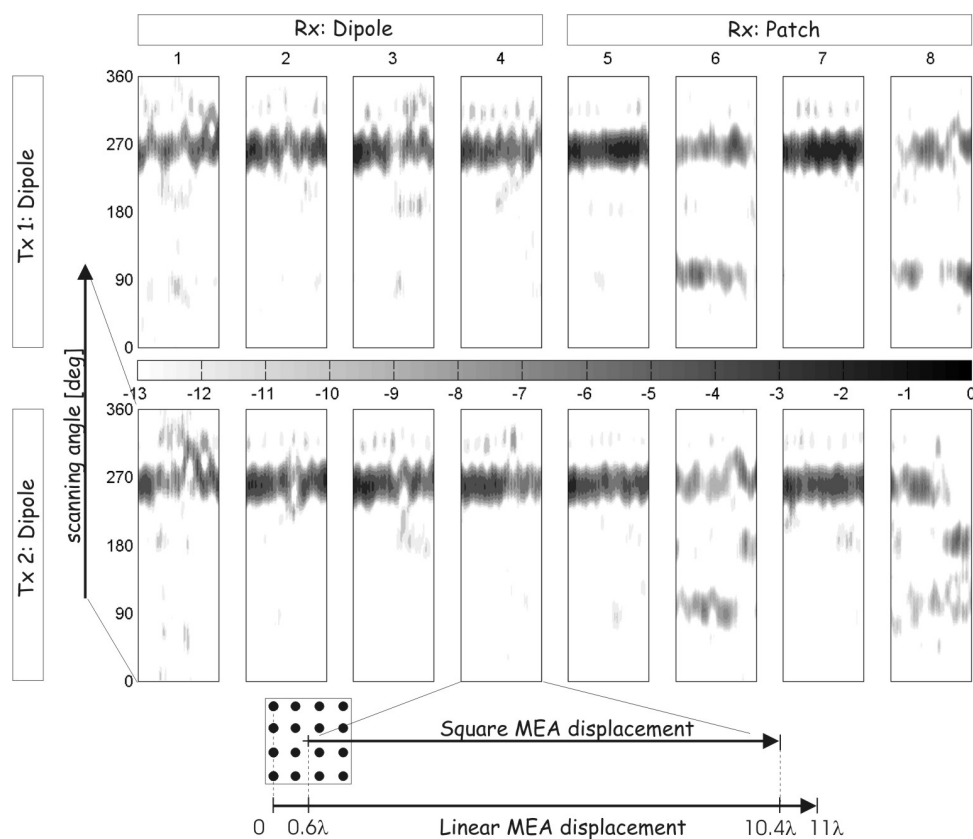

Figure 4.9: Example of a DoA estimation along the slide. WSS condition respected.

When considering the PAS for the Rx element {1-4} and {5,7}, the energy is confined

to a LOS scenario since both Tx and Rx elements have the same polarization. In the PAS seen from the elements {6,8} more components contribute to the PAS since their polarization is different from the TX. The vertically transmitted signal needs to go through a richer scattering process to get cross-polarized for the horizontally polarized element {6,8} and therefore the LOS is not sufficient in this case. Normal reflections on smooth surfaces preserve the polarization of the incident wave and to achieve cross-polarization oblique reflections and or irregular surfaces are necessary.

The WSS condition is respected since there are no differences in the DoA estimation and the fading statistics remain unchanged along all the displacements since all the energy is coming from a similar cluster. Also the PAS results from the first square MEA, Tx1, are similar to those obtained with the second square MEA, Tx2.

4.3.3.3 Situation where WSS does not Hold

In Figure 4.10, the PAS from Tx1 is not the same as the PAS from Tx2. Furthermore, when looking at Tx2, the PAS estimation at the Rx elements {1,2} are different, even though they have the same polarization and are closely spaced.
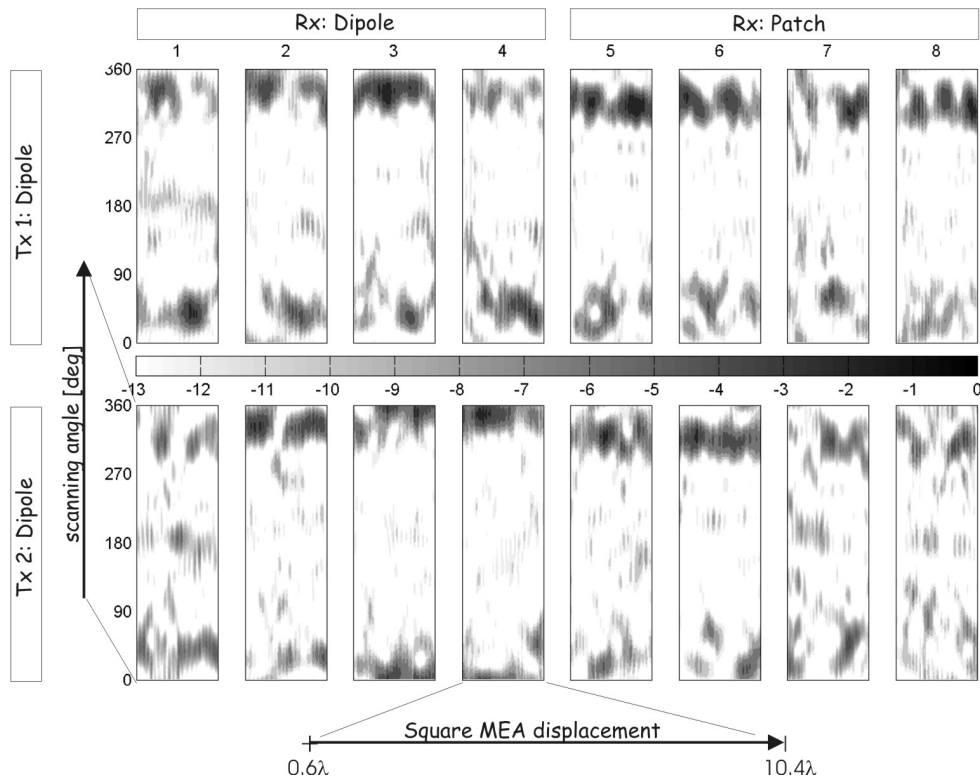

Figure 4.10: Example of a DoA estimation along the slide. WSS condition not respected.

Also, the Rx element {1} shows that for the same run the PAS is extremely variable meaning that different clusters contributes to the statistic of the signal within a run, which indicates that the WSS condition is not respected during that measurement.

4.4 Power Correlation Coefficient Analysis

Four different power correlation coefficients are investigated in this thesis. They are defined and listed as follows

① The **spatial correlation coefficient** is the correlation coefficient between two elements of same polarization but separated by a spatial distance Δi. To facilitate the interpretation of the results, the spatial correlation between the elements is divided into three categories with different Δi. It is denoted $|\rho_{S_{\Delta i}}|$. Table 4.4 summarizes the three categories per project.

② The **polarization correlation coefficient** represents the correlation coefficient between two elements of different polarizations, but identical radiation patterns [3] and no spatial separation. It is denoted $|\rho_P|$.

③ The **joint spatial-polarization correlation coefficient** refers to the correlation coefficient between two elements of different polarizations, separated by a given spatial distance Δi, and identical radiation patterns. It is denoted $|\rho_{S_{\Delta i}\&P}|$.

④ The **joint pattern-spatial-polarization correlation coefficient** refers to the correlation coefficient between two elements of different polarizations, with two different radiation patterns and separated by a given spatial distance Δi. It is denoted $|\rho_{R\&P\&S_{\Delta i}}|$.

4.4.1 Spatial Domain

The spatial power correlation coefficient $\rho_{S_{\Delta i}}$ was computed for all the 79 picocell paths and 28 microcell paths. To provide a better overview of the correlation coefficient behavior with respect to each cell type, i.e., microcell vs. picocell, the cdfs of the correlation coefficient are presented per cell and for several spatial element separations Δi. At the MS, the dipole element of the different MEA projects is considered and at the BS, the dipole and the $+45°$ elements are used for the METRA and the SUNBEAM project respectively (see Table 4.4).

Figure 4.11 presents the cdf of the spatial power correlation for the picocell environment. Figure 4.11 (i) illustrates the correlation coefficient behavior at the MS and Figure 4.11 (ii) at the BS. Figure 4.12 illustrates the cdf of the correlation coefficient

---

[3]Note that due to the reasonable similarity between the radiation pattern in the XZ and YZ planes, it is assumed that the pathch antenna radiation pattern is rotationally symmetric.

Project	SUNBEAM		METRA	
Location	MS	BS	MS	BS
Polarization	vertical	$+45°$	vertical	vertical
$\Delta 1$	0.5λ	0.45λ	0.4λ	1.5λ
$\Delta 2$	1.0λ	0.9λ	0.8λ	3.0λ
$\Delta 3$	1.5λ	1.35λ	1.2λ	4.5λ
MEA set-up	⌊⌊⌊⌊ MS	↖↖↖↖ BS	⌊⌊⌊⌊ MS	⌊⌊⌊⌊ BS

Table 4.4: *3 categories of spatial correlation coefficient with respect to the spacing between elements.*

for the microcell environment for the METRA project and Figure 4.13 the SUNBEAM project. Conclusions based on the cdfs of the three figures are commented simultaneously.

The cdfs have to be read such that, for instance in Figure 4.11 (i), *for 50 % of the measured paths, for the picocell environment, the spatial power correlation at the MS for elements separated by 0.4λ is less than 0.25.*

(i) MS (ii) BS
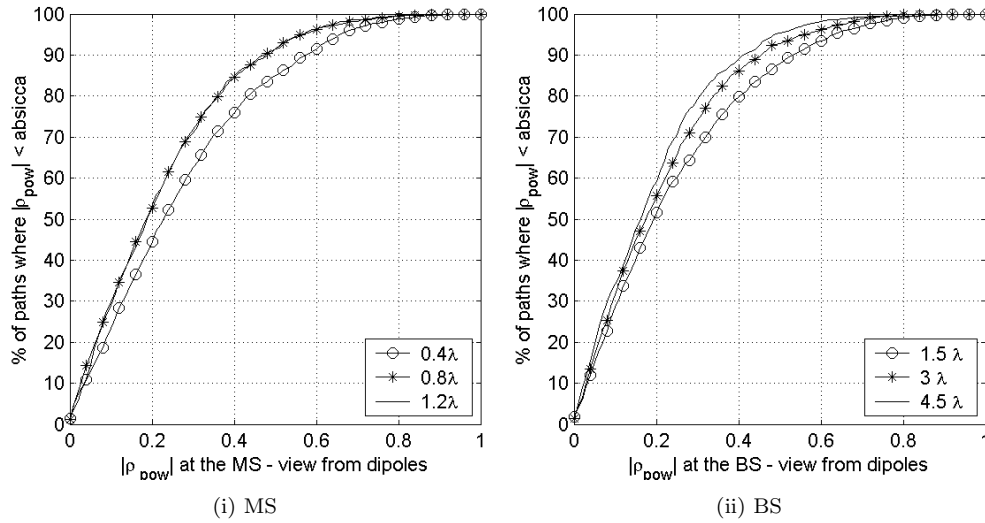
Figure 4.11: *Empirical cdf of the power $|\rho_{S_{\Delta i}}|$ for the picocell environments.*

At the MS, the correlation coefficient is low, $|\rho_{pow}| \leq 0.6$ for 90% of the measured paths for the picocell and microcell considering the small spatial separation, i.e, $\Delta_1 \leq 0.5\lambda$ to $\Delta_3 \leq 1.5\lambda$. The correlation coefficient behavior either in the picocell scenario or in the microcell scenario is similar at the MS since the MS remains indoor and therefore illuminates the same scatterers.

(i) MS   (ii) BS

Figure 4.12: Empirical cdf of the power $|\rho_{S_{\Delta i}}|$ for frb7 microcell environments—courtyard and parking—(METRA project).

(i) MS)   (ii) BS
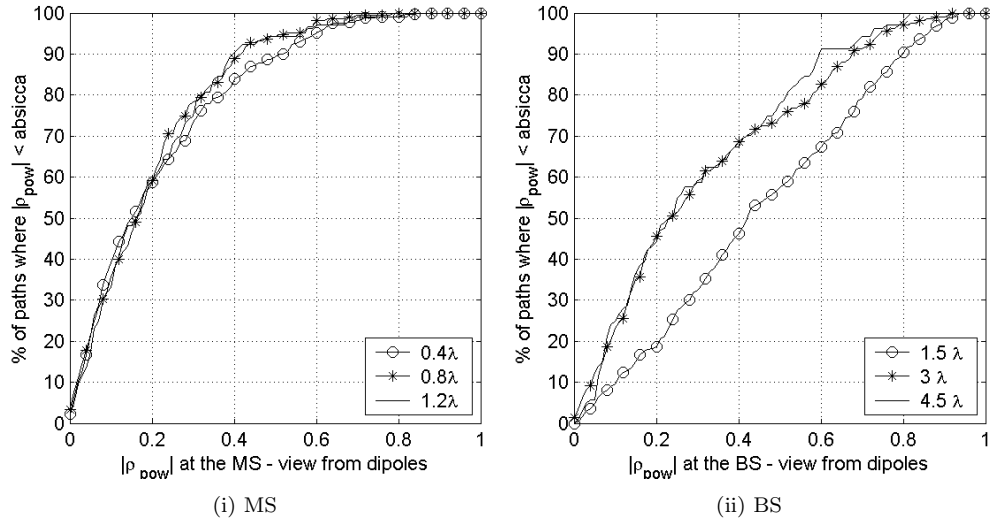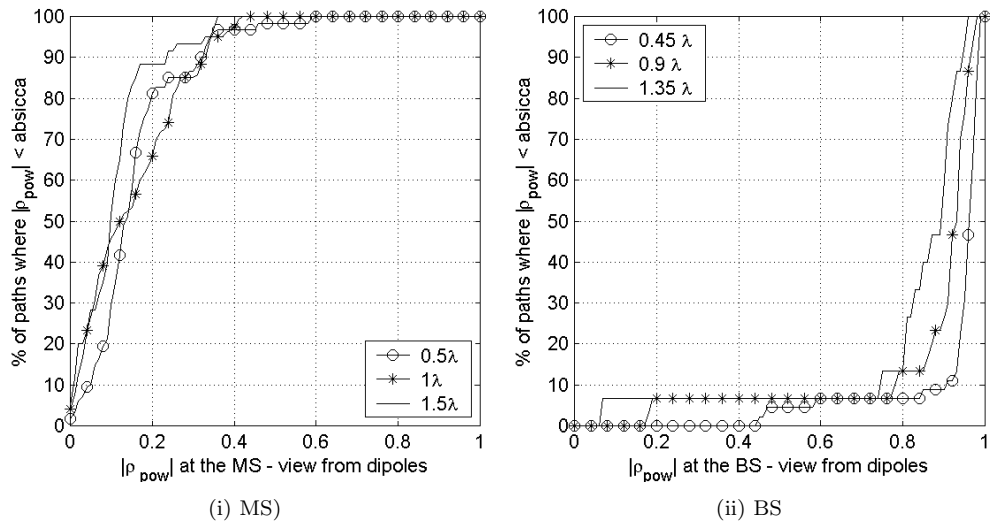
Figure 4.13: Empirical cdf of the power $|\rho_{S_{\Delta i}}|$ for novi2 microcell environments (SUNBEAM project).

At the BS, the correlation coefficient is low for the picocell, $|\rho_{pow}| \leq 0.6$ for 90% of the measured paths. This is to be expected with a larger separation between the elements of the MEAs ($1.5\lambda \leq \Delta i \leq 4.5\lambda$) and the rich indoor scattering.

For microcell environments investigated in the context of the METRA project, Figure 4.12 (ii), the smallest separation 1.5λ indicates a higher level of correlation than for the rest of the separation, i.e. $|\rho_{pow}| \leq 0.85$ for 90% of the measured paths for a spacing of 1.5λ whereas $|\rho_{pow}| \leq 0.65$ for 90% for $\Delta_i \geq 3\lambda$.

For the microcell environments investigated in the context of the SUNBEAM project, the correlation at the BS is very high, $|\rho_{pow}| \geq 0.95$ for 90% of the measured paths, due to the low antenna separation and the low AS experienced in this environment.

Therefore, from a system perspective the deployment of spatial diversity at the BS is not recommended in this environment unless a separation larger than 4.5λ is used.

The empirical cdf of $\rho_{S_{\Delta i}}$ was calculated for each of the 7 environments independently to one another considering their 50% and 90% percentage levels of their respective number of measured paths are summarized in Tables G.1 and G.2 in Appendix G.1 on page 155. An example of the cdf of the correlation coefficient for novi2 is also presented in Figure G.2.

4.4.2 Polarization, Joint Spatial-Polarization and Joint Pattern-Spatial-Polarization Domain

The investigation of the spatial correlation behavior of the MEA showed that spatial diversity technique could be easily employed in the indoor environment. However, when considering microcell environments, spatial diversity has to be obtained at the expense of a large antenna separation. This highlights the fact that when deploying the MIMO technology in wireless systems, the main question is *how to get enough decorrelation at both ends of the antenna system?* The alternative is to consider other diversity techniques to achieve low correlation values *all the time.*

Joint spatial-polarization diversity is interesting in the sense that the correlation coefficient is the product of the correlation coefficient in the polarization and the correlation coefficient in the spatial domain as reported in [132, equation (9)] for microcell environment so that

$$|\rho_{S_{\Delta i}+P}| = |\rho_{S_{\Delta i}}|.|\rho_P| \tag{4.6}$$

An analysis of this property based on the measured data for picocell and microcell environment of the PhD programme as been carried out to illustrate the work of [132] and is presented in Appendix G.4 on page 157.

To simplify the study, this section addresses the analysis of the power correlation coefficient considering vertically polarized dipole reference antennas, defined at the

MS as

$$\rho_{n1n2,\,pow}^{MS} = \left\langle |\alpha_{mn1}|^2, |\alpha_{mn2}|^2 \right\rangle \tag{4.7}$$

where m is the element vertically polarized and $n1$, $n2$ have different polarizations and radiation patterns, and defined similarly at the BS as

$$\rho_{m1m2,\,pow}^{BS} = \left\langle |\alpha_{m1n}|^2, |\alpha_{m2n}|^2 \right\rangle \,, \tag{4.8}$$

where n is the element vertically polarized and $m1$, $m2$ have different polarizations and radiation patterns.

4.4.2.1   Analysis at the MS

This analysis is very similar to the one presented earlier in the spatial domain. This analysis focuses on the METRA measurement data only. Recall, that three different MEAs configuration were deployed at the MS, namely vertical, horizontal 1 and horizontal 2.

vertical   horizontal 1   horizontal 2
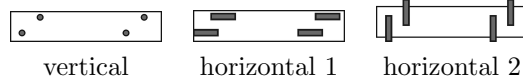
Assuming that the radio channel was stationary for the duration of time spent in one path, it is possible to synthetically combine the MEAs configurations to obtain hybrid MEAs. Table 4.5 presents the possible power correlation coefficients at the MS which are extracted from the hybrid MEA set-ups based on the measured data. This table is written in a symmetrical matrix format meaning that the upper triangular is only considered since the lower triangular is the same.

Figures 4.14 (i) and 4.14 (ii) present the cdfs of all the correlation coefficient combinations for the picocell and microcell environments, respectively. The cdfs of all the combinations can be compared with the cdf of the spatial correlation coefficient analysed earlier.

The results of Figure 4.14 show that even though spatial correlation values were low, introducing another polarization—with another radiation pattern— ($\rho_{R\&P\&\Delta i}$) provides even lower values. Also when spatial diversity is combined with radiation pattern diversity ($\rho_{R\&\Delta i}$), a low correlation value is provided. This conclusion is valid for both picocell and microcell environments. The cdf of the different correlation combination are very close to each other. Except for the spatial diversity, the values of correlation at 50% and 90% percentage levels extracted from Figure 4.14 are less than 0.15 and 0.35 respectively. This means that when the MIMO technology is to be deployed in indoor environment low correlation should be expected between the MEAs' elements.

The results of the correlation coefficient for the hybrid set {vertical and horizontal 1} and the hybrid set {vertical and horizontal 2} are similar. This is an interesting result since the outage correlation remains the same regardless of the orientation of the horizontal dipole in indoors.

$|\rho_{pow}|$		vertical				horizontal 1				$\cdots$
		1	2	3	4	1	2	3	4	$\cdots$
vertical	1	1	$S_{\Delta 1}$	$S_{\Delta 2}$	$S_{\Delta 3}$	R&P	R&P&$S_{\Delta 1}$	R&P&$S_{\Delta 2}$	R&P&$S_{\Delta 3}$	$\cdots$
	2		1	$S_{\Delta 1}$	$S_{\Delta 2}$	R&P&$S_{\Delta 1}$	R&P	R&P&$S_{\Delta 1}$	R&P&$S_{\Delta 2}$	$\cdots$
	3			1	$S_{\Delta 1}$	R&P&$S_{\Delta 2}$	R&P&$S_{\Delta 1}$	R&P	R&P&$S_{\Delta 1}$	$\cdots$
	4				1	R&P&$S_{\Delta 3}$	R&P&$S_{\Delta 2}$	R&P&$S_{\Delta 1}$	R&P	$\cdots$
horiz. 1	1					1	$S_{\Delta 1}$	$S_{\Delta 2}$	$S_{\Delta 3}$	$\cdots$
	2						1	$S_{\Delta 1}$	$S_{\Delta 2}$	$\cdots$
	3							1	$S_{\Delta 1}$	$\cdots$
	4								1	$\cdots$
horiz. 2	1									$\cdots$
	2									$\cdots$
	3									$\cdots$
	4									$\cdots$

$\cdots$	horizontal 2			
$\cdots$	1	2	3	4
$\cdots$	R&P	R&P&$S_{\Delta 1}$	R&P&$S_{\Delta 2}$	R&P&$S_{\Delta 3}$
$\cdots$	R&P&$S_{\Delta 1}$	R&P	R&P&$S_{\Delta 1}$	R&P&$S_{\Delta 2}$
$\cdots$	R&P&$S_{\Delta 2}$	R&P&$S_{\Delta 1}$	R&P	R&P&$S_{\Delta 1}$
$\cdots$	R&P&$S_{\Delta 3}$	R&P&$S_{\Delta 2}$	R&P&$S_{\Delta 1}$	R&P
$\cdots$	R	R&$S_{\Delta 1}$	R&$S_{\Delta 2}$	R&$S_{\Delta 3}$
$\cdots$	R&$S_{\Delta 1}$	R	R&$S_{\Delta 1}$	R&$S_{\Delta 2}$
$\cdots$	R&$S_{\Delta 2}$	R&$S_{\Delta 1}$	R	R&$S_{\Delta 1}$
$\cdots$	R&$S_{\Delta 3}$	R&$S_{\Delta 2}$	R&$S_{\Delta 1}$	R
$\cdots$	1	$S_{\Delta 1}$	$S_{\Delta 2}$	$S_{\Delta 3}$
$\cdots$		1	$S_{\Delta 1}$	$S_{\Delta 2}$
$\cdots$			1	$S_{\Delta 1}$
$\cdots$				1

Table 4.5: *Extraction of the possible $|\rho_{pow}|$ at the MS from the measured data. R: radiation pattern, P: polarization, $S_{\Delta i}$: spatial with separation Δi, R&P&$S_{\Delta i}$: joint pattern-polarization-spatial, R&P: joint pattern-polarization.*
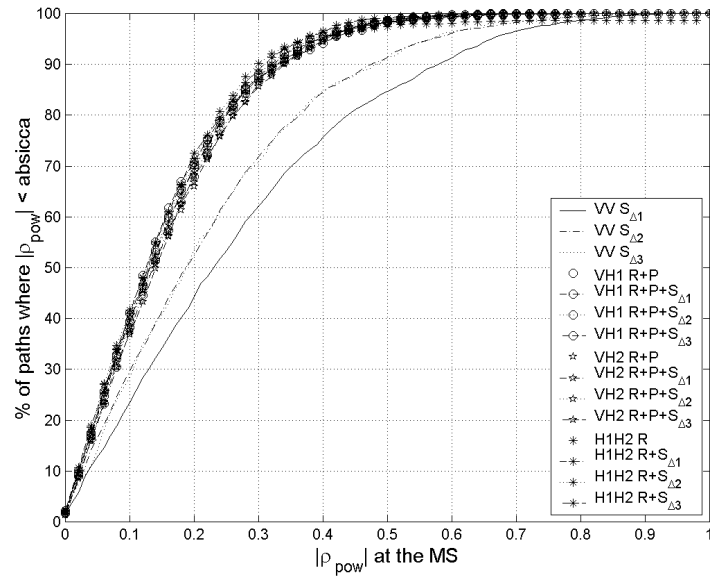
(i) Picocell environments.
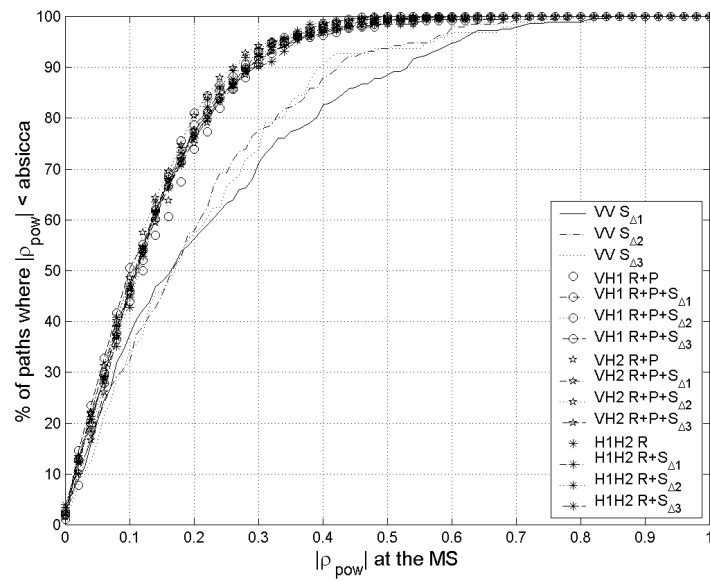
(ii) Microcell environments.

Figure 4.14: Empirical cdf of $|\rho_{pow}|$ at the MS for two cell type (METRA measurement data only).

4.4.2.2 Analysis at the BS

A direct comparison of the correlation coefficient between single polarized and dual polarized antenna configurations is presented here since dual polarized patch antennas with the same radiation pattern were employed at the BS.

Recall the two orientations in the patch antenna for the picocell measurement as illustrated in Figure 4.15. The patch is orientated $\pm 45°$ for the picocell environment novi2, novi3, nokia and $90°/0°$ for fb7b2, and the airport. This difference in the patch orientation influences the correlation coefficient and also the BPR. This is very important and the consequences are treated in detail in Chapter 6 on page 109. For the microcell measurement, two experimental set-ups are used with also two orientation. The METRA measurement taken in frb7 used $90°/0°$ patch orientation and the SUNBEAM project (novi2) considered $\pm 45°$ orientation as recalled in Figure 4.16 below.
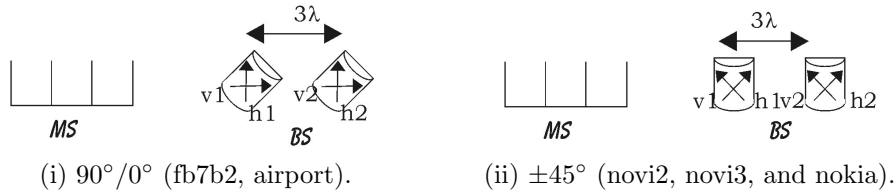

(i) $90°/0°$ (fb7b2, airport). (ii) $\pm 45°$ (novi2, novi3, and nokia).

Figure 4.15: Rotation of the patch at the BS for the picocell environment (METRA).

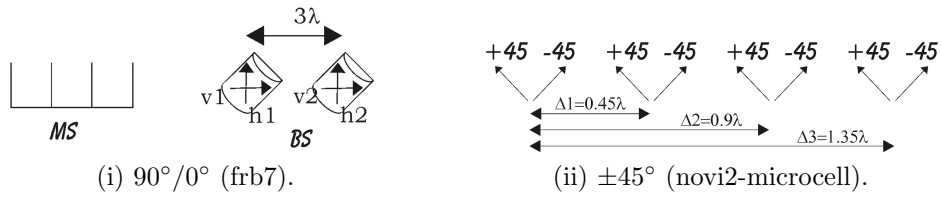(i) $90°/0°$ (frb7). (ii) $\pm 45°$ (novi2-microcell).

Figure 4.16: Rotation of the patch at the BS for the microcell environment (METRA+SUNBEAM).

Similar to the analysis performed at the MS, Table 4.6 describes the different combinations of power correlation coefficients which can be extracted from the measured data at the BS.

$|\rho_{pow}|$	v1	h1	v2	h2
v1	1	P	$S_{3\lambda}$	$P\&S_{3\lambda}$
h1		1	$P\&S_{3\lambda}$	$S_{3\lambda}$
v2			1	P
h2				1

Table 4.6: Extraction of the possible $|\rho_{pow}|$ at the MS from the measured data. P: polarization, $S_{\Delta i}$: spatial with separation Δi. $P\&S_{\Delta i}$: joint polarization-spatial.

Figure 4.17 presents the cdfs for the different correlation coefficient combinations for the picocell environment. Figure 4.17 (i) presents the situation where the BS has the $90°/0°$ configuration, and the vertically transmitted polarized waves need to propagate through a rich scattering environment to be seen by the horizontal elements of the

patch antenna. As a consequence, the correlation coefficient between the vertical and the horizontal element is low but the BPR is unequal (BPR=-8 dB).

In the case of Figure 4.17 (ii), the BS has the $\pm 45°$ configuration. When the MS transmits vertical polarized waves, the waves do not need to go through different scatterers to be seen by the $+45°$ and the $-45°$ subsequently, the correlation coefficient between the $+45°$ and the $-45°$ is high ($|\rho_{pow}| \leq 0.8$ at 90% of the measured paths), but the BPR is equal (BPR=0.9 dB).

(i) $90°/0°$.   (ii) $\pm 45°$.
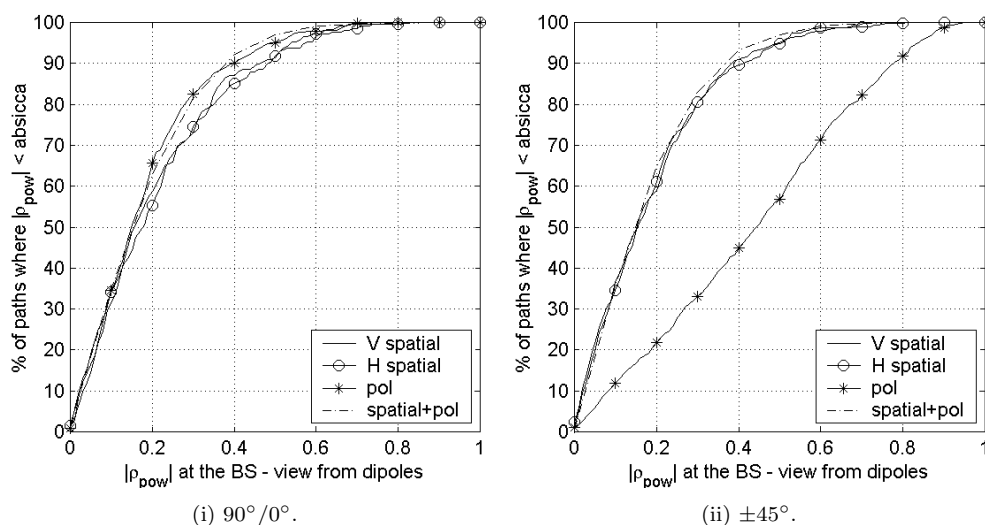
Figure 4.17: Empirical cdf of $|\rho_{pow}|$ at the BS for picocell scenario with respect to the two antenna orientations.

In both graphs, Figure 4.17 (i) and 4.17 (ii), the range of correlation values in the spatial domain are identical irrespective of the orientation of the patches. From these results it can be concluded that at the BS, for the picocell environments, the orientation of the antenna when considering polarization diversity is of crucial importance if low correlation is necessary between the ports of the MEA.

Figure 4.18 presents the results for the microcell environments. In Figure 4.18 (i), the elements are $90°/0°$ orientated (Figure 4.16(i)), i.e., based on the measurements taken in the context of the METRA project, whereas Figure 4.18 (ii) presents the microcell investigated during the SUNBEAM project where the elements are $\pm 45°$ orientated.

As expected the power spatial correlation coefficient for the SUNBEAM project in Figure 4.18 (ii) is high due to the low spatial separation between the elements of the MEA and the existence of a low AS in more than 90% of the measured paths. The spatial power correlation coefficient for the frb7 environment is not as high as for the SUNBEAM, at 90% of the measured paths $|\rho_S| \leq 0.75$.

The important conclusion is that in both graphs of Figure 4.18, the polarization di-
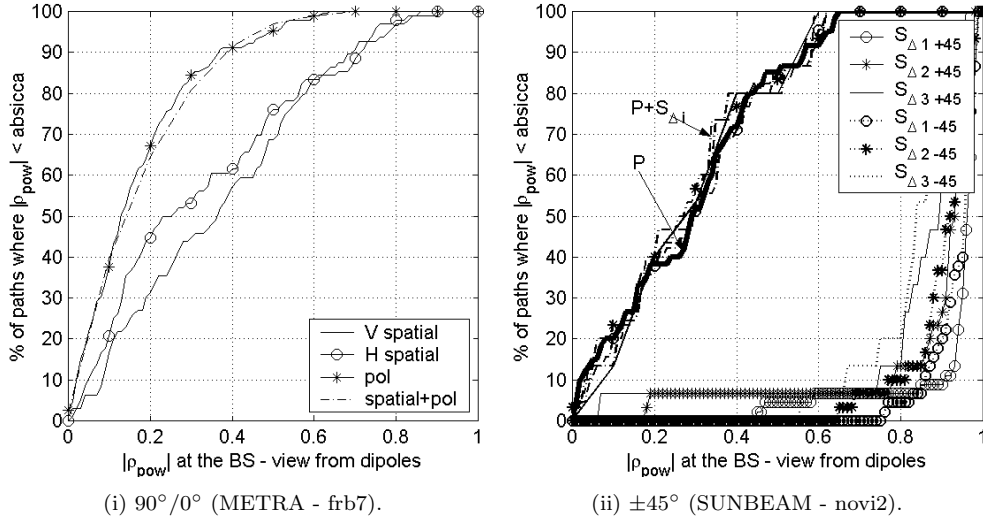
(i) 90°/0° (METRA - frb7).　　　　(ii) ±45° (SUNBEAM - novi2).

Figure 4.18: Empirical cdf of $|\rho_{pow}|$ at the BS for microcell scenario with respect to the two measurement set-up.

versity is a solution to achieve low correlation values compared to spatial diversity for microcell environments irrespective of the orientation of the patches. Joint spatial-polarization diversity technique represents the ultimate solution to obtain the lowest correlation values.

A summary of the results at 50% and 90% level for the picocell and the microcell environments can be found in Table G.3 in Appendix G.

4.5　Reference Propagation Paths

In the rest of the thesis six specific paths have been selected and used to present the behavior of the MIMO technology performances. The selection of these six paths is motivated by their differences in terms of their propagation properties.

4.5.1　Example 1

Example 1 is a **partially decorrelated** scenario. At both the MS and the BS the correlation coefficient values are low. This is one of the paths from the picocell novi2 environment (several small offices environment). See its location on page 41.

4.5.2 Example 2

Example 2 represents the opposite situation to Example 1. The propagation scenario is **partially correlated**: this appears in one of the paths of the novi2-microcell environment extracted during the SUNBEAM project. The AS, at the BS, is about 3°; as a result, the correlation coefficients between elements of same polarization are very high since all the energy received at the BS is confined to a narrow beam. The correlation coefficient at the MS is very low since the scattering in the indoor environment is rich enough so that only a small antenna separation of the order of 0.5λ is required to decorrelate signals. The measured signals from this example are Rayleigh distributed. See its location on page 132.

4.5.3 Example 3

Example 3 is a **partially correlated** scenario taken from the same environment as Example 2. However, contrary to Example 2, the measured signals indicate a Rice distribution with a *K-factor* of 3. See its location on page 132.

4.5.4 Example 4

Example 4 is a **partially decorrelated** scenario, extracted from the same set of measured data as for Example 2 and Example 3 (microcell novi2). An AS of approximately 20° has been identified; as a result, the correlation coefficient values are very low. The large AS experienced is explained by the presence of buildings located near the measurement paths. At the indoor MS, the situation is similar than for Example 2 and Example 3, i.e., low correlation. See its location on page 132.

4.5.5 Example 5

Example 5 is a **partially decorrelated** scenario, extracted from the nokia environment (a modern open office). The spatial correlation coefficients at both the BS and MS are very low. This particular example provides information for patch MEA being ±45° orientated. The measured signal are Rayleigh distributed. See its location on page 125.

4.5.6 Example 6

Example 6 exhibits the same spatial correlation and statistical distribution characteristics as Example 5 (**partially decorrelated** and Rayleigh distributed). It has been extracted from the Airport environment (a large open area). This particular exam-

ple provides information for patch MEA being 90°/0° orientated. See its location on
page 129.

4.6   Summary and Interim Conclusion

In this chapter a large number of topics related to the propagation aspect of the MIMO
technology has been addressed.

Description of the post-processing of the measured data has been presented. It was
shown that due to the low dispersivity of the radio channel and the time resolution of
the measurement system, the measured data were exploited in their NB post-processed
format.

The statistical distribution of the NB signal has been investigated in terms of the
K-factor. At the same time a DoA analysis was performed. The two information
sources were used together to categorise the environment investigated in terms of
their LOS/low AS or NLOS/high AS characteristics.

Based on the DoA analysis applied to the measured data it was concluded that the
angular distribution of the wave in indoor does not necessarily follow a uniform distri-
bution but more a cluster type. From this, a meaningful PAS value could not be easily
calculated. Furthermore, the DoA analysis enable to conclude whether the WSS re-
quirement would hold for the measured data. It was shown that some measured paths
did not hold such a requirement.

A detailed analysis of the power correlation coefficient has been performed in this
chapter so that the performance of the MIMO technology developed in Chapter 6 can
be explained. The analysis considered the spatial correlation coefficient, the polar-
ization correlation coefficient, the joint spatial-polarization correlation coefficient, and
the joint pattern-spatial-polarization correlation coefficient. The results are based on
measured data for different cell environment, i.e., picocell and microcell, and different
antenna configuration.

It was concluded that at the MS and the BS, for picocell environments, elements
separated by 0.4λ would provide low correlation. For microcell environments, the
correlation coefficient at the MS is also low. This is however not the case at the
BS. Large separation would be required to achieve low correlation coefficient when
spatial diversity is to be implemented. When polarization diversity is implemented, the
orientation of the elements is of critical importance since for a low correlation between
elements an unequal BPR may be occurring which results in a drastic deterioration of
the MIMO technology performance. It is also shown that the joint spatial-polarization
diversity technique represents the ultimum solution to obtain the lowest correlation
value for picocell and microcell.

Chapter 5

MIMO Modelling and Empirical Validation

5.1 Introduction

The idea of the members of the CPK group was to develop a stochastic MIMO model [57] taking into account the partial correlation of the radio channel keeping in mind that a model—to be interesting and used by other parties for simulations— needs to be simple and computationally efficient. This chapter presents the empirical validation of that model.

This stochastic model relies on findings already published in the literature regarding propagation in SIMO systems. A small set of parameters, namely the Power Delay Spectrum (PDS) (in the narrowband condition this reduces to one tap only), the Doppler spectrum and two correlation matrices describing the correlation properties at the two ends of the path, are necessary to fully characterise the communication scenario. These parameters can be extracted from measurement campaign results, but they could also be extracted from SIMO radio channel models [133][134][135][79][136]. In [137], parameters are provided to the model based on the characterisation performed in the present work. Also, regarding the 3GPP standardisation of the spatial channel models, the input parameters of the model presented in this thesis [10] are still under discussion in ad-hocs groups at the completion of this thesis [11] [138] [73].

The model presented in this thesis was first reported in [57] using the power correlation definition. Later during the 3GPP standardisation process, a consensus was reached, according to which the correlation definition was to be based on the complex information of the received signals. Even though the validation process has been performed on the basis of both power and complex definitions, the rest of the thesis considers only the complex version of the model.

The validation of this stochastic radio channel model is supported by measurement campaign results. The experimental validation of the model makes it extremely attractive since it illustrates how well the model matches reality. The validation procedure of the model follows two steps. The first step focuses on a local validation, meaning that only one path is considered at a time. The second step is a global validation, i.e. considering all the measured paths at once, so that an estimation error between the simulated and the measured data can be derived. The validation is performed under the NB condition in the spatial and polarization domain.

This chapter is divided into three main parts. The first one addresses the definition of the stochastic MIMO model. The second part treats the validation of the model in the spatial and finally the third part concentrates on the polarization domain.

5.2 The MIMO Radio Channel Model

The general MIMO radio channel structure has been defined in Section 2.2 on page 11. The WB MIMO radio channel model proposed in [57] is presented here in a NB format since the validation is performed under the NB condition.
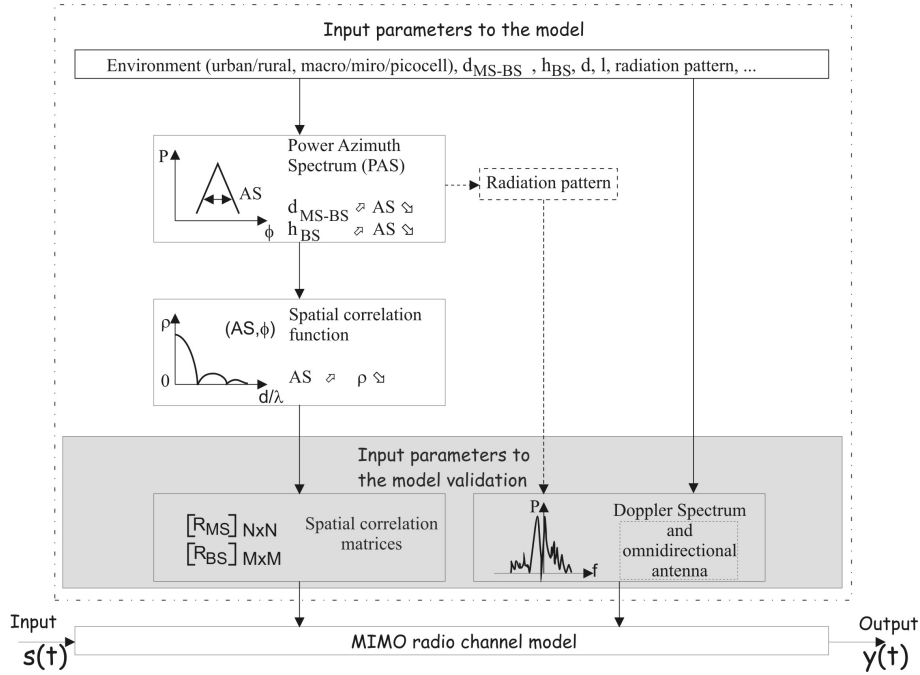

Figure 5.1: *Functional sketch of the MIMO model. d_{MS-BS} stands for the distance between MS and BS, h_{BS} for the height of the BS above ground floor, AS for the Azimuth Spread. These parameters can easily be found in the SIMO literature. Note that the grey area outlines the input parameters used in the validation of the model.*

An illustration of the model presented in this thesis is given in Figure 5.1. The sketch diagram indicates the two main parts:

① The input parameter block.

② The MIMO radio channel model block with its input $\mathbf{s}(t)$ and output $\mathbf{y}(t)$.

The input parameter block can be divided into validation (shadowed) and normal (non-shadowed) mode. The shadowed part is the focus of this chapter as it suffices for the model validation process. The non-shadowed area illustrates how SIMO radio channel information can be used to provide input to the MIMO model when applying the stochastic model, though this is not within the scope of the thesis.

This section is divided into four important subsections. First the three assumptions to the model are presented. Next, the input parameters of the model used to validate the model are introduced. The third subsection consists of a description of how to apply the model using the input parameters. Finally the last subsection describes the limitations to the model.

5.2.1 Model Assumptions

The MIMO model is based on three assumptions:

① It is assumed that the same radiation pattern is applied to all the elements of the MEA. An example of a MEA topology supported, and not supported by the model is illustrated in Figure 5.2.
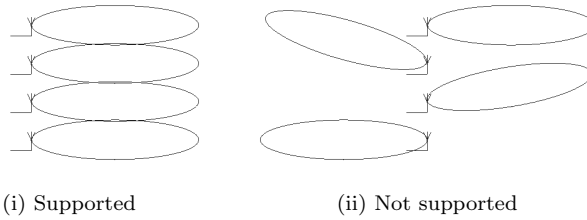

(i) Supported   (ii) Not supported

Figure 5.2: Illustration of the assumption on the antenna configuration.

If the radiation patterns are not identical or they point in different directions[1], i.e. like in the case of body worn devices influenced by near field effects, the generation of the spatial correlation matrix through a Kronecker product would not be valid (see the Kronecker product in (5.7)). To overcome this problem, the solution would be to generate $\mathbf{R}_{MIMO}$ from measured data or from another model and the generation of correlated signal could still be implemented in a

---

[1] Therefore illuminating different scatterers.

simple and computationally efficient manner adequate for link level simulation as described in more detail in Figure 5.4.

② The potential gain of the MIMO concept strongly depends on the correlation coefficient between the elements of $\mathbf{H}$. Let assume that α_{mn} is complex Gaussian distributed with identical average power. The effect of any imbalance in the average power is investigated and presented in more detail in Chapter 6. The complex correlation coefficient at the BS between element m_1 and m_2 is defined as

$$\rho_{m_1 m_2}^{BS} = \langle \alpha_{m_1 n}, \alpha_{m_2 n} \rangle \ . \tag{5.1}$$

From (5.1), it is assumed that the correlation function at the BS is independent of the index n since all the N elements at the MS illuminate the same surrounding scatterers and therefore also generate the same PAS at the BS.

The complex correlation coefficient observed at the MS is similarly defined as

$$\rho_{n_1 n_2}^{MS} = \langle \alpha_{m n_1}, \alpha_{m n_2} \rangle , \tag{5.2}$$

and is assumed to be independent of m, at the BS.

Given equations (5.1) and (5.2), the following symmetrical correlation matrices can be defined as, respectively

$$\mathbf{R}_{BS} = \begin{bmatrix} \rho_{11}^{BS} & \rho_{12}^{BS} & \cdots & \rho_{1M}^{BS} \\ \rho_{21}^{BS} & \rho_{22}^{BS} & \cdots & \rho_{2M}^{BS} \\ \vdots & \vdots & \ddots & \vdots \\ \rho_{M1}^{BS} & \rho_{M2}^{BS} & \cdots & \rho_{MM}^{BS} \end{bmatrix}_{M \times M} \tag{5.3}$$

and

$$\mathbf{R}_{MS} = \begin{bmatrix} \rho_{11}^{MS} & \rho_{12}^{MS} & \cdots & \rho_{1N}^{MS} \\ \rho_{21}^{MS} & \rho_{22}^{MS} & \cdots & \rho_{2N}^{MS} \\ \vdots & \vdots & \ddots & \vdots \\ \rho_{N1}^{MS} & \rho_{N2}^{MS} & \cdots & \rho_{NN}^{MS} \end{bmatrix}_{N \times N} . \tag{5.4}$$

One should note that the correlation coefficient can be taken arbitrary, but must fulfill mathematical laws, to ensure that the correlation matrices are positive semi-definite.

③ The complex correlation coefficient between two arbitrary transmission coefficients connecting two different sets of elements is expressed as

$$\rho_{n_2 m_2}^{n_1 m_1} = \langle \alpha_{m_1 n_1}, \alpha_{m_2 n_2} \rangle , \tag{5.5}$$

which is shown [20] to be equivalent to

$$\rho_{n_2 m_2}^{n_1 m_1} = \rho_{n_1 n_2}^{MS} \rho_{m_1 m_2}^{BS}, \tag{5.6}$$

provided that (5.1) and (5.2) are independent of n and m, respectively. In other words, this means that the spatial correlation matrix of the MIMO radio channel is the Kronecker product of the spatial correlation matrix at the MS and the BS, thus

$$\mathbf{R}_{MIMO} = \mathbf{R}_{MS} \otimes \mathbf{R}_{BS} \tag{5.7}$$

where $\otimes$ represents the Kronecker product[2]. This philosophy was inspired by [132, equation (9)] where it was experimentally justified that the polarization and spatial decorrelation effects are independent and multiplicative in compound antenna systems. This relation has also been confirmed in [139].

This stochastic model implicitly assumes WSS condition since the simulated channel coefficient does not change statistics. The model produces a Rayleigh signals only. A Rice extension of this model has been proposed in [13]. The measured data were essentially Rayleigh distributed therefore the validation focuses on the Rayleigh version of this model.

5.2.2   Input Parameters to the Validation

The two input parameters used in the validation stage are illustrated by the shaded area of Figure 5.1 and they have been extracted from the measurement campaign data. They consist of the average spatial complex correlation matrices $\mathbf{R}_{BS}$ and $\mathbf{R}_{MS}$, and the magnitude average Doppler spectrum.

① The measured spatial complex correlation matrices are the results of an average over the reference elements n and m with respect to which the matrices are computed.

② The average measured Doppler spectrum is obtained by averaging over all the MN radio links and is defined at the MS, since the BS is fixed.

The limitation to the average Doppler spectrum is due to the measurement set-up, but is not inherent to the model. If both MS and BS were moving, the Doppler spectrum of the channels would have been defined as the convolution of the individual Doppler spectra defined either at the MS or at the BS, considering the other end fixed. The phase shifts due to both movements add, causing the respective phases to multiply each other, which is equivalent to the convolution of their Doppler spectra.

Two examples of typical measurement paths are used for the local validation. Their selection is motivated by the differences in terms of their propagation properties. These examples have been introduced in Chapter 5 on page 81 and shortly reminded bellow:

---

[2]Note that this is only valid under the aforementioned condition on the radiation pattern of the MEAs !

☞ Example 1 : This is a partially decorrelated scenario selected from the picocell novi2 environment. The signals are Rayleigh distributed.

☞ Example 2 : This example represents the opposite situation to Example 1 where the propagation scenario is partially correlated: this appears in one of the paths of the novi2-microcell environment. The signals are Rayleigh distributed.

Example 1: Picocell - Partially decorrelated

$$\mathbf{R}_{BS} = \begin{bmatrix} 1 & -0.45+0.53i & 0.37-0.22i & 0.19+0.21i \\ -0.45-0.53i & 1 & -0.35-0.02i & 0.02-0.27i \\ 0.37+0.22i & -0.35+0.02i & 1 & -0.10+0.54i \\ 0.19-0.21i & 0.02+0.27i & -0.10-0.54i & 1 \end{bmatrix}$$

$$\mathbf{R}_{MS} = \begin{bmatrix} 1 & -0.13-0.62i & -0.49+0.23i & 0.15+0.28i \\ -0.13+0.62i & 1 & -0.13-0.52i & -0.38+0.12i \\ -0.49-0.23i & -0.13+0.52i & 1 & 0.02-0.61i \\ 0.15-0.28i & -0.38-0.12i & 0.02+0.61i & 1 \end{bmatrix}$$

Example 2: Microcell - Partially correlated

$$\mathbf{R}_{BS} = \begin{bmatrix} 1 & -0.85+0.46i & 0.76-0.57i & -0.70+0.60i \\ -0.85-0.46i & 1 & -0.95+0.19i & 0.90-0.24i \\ 0.76+0.57i & -0.95-0.19i & 1 & -0.98+0.08i \\ -0.70-0.60i & 0.90+0.24i & -0.98-0.08i & 1 \end{bmatrix}$$

$$\mathbf{R}_{MS} = \begin{bmatrix} 1 & -0.24+0.04i & 0.11+0.11i & -0.13+0.15i \\ -0.24-0.04i & 1 & -0.29+0.06i & 0.14+0.10i \\ 0.11-0.11i & -0.29-0.06i & 1 & -0.29+0.06i \\ -0.13-0.15i & 0.14-0.10i & -0.29-0.06i & 1 \end{bmatrix}$$

Both in Example 1 and Example 2, $|\mathbf{R}_{MS}|^2$ is partially decorrelated with a mean power correlation coefficient values of 0.4 and 0.29 respectively. This is expected since the MS is surrounded by scatterers in both cases. On the other hand, $|\mathbf{R}_{BS}|^2$ presents two different behaviors. In Example 1, the mean power correlation coefficient is fairly low, 0.27, as expected for a cluttered indoor indoor environment, while the spatial correlation coefficients at the BS are highly correlated in Example 2 with a mean power correlation coefficient value of 0.93.

An illustration of the averaged measured Doppler spectrum of Example 1 is presented in Figure 5.3. The spectrum is normalized in frequency to its maximum Doppler shift f_m and in power to its maximum value.

5.2.3   How to Apply the Model

The purpose of the model is to generate simulated partially correlated MIMO channel coefficients α_{mn} from zero-mean complex i.i.d. random variables a_{mn} using the Cholesky decomposition procedure reported in [140]. The practical procedure to obtain α_{mn}, in a MIMO perspective, is sketched in a flow chart in Figure 5.4.
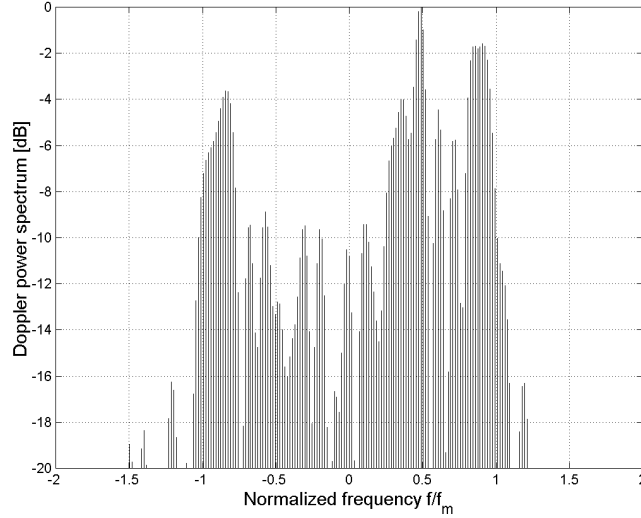
Figure 5.3: Averaged measured Doppler power spectrum for Example 1 (Picocell - Partially decorrelated).

The degree of correlation is defined by the correlation matrix of the MIMO channel $\mathbf{R}_{MIMO}$ derived from the complex average correlation matrix at the MS and the BS, see equation (5.7), and rewritten here for convenience.

$$\mathbf{R}_{MIMO} = \mathbf{R}_{MS} \otimes \mathbf{R}_{BS}$$

The original zero-mean complex i.i.d. random variables a_{mn} have their amplitudes shaped in the frequency domain by the average measured Doppler spectrum and their phases uniformly distributed over $[0, 2\pi]$ and independent from one another such that MN independent and identically distributed variables are generated [141]. Note that when using the model, a simple check can be performed by the user to verify the distribution of the envelope considered.

In Section 5.2.1, it is assumed that each α_{mn} is a complex variable with identical average power. This assumption can easily be relaxed and any imbalance in BPR between elements can be mapped into a matrix $\mathbf{P}$ whose elements are the product of the standard deviations $\sigma_{\alpha_{mn}}$ of the channel radio links α_{mn}. The matrix of the complex covariance coefficient $\mathbf{\Gamma}$ is defined as

$$\mathbf{\Gamma} = \mathbf{R}_{MIMO} \times \mathbf{P} \tag{5.8}$$

where $\times$ represents the element by element multiplication. Consequently, $\mathbf{\Gamma}$ contains the correlation properties of the MIMO radio channel as well as the magnitude of each single radio link.

The symmetrical mapping matrix $\mathbf{C}$, also called the Cholesky triangle, results from the standard Cholesky factorization of the matrix

$$\Gamma = \mathbf{C}\mathbf{C}^T \ , \tag{5.9}$$

provided that Γ is non-singular and the generation of correlated signals can be written as

$$\mathbf{A} = \mathbf{C}\mathbf{a} \tag{5.10}$$

where $\mathbf{A}_{MN\times 1} = [\alpha_{11}, \alpha_{21}, \ldots, \alpha_{M1}, \alpha_{M2}\ldots, \alpha_{MN}]^T$ and $\mathbf{a}_{MN\times 1} = [a_1, a_2, \ldots, a_{MN}]^T$.

Subsequently, the generation of the simulated MIMO channel matrix $\widetilde{\mathbf{H}}$ is a rearrangement of the vector $\mathbf{A}$ so that

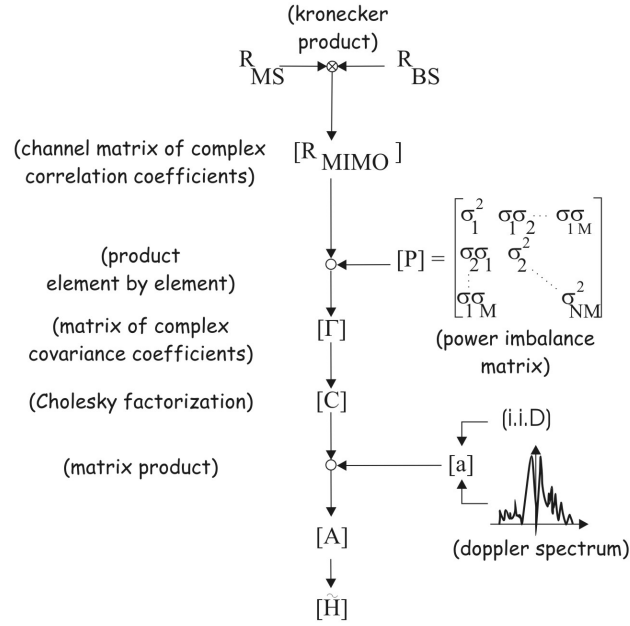$$\mathbf{A}_{MN\times 1} \Rightarrow \widetilde{\mathbf{H}}_{M\times N} \ . \tag{5.11}$$

Figure 5.4: Flow chart of the MIMO model for the spatial domain.

5.2.4 Limitations to the Model

The pin-hole scenario has its defenders; they argue that it exists and therefore should be modelled. However, it still remains the exception to the rule [47]. The aim of the model proposed in [57], redefined here in his NB format, and empirically validated in

this study, is primarily aimed towards a professional audience who seek to employ MIMO technology in realistic mobile scenarios.

This stochastic MIMO radio channel model cannot reproduce the pin-hole effect. The channel transfer matrix of the pine-hole is described in [87] as a dyad with one degree of freedom, where each channel coefficient α_{mn} writes as the product of two independent zero-mean complex Gaussian random variables. Therefore, the linear generation process described by (5.10) can not account for the product of random variables. Note, however, that even though measured data were collected in a variety of environments, the pin-hole effect was not observed.

5.3 Experimental Validation in the Spatial Domain

The purpose of this section is two-fold. First, the assumptions of the model are being validated in the spatial domain. Next the local and global validation procedures are explained along with their outcomes.

5.3.1 Validation of the Assumptions

The fulfillment of the model's assumptions have been verified using a 4×4 MIMO configuration considering dipoles at both the MS and the BS. The assumptions are that (i) the MEA elements have the same radiation pattern (ii) the spatial correlation at the BS (MS) is independent of n (m) respectively and that (iii) the spatial correlation matrix of the MIMO radio channel is the Kronecker product of the spatial correlation matrices at the BS and the MS (5.7).

① $\boxed{\textit{the MEA elements have the same radiation pattern}}$

The radiation pattern of the MEA element has been treated in Chapter 3. Each MEA at both the MS and BS exhibits elements with the same radiation pattern.

② $\boxed{\textit{the spatial correlation at the BS (MS) is independent of } n \textit{ (m) respectively}}$

The std of each measured spatial correlation coefficient $|\rho^{\text{BS}}_{m_1 m_2}|$ and $|\rho^{\text{MS}}_{n_1 n_2}|$ is computed over the N and M reference antennas respectively for each environment. The std at the BS is expressed as

$$std_-\rho^{BS}_{m_1 m_2} = std\left(\left\{|\rho^{nm_1}_{nm_2}|\right\}\right), \quad \forall \ n \in [1\dots4], \tag{5.12}$$

and at the MS as

$$std_-\rho^{MS}_{n_1 n_2} = std\left(\left\{|\rho^{n_2 m}_{n_1 m}|\right\}\right), \quad \forall \ m \in [1\dots4]. \tag{5.13}$$

where $std(.)$ return the standard deviation.

Figure 5.5 presents the cdf of $std\_\rho^{BS}_{m_1 m_2}$ (left graph) and $std\_\rho^{MS}_{n_1 n_2}$ (right graph) computed over the 92 measured paths considered with the METRA measurement setup for the 6 different correlation coefficients, i.e., the upper triangular coefficients of the correlation matrix of the 4x4 MIMO configuration.
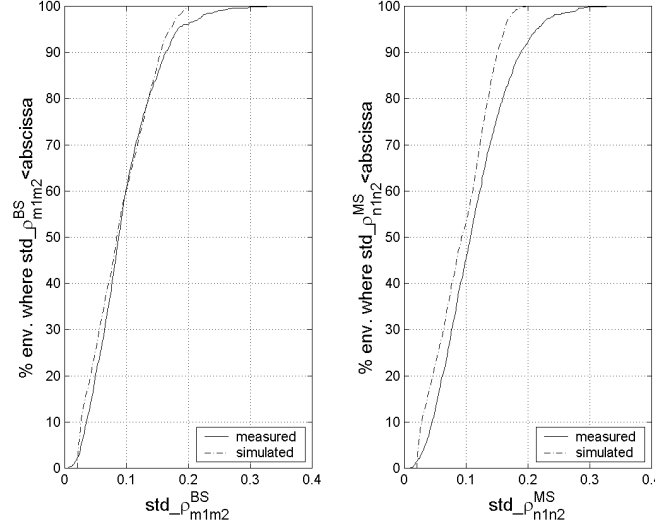

Figure 5.5: *Example of the cdf of $std\_\rho^{BS}_{m_1 m_2}$ (left graph) and $std\_\rho^{MS}_{n_1 n_2}$ (right graph). The cdf is performed over all the measured environments and for all the seven correlation coefficients.*

To validate the statistical significance of the empirical results, the cdf, based on the measured data, is compared to a cdf obtained from simulations performed under similar conditions. For each of the 92×6 different measured correlation coefficients, two correlated, Rayleigh-distributed signals of length 1,000λ, i.e., long enough to achieve enough statistics, are generated. These 1,000λ-long vectors are truncated into 11.8λ-long runs over which the correlation coefficient is computed again. The resulting correlation coefficients exhibit a standard deviation $std_{11.8\lambda}$. This operation is repeated 92×6 times so that a simulated cdf of $std_{11.8\lambda}$ is then obtained under the same conditions as for the measured cdf.

The measured and the simulated cdfs could differ in their respective slope and in their median value. A difference in the steepness of the cdf would indicate a lack of statistics. In the case where the simulated cdf would be generated from an infinite number of realisation, the slope would be vertical. By reducing the amount of statistic the cdf becomes less steeper. On the other hand, the median point of the measured and simulated cdfs would not coincide if assumption (i) were not fulfilled.

The simulated cdf is shown in Figure 5.5. The slope between the simulated and

the measured cdf is similar. The good match between the measured and the simulated cdfs supports assumptions (5.1) and (5.2).

③ $\boxed{\textit{the Kronecker product}}$

The assessment of the Kronecker product assumption in (5.7) is performed by comparing empirical results and simulated results generated from the proposed MIMO radio channel model. The results are presented in the next section.

5.3.2 Validation Procedure

The eigenvalue decomposition (EVD) of the instantaneous correlation matrix $\mathbf{R}$, defined in Section 2.3, has been chosen to serve as a benchmark for the validation process of the MIMO model. In order to consider the qualitative accuracy of the model, a comparison between measured and simulated eigenvalues is performed for 4×4 MEA configuration where at most $K = 4$ distinct eigenvalues can be expected.

For each measurement path, the input parameters are fed into the proposed stochastic MIMO model. A simulation consisting of $q = 1 \ldots 100$ realisations of the MIMO channel produces $\widetilde{\mathbf{H}}_{M \times N \times L}$, where $\widetilde{\mathbf{H}}$ is a three dimensional matrix with L the number of samples in each realisation.

For each realisation q, the simulated $\widetilde{\mathbf{H}}_{4 \times 4 \times L}$ counts as many samples L as in the measured $\mathbf{H}_{4 \times 4 \times L}$ collected during one MEA run, i.e., 20λ or 11.8λ depending on the measurement set-up.

Next, for each realisation q, the instantaneous EVD of $\widetilde{\mathbf{H}}_{4 \times 4 \times l} \widetilde{\mathbf{H}}_{4 \times 4 \times l}^{H}$ is performed for each sample $l = 1 \ldots L$ in order to identify the corresponding simulated eigenvalues denoted by the vector

$$\lambda_{sim\_kq\,L \times 1} = [\lambda_{sim\_kq\ 1}, \ldots, \lambda_{sim\_kq\ l}, \ldots, \lambda_{sim\_kq\ L}]^{T} \ . \tag{5.14}$$

From these eigenvalues, k large vectors $[\lambda_{sim\_k}]_{1 \times QL}$ containing the 100 realisations for the simulated eigenvalues λ_{sim_kp} are deduced so that

$$\lambda_{sim\_k} = \{\lambda_{sim\_kq}\} \ , \tag{5.15}$$

where $\{.\}$ represents a set of variables.

The validation procedure of the model follows two steps. The first step focuses on a local validation, meaning that only one path is considered at a time. The second step is a global validation, i.e. considering all the measured path at once, so that an estimation error between the simulated and the measured data can be derived.

5.3.2.1   Local Validation

The local validation consists of the comparison of the cdf of λ_{meas_k} and λ_{sim_k} for each of the measured paths. Figure 5.6 and Figure 5.7 present the eigenanalysis performed for the two propagation environments, Example 1 and Example 2 respectively. The cdf of a measured SISO system is also plotted along with a Rayleigh curves used as a reference. This Rayleigh curve is produced from a set of samples which have been statistically generated from [142, p. 45].

The cdfs of the measured eigenvalues λ_{meas_k} are computed for a full displacement of the Tx. They are displayed on the same graph with the cdfs of the simulated eigenvalues λ_{sim_k} which cdfs have been derived over the QL variables of the vector λ_{sim_k}. These two figures show that the cdfs of the eigenvalues generated from the stochastic model match well the empirical cdfs.

5.3.2.2   Global Validation

A global analysis encompassing all the measurement paths has been performed to measure the error between the measured and the simulated eigenvalue results. The previous examples, Example 1 and Example 2, are embedded in the global validation. The analysis is based on the difference between λ_{meas_k} and λ_{sim_k} at 50% [3] cdf level for each path and for each eigenvalue such that

$$\Delta_{error\_k} = [\lambda_{meas\_k} - \lambda_{sim\_k}]_{50\%} . \tag{5.16}$$

Figure 5.8 illustrates the cdf of Δ_{error_k} calculated over the 107 investigated paths.

! Some discrepancies between the empirical and the simulated are present due to the fact that the simulated results are based on the average complex correlation matrix and average Doppler spectrum while the measured data are a set of real instantaneous realisations. Therefore, discrepancies may be likely to occur between measured and simulated data in the cases where the measured radio channels do not fulfill the WSS. Finally, the strength of the *K-factor* may contribute to the discrepancy between the measured and the simulated results.

For more clarity in the graph, the absolute value $|\Delta_{error\_k}|$ is considered since the distribution of Δ_{error_k} is bound to be symmetrical around zero. The error generated by the proposed model is bounded for 80% of the paths within ± 0.6 dB for the first simulated eigenvalue λ_1, within ± 1.6 dB for λ_2, ± 2.2 dB for λ_3, and ± 2.6 dB for λ_4. As expected the higher the order of the eigenvalue the bigger is the discrepancy since they are the most affected by the noise.

These $|\Delta_{error\_k}|$ values are considered to be reasonably small and concludes that the proposed stochastic MIMO radio channel model is validated in the spatial domain.

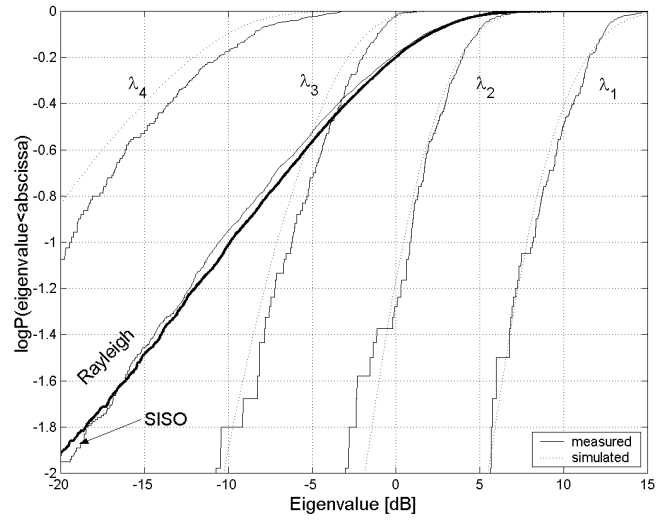[3]50% is equivalent to $log_{10}(0.5) = -0.3$

Figure 5.6: Local validation. Cdf of λ_{meas_k} and λ_{sim_k} for Example 1 (Picocell - Partially decorrelated).
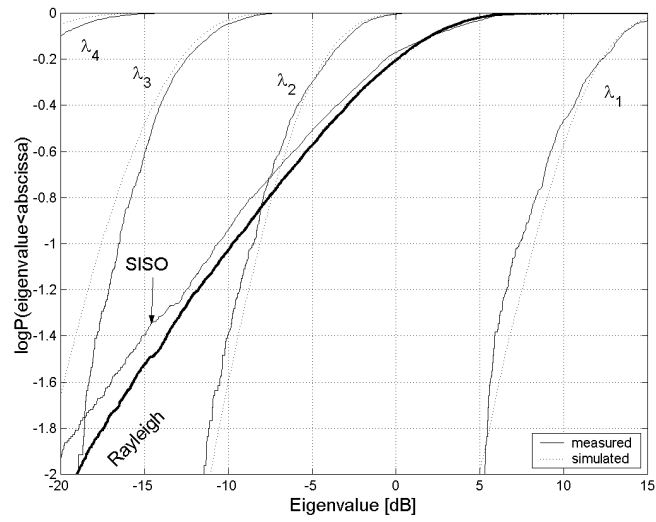

Figure 5.7: Local validation. Cdf of λ_{meas_k} and λ_{sim_k} for Example 2 (Microcell - Partially correlated).
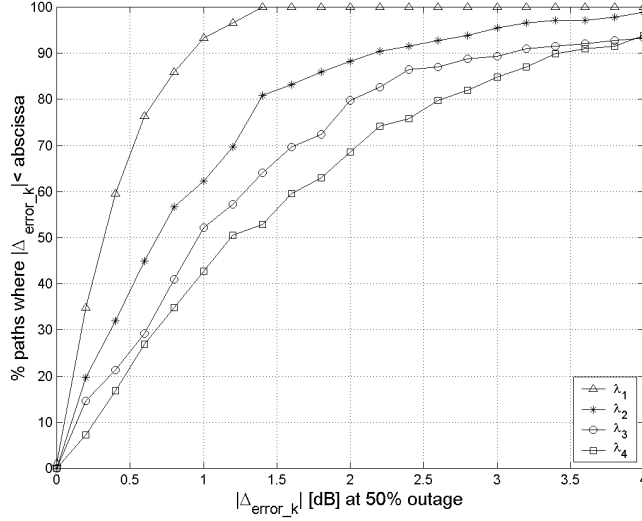
Figure 5.8: Global validation. Cdf of $|\Delta_{error\_k}|$ over all the measurement paths.

5.4 Experimental Validation in the Polarization Domain

The dimensions of a large physical MEA is a general issue of concern for MIMO technology. A solution to mitigate this problem could be the use of dual-polarized antennas hence reducing the size of the MEA compared to only using spatial diversity. Therefore it is important, when modelling the MIMO radio channel, to also consider the validity of the model with respect to the polarization domain.

For clarity in the reading of the thesis, the outcome of the validation procedure in the polarization domain is presented here only, whereas the validation procedure is presented in Appendix C. Two different methods of implementing the modelling of the radio channel in the polarization domain are described depending on the nature of the propagation scattering. These two methods treat the question whether ρ is dependent, or not, of the polarization of the reference element.

In the spatial domain, it was found that ρ is independent of the reference element. In the polarization domain, the first model option considers a *polarization-independent* definition of ρ and the second option a *polarization-dependent* definition. The dependency in the polarization would occur in a strong LOS situation. It was found that the scattering nature of the measured data limited the polarization investigation to only one method, therefore only the first option has been considered in the validation.

Figure 5.9 illustrates the local validation in the polarization domain of Example 1,

but with a different MIMO antenna configuration than for Figure 5.6. At both the MS and BS, the polarization diversity is considered. For this path, $BPR = -7.5 \ dB$ and $BPR = -1.6 \ dB$ were measured at the MS and BS respectively. The eigenvalues are normalized to the mean power of the elements $|h_{V_i V_j}|^2$, where V is implicitly the vertical polarization and i, j the index of the vertical elements. The inspection of the measured and simulated curves of Figure 5.9 indicates that the cdfs of the eigenvalues generated from the stochastic model match the measured eigenvalues well.

A global analysis over all the measured paths of the METRA campaign has also been performed in order to measure the match between the measured and the simulated results. The $|\Delta_{error\_k}|$ is presented in Figure 5.10 and indicates that at 50% cdf level the error is bounded for 80% of the investigated paths within $\pm 0.4 \ dB$ for λ_1, $\pm 1.5 \ dB$ for λ_2 and λ_3, and $\pm 2.4 \ dB \ \lambda_4$. The $|\Delta_{error\_k}|$ generated from $Array_1$ and $Array_2$[4] are almost identical.

These results allow to conclude that the model reproduce realistic MIMO radio channels appropriately when considering polarization diversity for the 1st method.
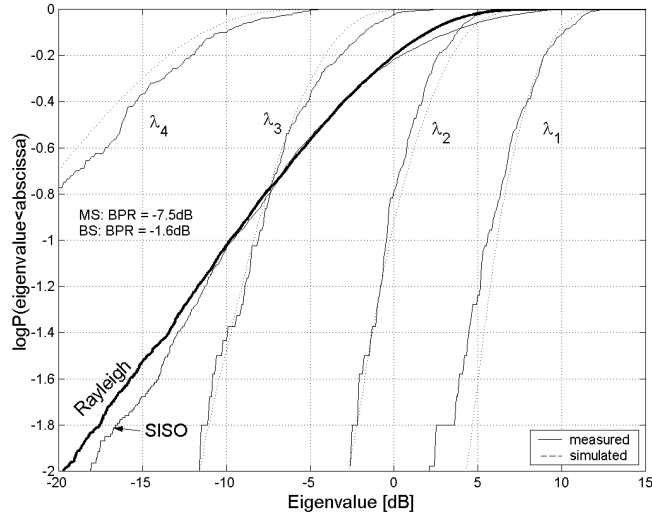

Figure 5.9: Local validation of the model for Example 1 in the polarization domain. The cdfs of the 4 eigenvalues are presented for simulated and measured data. It can be seen that the set of simulated eigenvalues match the measured eigenvalues well.
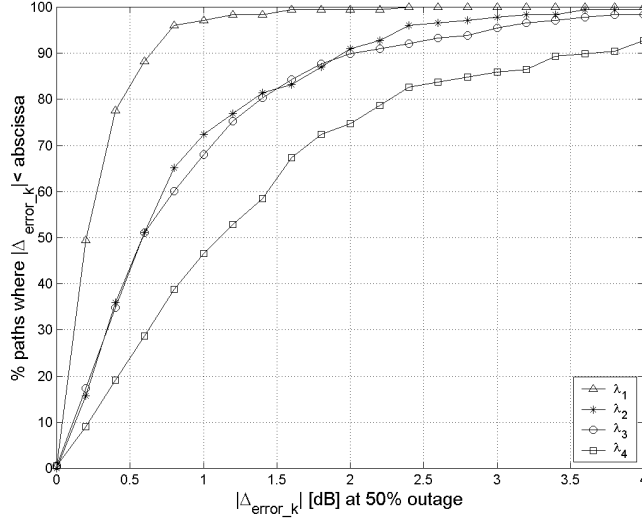
---

[4]see Appendix C

Figure 5.10: Global validation of the model in the polarization domain. The cdfs of $|\Delta_{error\_k}|$ when using $Array_1$ quantitatively present the ability of the model to reproduce realistic MIMO radio channel.

5.5   Summary and Interim Conclusion

A description of a WB stochastic MIMO radio channel model reported in [57] has been presented in its NB format along with its empirical validation.

This is a simple and computationally efficient model, well suited for link level simulations. The originality of this model is that it enables the simulation of partially correlated radio channels as it is to be expected from realistic wireless scenarios

The advantage of the model is that it relies on findings already published in the literature regarding propagation in SIMO systems. Consequently, a small set of parameters for characterising the communication scenario in the narrowband condition, the power Doppler spectrum (with their phases uniformly distributed over $[0, 2\pi]$ and independent from one another) and two correlation matrices describing the correlation properties at the two ends of the path, are necessary for the stochastic model.

The validation procedure of the MIMO model consisted on the comparisons between measured eigenvalues and simulated eigenvalues. The model validation was performed in both the spatial and polarization domains. Local (investigation of one path at a time) and global (investigation all the path treated at the same time) validation were considered. Their outcome indicates that the stochastic MIMO radio channel model renders the correlated propagation mechanisms appropriately for the spatial domain, and therefore has been validated in the NB condition. For the polarization domain,

two different methods of implementing the model were described depending on the nature of the propagation scattering. The scattering nature of the measured data limited the polarization investigation to only one method. This method used to model the polarization domain was positively validated.

It is believed that the NB validation of the model can be extended to WB condition with the uncorrelated scattering assumption in the delay domain, i.e., between the taps of the delay line channel model, as in [57].

Chapter 6

Performance Evaluation of the MIMO Radio Channel

In this chapter, the impact of the propagation properties of the radio channel on the parallel subchannelling concept is presented. Having understood the basic concept of MIMO, a number of factors which influence the number of eigenvalues and thereby the optimisation of the MIMO technology can be listed below

☞ Number of elements in the MEA configuration

☞ Correlation properties of the MIMO radio channel

☞ BPR between the MEA ports

The conclusions and recommendations are supported by capacity results, based on measured and simulated data, to emphasize the consequences of these parameters on MIMO system performance. The estimation of the spectral efficiency is based on the calculation of the Shannon capacity formula (see Chapter 2). This study is limited to a single-user scenario where two power allocation strategies are compared; water-filling and uniform power allocation.

Recall that the capacity results presented here are theoretical values for error-free transmission in the presence of background noise and provide an idea of the MIMO performance. To reach these values, in real life, coding (e.g. turbo coding) detection, constellation size among others should be considered in the system implementation. For an isolated MIMO system, i.e., single user scenario, the results presented here are a theoretical upper limit to the achievable data rate.

6.1 Impact of the Radio Channel on the MIMO Performance

This section presents the impact of the correlation properties of the radio channel on the parallel subchannels offered by the MIMO concept. This is addressed for the spatial, polarization and joint spatial-polarization domains. These results are based from the measured radio channel data.

Mainly two paths were identified for their propagation properties and used in the analyses of this section unless otherwise mentioned. The measured data are extracted from the indoor-to-outdoor microcell of the SUNBEAM project measurement campaign. They have been introduced in Chapter 4 on page 73 for their two distinctive ASs and reminded below:

☞ Example 3 : AS of about 3°; as a result, the correlation coefficients between elements of same polarization are very high ($\rho \geq 0.9$). This is a partially correlated scenario with a Rice distribution (*K-factor* = 3).

☞ Example 4 : AS of approximately 20°; as a result, the correlation coefficient values are low ($\rho \leq 0.5$). This is a partially decorrelated scenario.

Recall that in both cases, the correlation coefficient at the MS is very low ($\rho \leq 0.3$) since the scattering in the indoor environment is rich enough so that only a small element separation of the order of 0.5λ is required to decorrelate signals.
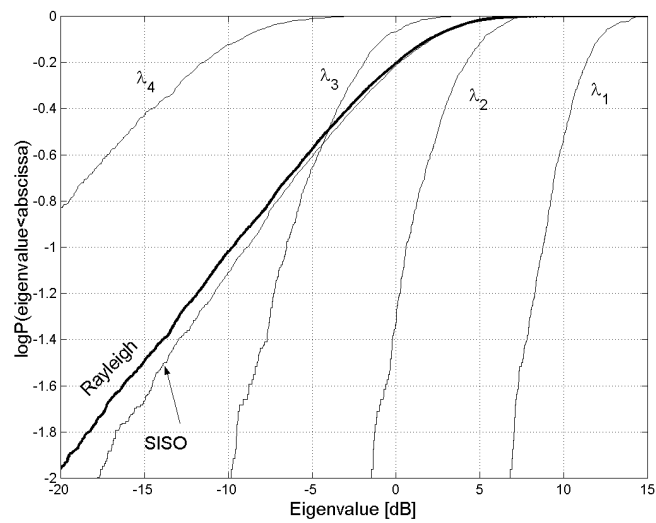
6.1.1 Spatial Domain

The results illustrate very well the influence of the radio channel in the spatial domain on the concept of parallel subchannelling (Figure 6.1) and its consequences for the capacity (Figure 6.2).

The eigenvalue analysis of the measurement data is performed on a 4×4 MEA configuration; results of the eigenanalysis are presented in Figure 6.1. The MS consists of four vertical polarized elements with 0.5λ separation and the BS consists of the same number of element with 0.45λ separation. The cdfs are computed over the full run of the Tx mast, 20λ in this case.

Figure 6.1 (i) illustrates the partially correlated scenario only. The high gain of the MEA at the BS due to the low AS results in one strong eigenvalue, λ_1, while the second strong eigenvalue λ_2 is 25 dB lower than λ_1. For the partially decorrelated scenario, illustrated in Figure 6.1 (ii), λ_2 and λ_3 become more significant. The cdf of the measured eigenvalues in the partially decorrelated scenario is in relatively good agreement with the theoretical study presented in [17] where fully decorrelated i.i.d. radio links were assumed.
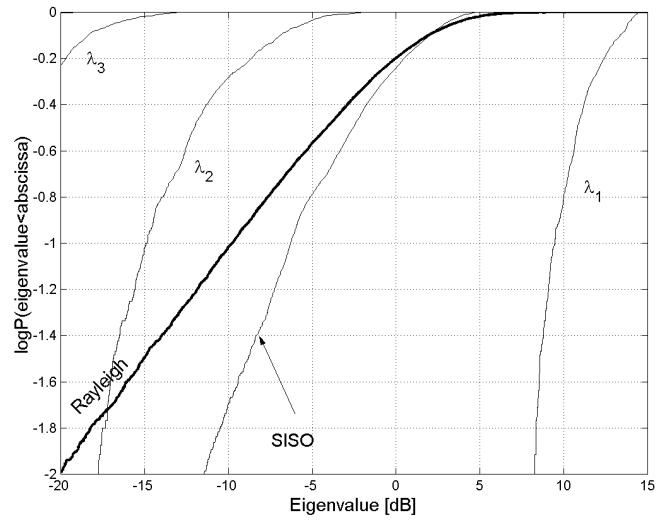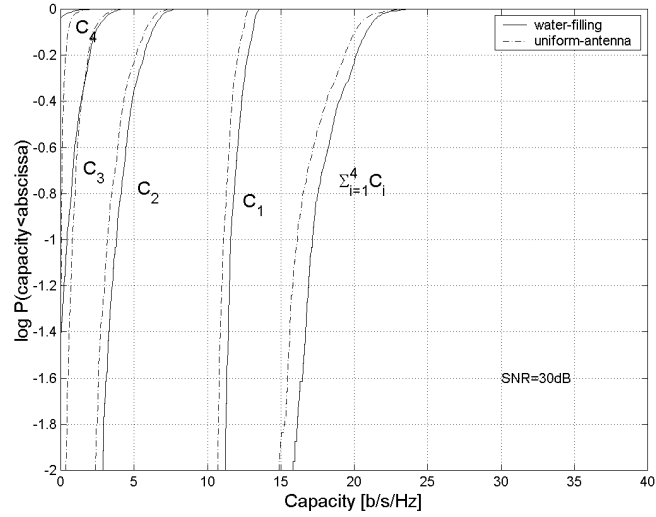
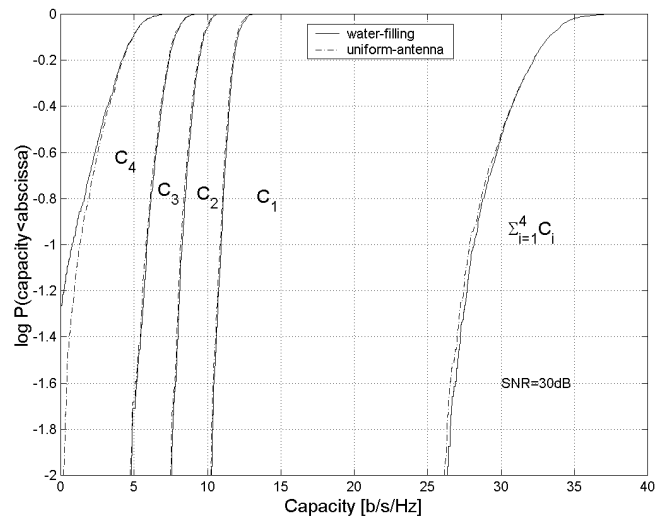(i) Example 3, partially correlated scenario in the spatial domain, AS $\simeq 3°$ at the BS.

(ii) Example 4, partially decorrelated scenario in the spatial domain, AS $\simeq 20°$ at the BS.

Figure 6.1: Cdfs for the eigenvalues for two distinct radio channel properties within the same microcell environment.

(i) Capacity results for Example 3.

(ii) Capacity results for Example 4.

Figure 6.2: Empirical example of the mapping between the eigenvalue and the capacity within the same microcell environment (SNR=30 dB).

The difference in the number of parallel subchannels within the same microcell emphasizes the need for a more robust MIMO technique to counteract the environmental fluctuations. This may be achieved either by increasing the spacing between the elements of the MEA or by using polarization diversity as shown later in this chapter.

Figure 6.2 illustrates the impact of each subchannel, identified in Figure 6.1, upon the total capacity available, assuming a mean SNR per Rx element of 30 dB. The total capacity $\sum C_i$ at the 10% level, for the correlated case in Figure 6.2 (i), is 17 b/s/Hz due to the fact that only two channels, identified by λ_1 and λ_2, are contributing. When the MIMO radio channel is decorrelated, i.e., the contribution of λ_1, λ_2 and λ_3 is significant, a tremendous total capacity of 27.9 b/s/Hz is achievable.

The comparison between the two power allocation strategies on the total capacity indicates that the difference is very small when the elements of the MEA are sufficiently decorrelated. However, it must be emphasized that the water filling strategy always provide a higher capacity than the uniform strategy, which is in good agreement with results reported in [61].

6.1.2 Impact of the MEA Topology

A convenient comparison of the performance of different MIMO systems is the total spectral efficiency of different MEA topologies. The spatial domain is only considered here and the two spatial environments presented above are investigated.

Tables 6.1 and 6.2 summarize the total capacity achievable for all the M×N configuration topologies possible ($M, N \leq 4$) based on measured channel data. The values are presented for a mean SNR per Rx element of 30 dB and at 10 % level.

Table 6.1 shows that in a partially correlated propagation scenario, when considering the correlation between the MEA elements at the BS, the capacity achieved by a 1×4 system is 11.1 b/s/Hz which is greater than for a 4×1 system (9.9 b/s/Hz). The difference between the two topologies is about 1 b/s/Hz, which is explained by the 3 dB difference in gain shown in Figure 2.5 on page 20 for the partially correlated scenario ($log_2(2) = 1$).

Table 6.2 also shows that since the channel is partially decorrelated, i.e., the correlation between the MEA elements at the BS and the MS are decorrelated, the number of elements at both ends of the link are interchangeable without significant changes in the capacity results i.e. a 1×4 system gives 10.9 b/s/Hz $\simeq$ 10.3 b/s/Hz achieved by a 4×1 system.

When the MIMO MEAs configuration is symmetrical, i.e., $M = N$, the difference between the water filling and the uniform power allocation is marginal in the considered scenario. However, in the case when the MEA configuration is asymmetrical, i.e., $M \neq N$, the total capacity considering the uniform power allocation is different with respect to the MEAs set-up so that $C_{M \times N} \neq C_{N \times M}$ and subsequently, the difference

$M \times N$		Water filling				Uniform			
		M element (BS)				M element (BS)			
		1	2	3	4	1	2	3	4
N element (MS)	1	7.9	8.9	9.5	9.9	7.9	8.9	9.5	9.9
	2	9.7	11.1	12.2	13.6	8.7	10.8	12.1	13.5
	3	10.5	12.5	14.1	15.7	8.9	11.5	13.3	15.2
	4	11.1	13.6	15.4	17.2	9.1	11.9	13.9	16.1

Table 6.1: Capacity (b/s/Hz) comparison at 10% level for different MEA topologies with a mean SNR per Rx element of 30 dB. Example 3, Partially correlated scenario, AS $\simeq$ 3° at the BS.

$M \times N$		Water filling				Uniform			
		M element (BS)				M element (BS)			
		1	2	3	4	1	2	3	4
N element (MS)	1	6.7	8.5	9.5	10.3	6.7	8.5	9.5	10.3
	2	8.9	13.7	16.6	18.4	8.0	13.7	16.6	18.4
	3	10.1	16.8	20.8	24.4	8.5	15.7	20.7	24.4
	4	10.9	18.3	23.9	28.2	8.9	16.3	22.7	27.9

Table 6.2: Capacity (b/s/Hz) comparison at 10% level for different MEA topologies with a mean SNR per Rx element of 30 dB. Example 4, Partially decorrelated scenario, AS $\simeq$ 20° at the BS.

with the water filling become more significant depending on the selected MEAs set-up. In the case where there are more MEA elements at the Rx than the Tx, i.e., $N \leq M$, the uniform power allocation does not waste any power since the potential number of subchannels is equal to the number of Tx MEA elements. However in the case where $N \geq M$, i.e., more Tx elements than at the Rx, the potential number of achievable subchannel is the same and the Tx power is wasted, consequently $C_{N \geq M} \leq C_{N \leq M}$. When $N \geq M$ the difference between the water-filling and the uniform power allocation is significant. In the rest of the thesis the optimum power allocation, i.e. the water filling scheme, is used to present total capacity results since they are not affected when $M \neq N$.
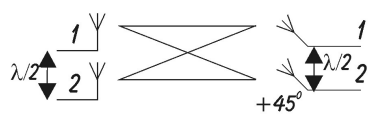
6.1.3 Polarization Domain

To remedy the weakness of the spatial diversity technique with regards to the variation of the propagation properties of the radio channel in the spatial domain, two methods can be used. The first method is to increase the spatial separation between the elements and therefore consider a larger MEA somewhat cumbersome. The second method is the use of polarisation diversity which is considered in this section.

The results presented here consider the same radio channel as described earlier in Example 3 and Example 4. a partially correlated (AS $\simeq$ 3° at the BS) and a partially decorrelated (AS $\simeq$ 20° at the BS) scenario respectively.

Two 2×2 MIMO MEA topologies are compared. They differ at the BS: one system uses spatial diversity and the second system employs polarization diversity only, i.e., dual polarized colocated elements with no spatial separation. The ±45° set-up is considered here so that the scenarios exhibit an equal BPR. Note that the polarization loss vector due the tilting of ±45° is not compensated in the rest of the analysis.

☞ 2×2 spatial: The MS consists of two vertical polarized elements with a spacing of 0.5λ and the BS consists of two +45° elements with a spacing of 0.5λ. An illustration of the MIMO setup is given below along with the mean power correlation coefficient matrix at both the BS and MS.
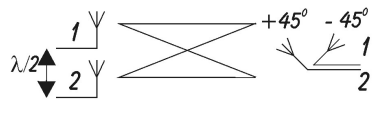
$$\mathbf{R}_{BS}^{pow} = \begin{bmatrix} 1 & 0.96 \\ 0.96 & 1 \end{bmatrix} \qquad \mathbf{R}_{BS}^{pow} = \begin{bmatrix} 1 & 0.59 \\ 0.59 & 1 \end{bmatrix}$$

$$\mathbf{R}_{MS}^{pow} = \begin{bmatrix} 1 & 0.11 \\ 0.11 & 1 \end{bmatrix} \qquad \mathbf{R}_{MS}^{pow} = \begin{bmatrix} 1 & 0.09 \\ 0.09 & 1 \end{bmatrix}$$

Example 3   Example 4

☞ 2×2 pol: The MS consists of two vertical polarized elements with a spacing of 0.5λ and the BS consists of two dual polarized ±45° colocated elements, i.e., with no spacing. An illustration of the MIMO setup is given below along with the mean power correlation coefficient matrix at both the BS and MS.


$$\mathbf{R}_{BS}^{pow} = \begin{bmatrix} 1 & 0.45 \\ 0.45 & 1 \end{bmatrix} \qquad \mathbf{R}_{BS}^{pow} = \begin{bmatrix} 1 & 0.02 \\ 0.02 & 1 \end{bmatrix}$$

$$\mathbf{R}_{MS}^{pow} = \begin{bmatrix} 1 & 0.08 \\ 0.08 & 1 \end{bmatrix} \qquad \mathbf{R}_{MS}^{pow} = \begin{bmatrix} 1 & 0.22 \\ 0.22 & 1 \end{bmatrix}$$
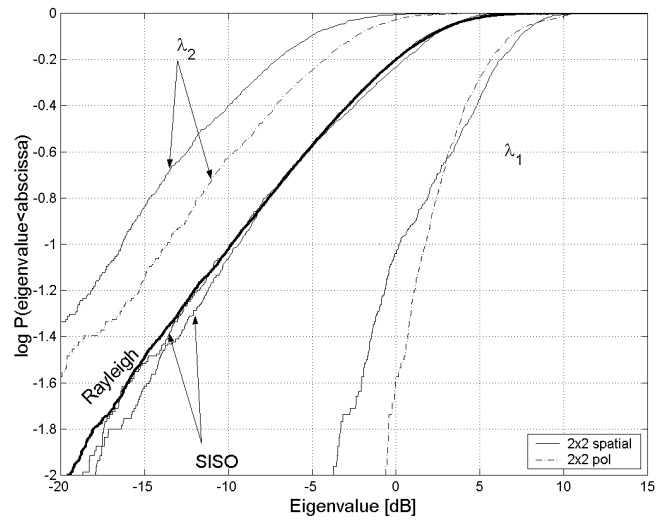
Example 3   Example 4

Figure 6.3 (i) presents the radio channel classified as partially correlated in the spatial domain for the two MEA set-ups. The power gain of the second subchannel, λ_2, is improved when polarization diversity is employed. This was to be expected since the correlation coefficient showed lower correlation when polarization diversity was employed than using spatial diversity.

Therefore polarization diversity can be used as a remedy to make MIMO systems more robust with respect to the radio channel. However the use of polarization diversity on its own limits the number of MEAs elements. Combining polarization diversity with spatial diversity could be performed to increase the number of elements and subsequently increase the MIMO technology performance. This is addressed in the next section.
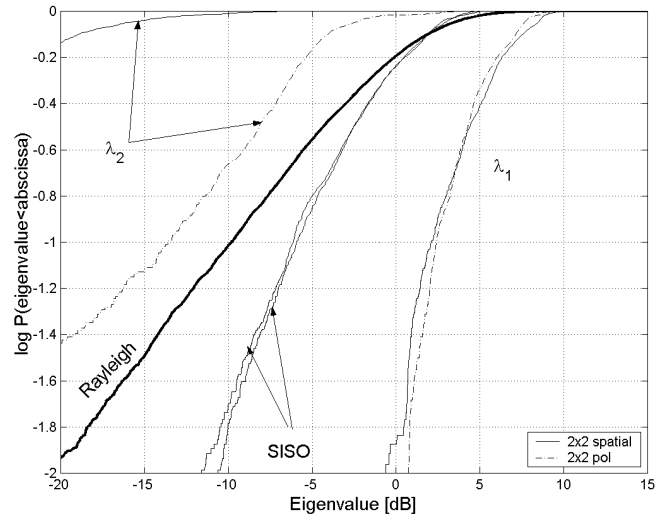
(i) Example 3, partially correlated scenario in the spatial domain, but partially decorrelated in the polarization domain.

(ii) Example 4, partially decorrelated scenario in the spatial and polarization domain.

Figure 6.3: Comparison of the spatial and the polarization diversity technique using 2×2 MIMO MEA configuration for two distinct radio channel spatial correlation classes.

6.1.4 Joint Spatial-Polarisation Domain

In this section, two advantages of using the joint spatial-polarisation domain in MIMO technology are addressed: robustness and compactness.

Recall that the joint spatial-polarization correlation coefficient is the product of the polarization and the spatial correlation coefficients as it was shown earlier in a microcell environment. Therefore, it is unlikely that both diversity techniques fail simultaneously.

6.1.4.1 Robustness Advantage

To provide a quantitative order of performance when applying joint spatial-polarization diversity to the MIMO concept, capacity results based on measured data are presented hereafter which illustrate the impact of such diversity techniques. The MEA elements at the BS are all polarized to $+45°$. This orientation is due to physical measurement limitation). A comparison between the following MEAs topology is performed.

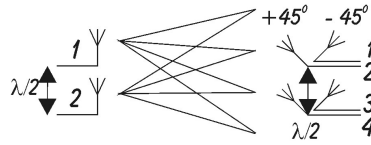☞ 1×1 spatial: The MS consists of a vertical polarized element and the BS consists of one $+45°$ element.
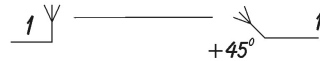
☞ 2×4 spatial: The MS consists of two vertical polarized elements with a spacing of 0.5λ and spatial diversity is only introduced at the BS with also a spacing of 0.5λ between the 4 elements.
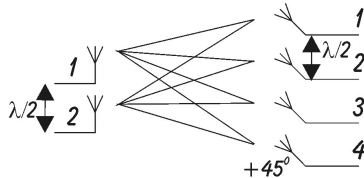
☞ 2×4 spatial+pol: The MS consists of two vertical polarized elements with a spacing of 0.5λ and combines two $\pm45°$ elements with spatial diversity, i.e. 0.5λ, between the two pairs.

☞ 4×4 spatial: The MS consists of four vertical polarized elements with a spacing of 0.5λ and spatial diversity is only introduced at the BS with also a spacing of 0.5λ between the 4 elements.
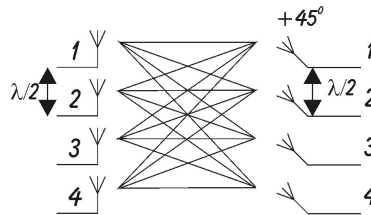

The analysis considers the same microcell environments as earlier, Example 3 and Example 4, the partially correlated and decorrelated propagation scenarios in the spatial domain investigated during the SUNBEAM measurement campaign respectively. The total capacity achievable with such a set of MIMO topology is presented in Figure 6.4 (i) for the partially decorrelated scenario and Figure 6.4 (ii) for the partially correlated propagation scenario in the spatial domain.

It is believed that a 2×4 set-up is a reasonable configuration for a practical implementation of the MIMO technology for a UMTS system, i.e., two elements can be fitted at the handset and four elements at the BS and therefore the analysis is focused on these 2×4 systems.

For the partially decorrelated situation in Example 4, the combined 2×4 spatial-polarization diversity system provides a higher total capacity than the 2×4 spatial diversity system. Using the polarization diversity, the correlation at the BS is low and as a consequence, two effective parallel channels are created, which are similar in performance to the 4×4 spatial diversity system. The capacity gain achieved by the 2×4 and 4×4 spatial set-up compared to the 1×1 system is the result of a Tx diversity gain since the elements of the MEA indoors are partially decorrelated. The parallel subchannelling is not exploited.

However, in Figure 6.4 (ii) the propagation channel is already partially decorrelated in the spatial domain, therefore the added decorrelation due to the polarization diversity is not significant. This results in the same total capacity, with or without polarization diversity for the 2×4 MEA set-up. Here, the 4×4 system takes advantage of the four parallel subchannels hence a large achieved capacity.
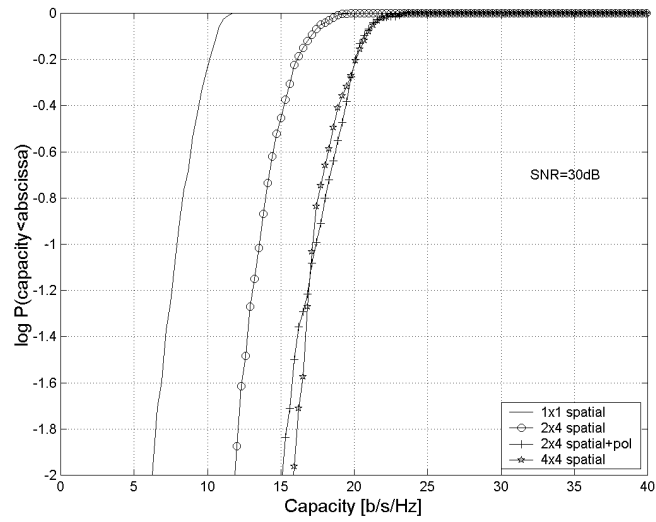
(i) Example 3, partially correlated in the spatial domain.
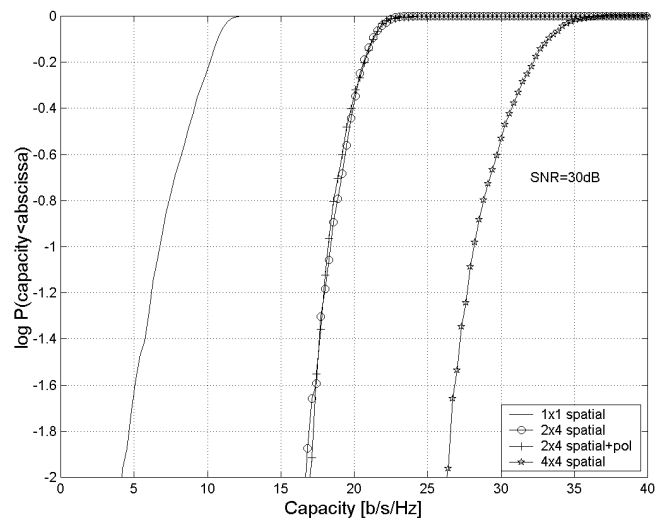
(ii) Example 4, partially decorrelated in the spatial domain.

Figure 6.4: Capacity comparison for different MEA set-ups.

Once again, it confirms the fact that the use of the joint spatial-polarization diversity is an attractive solution to achieve high decorrelation between the MEA elements when the radio channel is partially correlated in the spatial domain, and subsequently provides a more robust system in terms of spectral efficiency for microcell environments.

6.1.4.2 Compactness Advantage

!

For indoor picocell environments, large number of element MEAs are likely to be implemented for WLAN application so high bit rate data transfer can be performed. Physical size becomes an issue if only spatial diversity is considered. The use of colocated dual polarised MEA can provide low correlation for a reasonable MEA physical size when large number of element is considered.

In this section, the analysis focuses on picocell scenarios. The investigation is based upon measured data collected during the METRA project. One path is considered here with two 4×4 MIMO systems since the measured data obtained in such a environment indicated equal BPR at both the MS and the BS. This path has been introduced in Chapter 5 on page 81 and reminded below:

☞ Example 5 : partially decorrelated scenario in the spatial domain from the nokia environment, where the patch MEA are ±45° orientated.

The two MIMO systems differ in the type of MEA configuration used at the BS as presented in the following.

☞ 4×4 spatial: The MS consists of four vertical polarized element with a spacing of 0.4λ and the BS consists also of four vertical polarized element but with a spacing of 1.5λ.
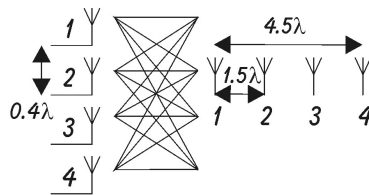
☞ 4×4 spatial+pol: The MS consists of four vertical polarized element and the BS consists of two dual dual polarised ±45° patch MEAs with 3λ separation.
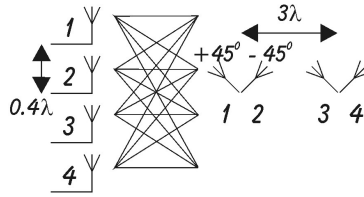
Figure 6.5 illustrates the performances of the first 4×4 spatial MIMO system. The MIMO system uses full advantage of the spatial propagation channel since it is shown in Chapter 4 that for picocell environments the spatial separation employed during the measurement was relatively low. Four eigenvalues can be identified, 2 of them being significant (P>0 dB at 10% level).

When considering the second MIMO system employing joint spatial-polarization diversity in Figure 6.6, the results are similar. Recall that the graphs present the normalized eigenvalue therefore the two graphs can be compared.

Using four dipoles or two dual polarised patch MEAs at the BS provides the equivalent results in terms of subchannel gain in the measured MIMO radio channel. This also emphasizes that using joint spatial-polarisation diversities permits the use of more compact MEA set-ups when a large number of elements is to be deployed.
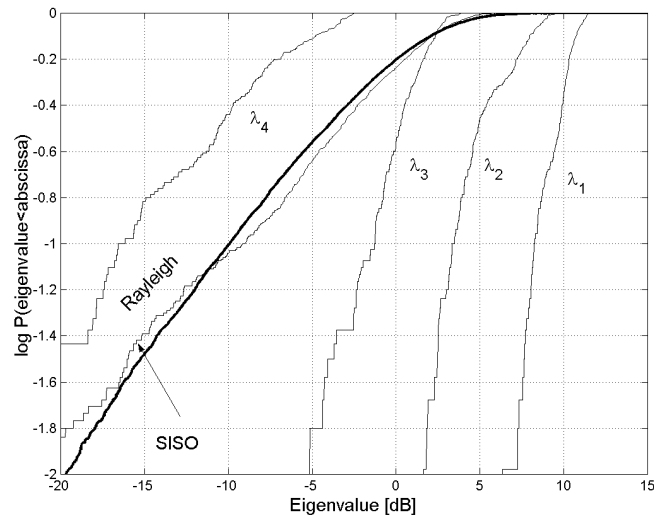

Figure 6.5: MIMO Eigenvalue distributions result for 4 dipoles at the MS and 4 dipoles at the BS for Example 5.
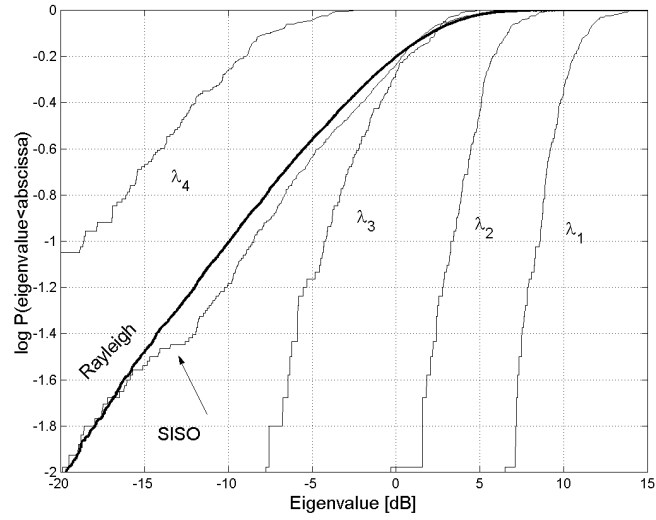
Figure 6.6: *MIMO Eigenvalue distributions result for 4 dipoles at the MS and 2 dual polarised* $\pm 45°$
patches for Example 5. Very similar behaviour to Figure 6.5 for the dipole configuration.
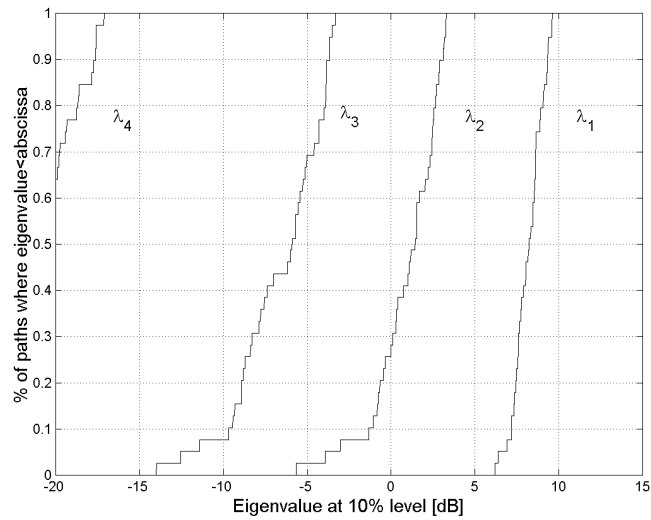

Figure 6.7: *Power gain of the parallel subchannels for 4(dipoles)×2($\pm 45°$ patch) MIMO configura-*
tion. The power gain is extracted from the 10% outage level of the eigenvalue (Figure 6.6) for each
measurement paths in Novi2, Novi3 and Nokia where the $\pm 45°$ *patch orientation is employed.*

The above results were presented for a single path. In order to have a global overview of the performance of the MIMO system when employing joint spatial-polarization diversity, an analysis has been performed over all the measurement positions of the picocell environments Novi2, Novi3 and Nokia. The reason for selecting these three picocell environments is that the patch elements at the BS had the same orientation, i.e., $\pm 45°$, in all three and as a result, the branches had equal BPR.

The power gain of each subchannel was extracted for each measurement path (see Figure 6.6) at 10% level and cumulated so that the cdf was computed. The empirical cdf of the power gain of each subchannel is presented in Figure 6.7.

The first two subchannels offer little variance in the power gain for the various measurement paths for the three investigated picocells. For the weaker eigenvalues, the slope is less steep. However, they have practically no significant impact on the MIMO performance. This indicates that for a picocell environment, with a BS employing $\pm 45°$ patch MEA, almost identical power gain is to be expected for the joint spatial-polarization technique for all the measurement paths.

6.2 Branch Power Ratio: A Practical Issue

In this thesis, the correlation coefficient behavior has been analysed to investigate the performance of a MIMO system assuming an equal BPR as defined in Section 2.8.

This section addresses the scenario where the BPR is unequal, which is a real implementation issue when using dual polarised MEAs. The investigation is based upon measured data collected during the METRA project and considers two distinct picocell environments where the dual polarized patch MEAs at the BS are set differently, $\pm 45°$ and $90°/0°$, therefore exhibiting different BPRs. They have been introduced in Chapter 5 on page 74 and reminded below:

☞ $\boxed{\text{Example 5}}$: partially decorrelated scenario in the spatial domain from the nokia environment, where the patch MEA are $\pm 45°$ orientated.

☞ $\boxed{\text{Example 6}}$: partially decorrelated scenario in the spatial domain from the airport environment,where the patch MEA are $90°/0°$ orientated.

Table 6.3 summarises the element configurations with their associated BPR and power correlation coefficients for one measured path of each of the two picocell environments. The value of $|\rho_{S_\Delta}|$, $|\rho_P|$, $|\rho_{S_\Delta \& P}|$ and the BPR for the two examples are averaged over the 8 possible elements of the MS. The correlation values are very low in both scenarios, whereas the BPR is very different.

Note that in practice with the same environment, tilting the antenna would affect not $\boxed{!}$ only the BPR but also the correlation coefficient [93]. Therefore, the two examples
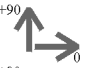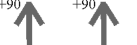
Path	Environment	MEA set-up at the BS		BPR[dB]	$|\rho|$
		P		0.9	0.22
Example 5	Nokia	$S_\Delta \& P$		1.4	0.23
		S_Δ		0.7	0.22
		P		-8	0.16
Example 6	Airport	$S_\Delta \& P$		-8	0.12
		S_Δ		0.3	0.11

Table 6.3: Summary of the MEA configurations with their associated BPR and correlation coefficient for a 1×2 scenario where the element at the MS is vertically polarised.

are not meant for comparison, but rather for illustration of the impact of the BPR on two specific cases.

In this section, the analysis follows three steps. A first study case focuses on a SIMO configuration to understand the propagation mechanism involved when the BPR varies from low to high values. Next, a second study case is presented using a 2×2 MIMO configuration for the two extreme BPRs. Finally the capacity performance is investigated and the impact of the BPR is outlined.

6.2.1   SIMO Approach

Figure 6.8 presents the cdfs of the eigenvalue computed for a 1×2 MEA configuration for $\pm 45°$ and $90°/0°$ element patches orientation. A vertically polarised dipole at the MS and a dual polarised patch at the BS are considered. In order to increase the statistical significance, the cdfs were computed over all the 8 elements at the MS. The cdfs are normalized to the strongest 1×1 radio channel due to the imbalance in the average received power.

Figure 6.8 (i) presents the Example 5 where the patch MEA is set such that it exhibits a $\pm 45°$ polarisation. It illustrates that the power gain from using two elements spatially separated but with a low BPR, is the same whether the $+45°$ or the $-45°$ element is used. There is no gain added to the spatial diversity technique by using polarisation diversity since $|\rho_{S_\Delta}|$ is already low. Note the diversity gain compared to the SISO scenario. Here again, note also that for the $\pm 45°$ case, in reality the mean received power level would be 0 to 3 dB lower than for the $90°/0°$ case.
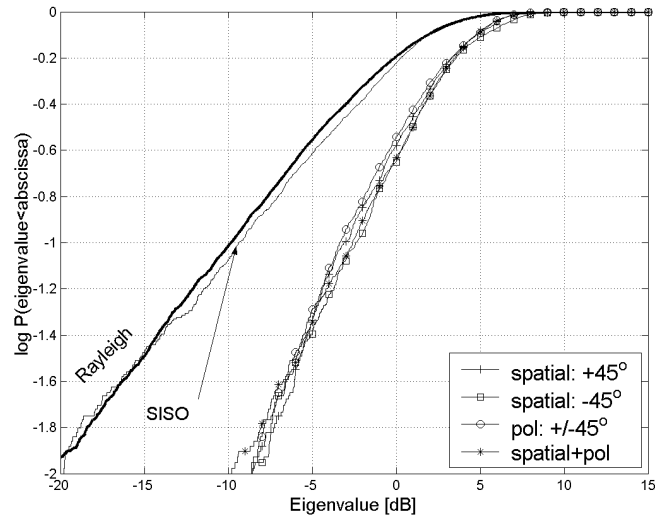
(i) Example 5: the nokia environment with the ±45° MEAs set-up.
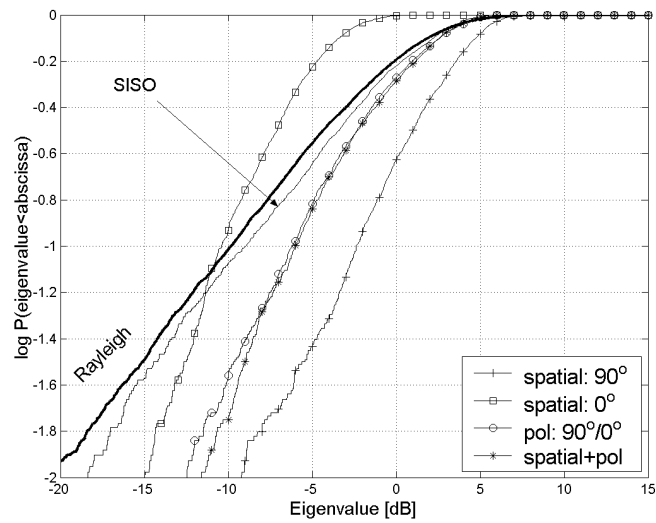
(ii) Example 6: the airport with the 90° and 0° MEAs set-up. Note the imbalance in the power gain compared to the above figure.

Figure 6.8: Illustration of the influence of the BPR on the power gain for a 1×2 SIMO configuration.
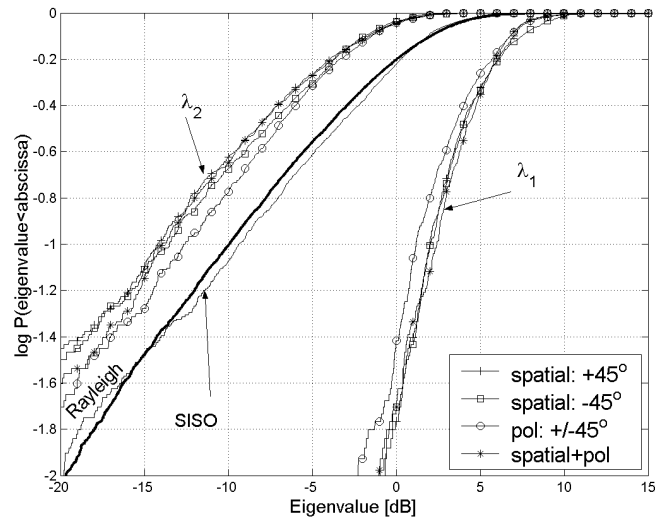
(i) Example 5: ±45°.
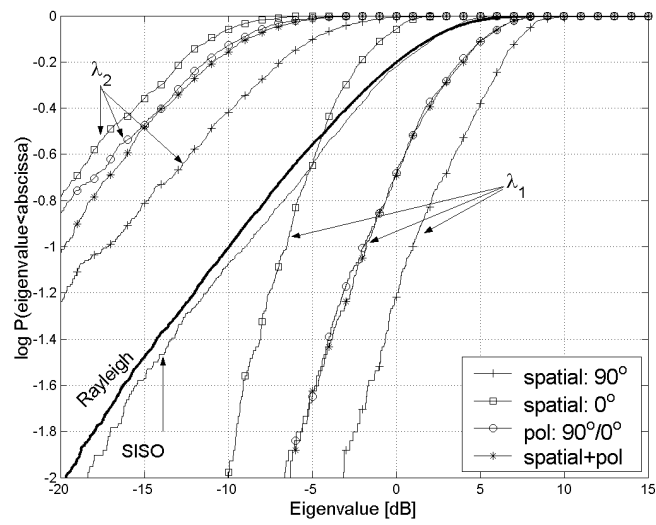
(ii) Example 6: 90° and 0°.

Figure 6.9: Illustration of the influence of the BPR on the eigenvalue for a 2×2 MIMO configuration.

In Figure 6.8 (ii), i.e., the Airport environment, the patch is rotated by 45° in the elevation plane such that a vertical (90°) and horizontal (0°) polarisation is achieved. It shows an imbalance in the available power gain depending on which branch is used. The 1×2 (0°) spatial set-up is 8 dB lower than the 1×2 (90°) spatial set-up. The polarization (90°/0°) and the spatial-polarization set-up have a higher gain compare to the 1×2 (0°) spatial MEA since the (90°) branch can still capture more energy than the (0°), but this gain remains negligible compared to the power gain of the 1×2 (90°) spatial set-up.

On the lowest power branch, i.e., 0°, a gain is noticeable due to the use of polarisation diversity but it remains negligible compared to the power gain of the 90° branch.

6.2.2 MIMO Approach

Figure 6.9 presents the MIMO extension of the previous SIMO analysis. The same picocell paths, MEA topology and eigenvalues normalization are used at the BS as in the example of Figure 6.8. Two vertical polarised elements are considered now at the MS.

Figure 6.9 (i), equal BPR scenario, shows that the two eigenvalues λ_1 and λ_2 exhibit a similar behavior whether using spatial diversity $+45°$, spatial diversity $-45°$, polarization diversity $\pm45°$, or joint spatial-polarization diversity.

Figure 6.9 (ii), BPR=-8 dB scenario, shows that the imbalance exhibited in the BPR drastically degrade the MIMO performance. λ_1 and λ_2 remain the same as in Figure 6.9 (i) when spatial diversity uses 90° since the transmitted signal is vertically polarised whereas when the $+0°$ branches are used, λ_1 and λ_2 drop down to -8 dB. The performance of the eigenvalues is also influenced by the BPR when considering the polarization and the joint spatial-polarization diversity even though $|\rho_P|$ and $|\rho_{S_\Delta \& P}|$ are very low.

6.2.3 Capacity Results

Figure 6.10 presents the total capacity computed from the measured data for the two situations for a mean SNR per Rx element of 30 dB. When an equal BPR is present, Figure 6.10 (i), a total capacity of 15 b/s/Hz is achieved at 10% level for all three diversity techniques. Figure 6.10 (ii) shows that with an unbalanced BPR, the capacity performance of the polarization and the joint spatial-polarization diversity drops to 12 b/s/Hz compare to the 14 b/s/Hz offered by the spatial diversity, although the power correlation values are very low. When spatial diversity is employed (using the 0° branches), a drop to 10 b/s/Hz is noticeable.
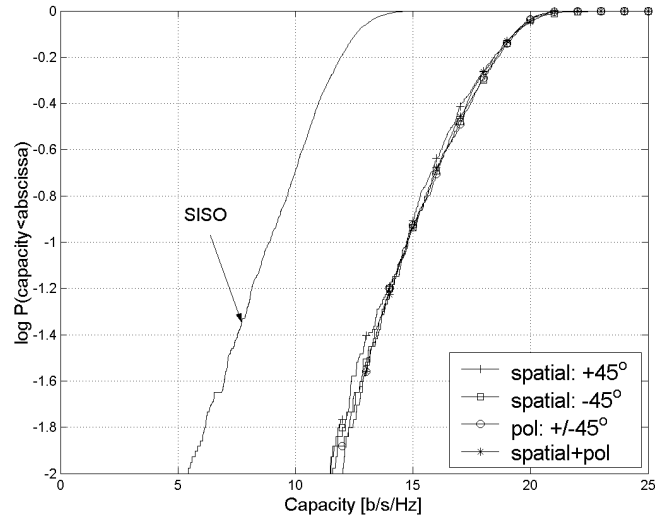
(i) Example 5: $\pm 45°$, equal BPR.
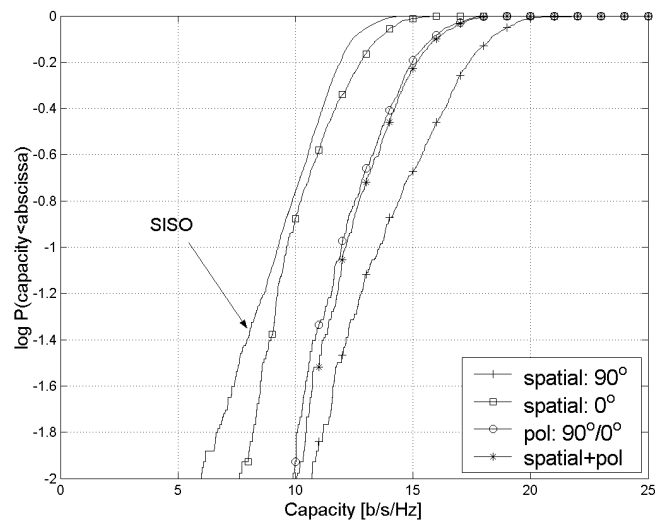
(ii) Example 6: $90°$ and $0°$. Note the impact of the unequal BPR.

Figure 6.10: Illustration of the influence of the BPR on the total capacity for a 2×2 MIMO configuration.

To conclude, although the correlation coefficient indicates strong decorrelation, no $\boxed{!}$ optimal MIMO configuration, in the robust sense, can be achieved when the BPR is unbalanced. Therefore when designing a MIMO system, it is recommended to deploy simultaneously equal BPR and low correlation coefficient MEA system.

6.3 Capacity Results for Microcell and Picocell

This section addresses the performance of the MIMO system in a more general perspective and the total theoretical capacity to be achieved by a MIMO system is presented for cell-specific situations for a single user scenario.

Making use of the model, Figure 6.11 illustrates the simulated total capacity at 10% outage level for different SNRs per Rx element when the water filling power allocation scheme is used. Two MEA set-ups, a 4×4 and a 2×4, are compared using spatial diversity only. The simulations are performed by extracting the input parameters from the measured data of the two paths introduced in Chapter 4 on page 73 and reminded below:

☞ $\boxed{\text{Example 1}}$: partially decorrelated scenario in the spatial domain selected from a picocell path.

☞ $\boxed{\text{Example 2}}$: partially correlated scenario in the spatial domain selected from a microcell path

The simulated capacity vs. SNR, on a logarithmic scale, increases in a linear manner, but its slope is proportional to the number of subchannels being taken into account in the summation of equation (2.21) on page 21 recalled below

$$C = \sum_{k=1}^{K} log_2(1 + \lambda_k \frac{P_k}{\sigma_n^2}) \ .$$

At low SNR, the contribution of the first subchannel, i.e., λ_1, is dominant. For higher SNRs, all the subchannels are present in equation (2.21) and consequently, the summation process takes over so that all four subchannels contribute to the total capacity. As a consequence, for a high SNR, the slope of the 4×4 MEA set-up capacity versus SNR is twice the slope of the capacity plot for the 2×4 MIMO set-up. Only 2 parallel subchannels are achieved in the second MEA set-up compared to the 4 parallel subchannels achieved by the 4×4 MIMO set-up. This means that when taking a SNR of 50 dB for instance, an increase in SNR of 3 dB provide 4 b/s/Hz for a 4×4, 2 b/s/Hz for a 2×2 and only 1 b/s/Hz for a conventional 1×1 wireless system.

Four conclusions can be drawn from these examples:

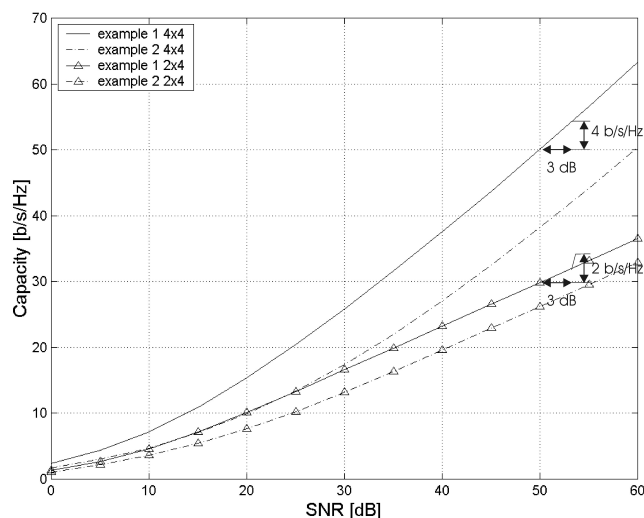☞ The total capacity increases with the SNR.

Figure 6.11: Simulated capacity (10% level) vs. SNR for Example 1 (Picocell - Partially decorrelated) and Example 2 (Microcell - Partially correlated). Use of the water filling power allocation strategy.

☞ The partially decorrelated situation provides more capacity than the partially correlated scenario at the same SNR and with the same MEA set-up.

☞ In the partially decorrelated scenario, the 4×4 MEA configuration takes full advantage of its additional available subchannels compared to the 2×4 set-up at high SNR.

☞ At low SNRs, MIMO systems only provide a combined Tx and Rx diversity and at high SNRs, the MIMO topology benefits from parallel subchannelling.

Figure 6.12 presents the cdf of the simulated capacity calculated with a mean SNR per Rx element of 30 dB and the input parameters extracted from all the 79 measured picocell paths. The simulated capacity results are robust for the picocell environments since the capacity results are less than 25 b/s/Hz and 27 b/s/Hz at the 10% and 90% percentage level respectively for a 4×4 MEA configuration, if water filling is used. This fluctuation of 2 b/s/Hz is explained by the fact that the elements of the MEAs at both the BS and the MS are sufficiently decorrelated for a sufficient amount of paths in picocell environments as previously demonstrated in this thesis. In the context of a MIMO scenario this is interesting since multiple parallel subchannels are available. It can therefore be concluded that even in situations where LOS is present in picocell environment, a MIMO topology using spatial diversity with small spacing is favorable. The difference between the two power allocation schemes is insignificant for a 2×4 MIMO set-up since the number of parallel subchannels is low. The difference becomes more significant as the number of potential parallel subchannels increases.
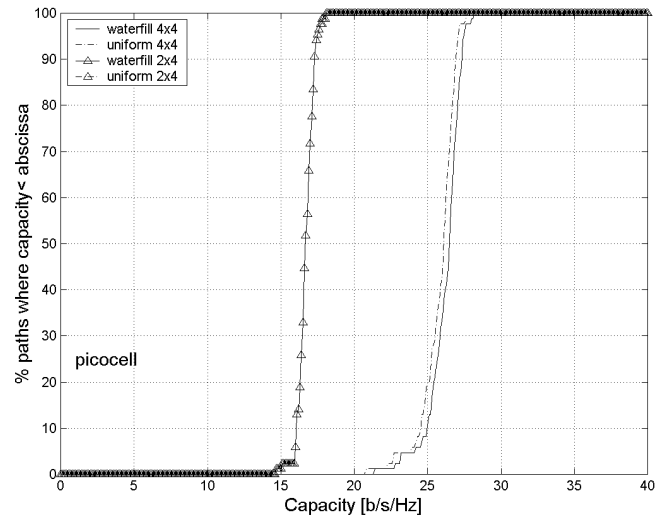
Figure 6.12: Cdf over the 79 picocell paths of the total capacity from capacity vs. SNR at SNR=30dB for 4×4 and 2×4 MEA configurations.
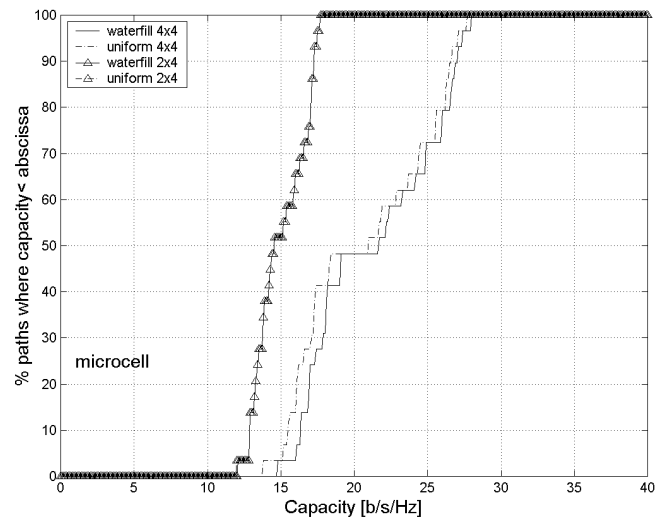

Figure 6.13: Cdf over the 28 microcell paths of the total capacity from capacity vs. SNR at SNR=30dB for 4×4 and 2×4 MEA configurations.

Figure 6.13 presents the cdf of the simulated capacity which input parameters are derived from the 28 measured microcell paths. The simulated capacity exhibits much larger variation than for picocell environment (Figure 6.12) from 16 b/s/Hz to 27 b/s/Hz at the 10% and 90% cdf level respectively. This is explained by the use of two different element spacings.The variation from 20 b/s/Hz to 27 b/s/Hz is attributed to the set-up using 1.5 λ while the low capacity contribution from 16 b/s/Hz to 20 b/s/Hz is obtained when applying only 0.5λ.

In microcell environments, the correlation, and subsequently the capacity, is strongly influenced by the nature of the surrounding scatterers and also by the element separation in the MEA. Scenarios with high correlation between MEA elements degrade the potential high bit rate of the MIMO set-up. Therefore, the use of spatial diversity technique, on its own, is not recommended for a MIMO topology when using 0.5λ element spacing at the BS. However, when 1.5λ is employed, microcell capacity results are similar to those measured in the picocell environments.

6.4   Summary and Interim Conclusion

In this chapter, the impact of the propagation properties of the radio channel on the parallel subchannelling concept has been presented emphasizing on the spectral efficiency achievable when using the MIMO technology.

The quality of the MIMO technology is dependent on the number of elements in the MEA employed, the correlation properties of the MIMO radio channel, and the BPR between the elements of the MEA system.

Two opposite propagation paths were selected as examples of a partially decorrelated and partially correlated paths. For the picocell environment, it was found that spatial diversity, with spatial separation as low as 0.4λ can provide low correlation and thereby high bit rate. However, this is not the case for the microcell environment. Simulated capacity results calculated with a mean SNR per Rx element of 30 dB indicates 25 b/s/Hz and 27 b/s/Hz at the 10% and 90% level respectively for a 4×4 MEA configuration, if water filling is used in the picocell environment. For the microcell environment, for the same percentage level 16 b/s/Hz to 27 b/s/Hz can be achieved when spatial diversity is used. Therefore polarization diversity can be used as a remedy to make MIMO systems more robust with respect to the radio channel. However the use of polarization diversity on its own limits the number of MEAs elements.

Combining polarization diversity with spatial diversity is recommended to design a robust and compact MIMO system with large number of element at the MEAs. This can only be achieved if equal BPR and low correlation coefficient are both present when designing a MIMO system.

Chapter 7

Conclusion

7.1   Summary

The performance of a new technology referred to as MIMO (Multi Input Multi Output), which involves a state-of-the-art combination of MEA (Multi Element Array) and digital signal processing, has been introduced to achieve higher spectral efficiency in wireless communication systems.

The potential benefits of using the MIMO technology lies in the creation of orthogonal information channels, the combination of Tx and Rx diversity, and an increase in the antenna gain. The performance of the MIMO technology is directly dependent on the MIMO propagation, the MEA, and the BPR (Branch Power Ratio); the MIMO technology would perform well in an uncorrelated scenario, i.e., a $M \times N$ MIMO topology offers $min(M, N)$ parallel subchannels at most, but would be less optimal for a correlated or pin-hole scenario. The eigenvalues are presented here as a quantitative approach to the parallel subchannelling; the capacity is directly connected to the eigenvalue through the Shannon capacity formula.

The main objective of this PhD is to provide measurement data which are bandwidth limited to the UMTS standard and also a characterisation of the radio MIMO propagation channel. Further, propagation parameters can be extracted from the measurement data and an empirical validation of a stochastic MIMO radio channel is possible. The target application of the correlation based MIMO model is link level simulation. This model originally assumes identical radiation pattern for each element of the MEA. Nevertheless, this constraint can be relaxed, under certain condition, so that any type of terminals can be considered. In addition, recommendations on how to use the MIMO technology are presented so that the MIMO technology achieves optimal performance.

7.2 Conclusions

One of the contributions of this thesis is the extensive MIMO measurement campaign presented in Chapter 3. Two measurement set-ups used for the ACTS SUNBEAM and IST METRA European projects were developed for the MIMO investigation of the radio channel. Suitable measured environments were identified to provide realistic propagation scenarios for picocellular and microcellular wireless system, where the MIMO technology is likely to be implemented. Spatial, polarization and hybrid spatial-polarization diversity set-ups can be extracted from the MIMO measurement data.

Another contribution of the thesis is the extraction of propagation parameters based on the measured data. This helps to understand the propagation radio channel and to further elaborate on the interpretation on the behavior of the MIMO technology. From the measured data, a large number of topics related to the extraction of propagation parameters are addressed in Chapter 4. The statistical distribution of the NB (narrowband) signal, *K-factor*, and the DoA (Directional of Arrival) analyses have been used together to categorise the environment investigated in terms of their LOS (Line-of-Sight)/NLOS(Non-Line-of-Sight) and low/high AS (Azimuth Spread) characteristics. Based on the information of the DoA using a square planar array, it can be concluded that the angular distribution of the waves in indoors does not necessarily follow a uniform distribution but more a clustered type. Hence, due to the identified clustering effect, it can be concluded that a meaningful PAS (Power Azimuth Spectrum) value can not easily be calculated. Furthermore, the DoA analysis can lead to the conclusion that on some measured paths the WSS requirement does not hold. Finally, a detailed analysis of the power correlation coefficient indicates that at the MS (Mobile Station) and the BS (Base Station), for picocell environments, elements separated by 0.4λ would provide low correlation ($\rho \leq 0.6$ for 90% of the measured paths). For microcell environments, the correlation coefficient at the MS is also low for this element separation, whereas, at the BS, large separation would be required to achieve a low correlation coefficient when spatial diversity is to be implemented. When polarization diversity is implemented, the orientation of the elements is of critical importance, since for a low correlation between elements, an unequal BPR may result in a drastic deterioration of the MIMO technology performance. It is also shown that the joint spatial-polarization diversity technique represents the optimum solution to obtain the lowest correlation value for picocell and microcell for compact MEA set-ups.

Another important contribution of the thesis, in Chapter 5, is the validation of a stochastic MIMO radio channel model developed and reported in [57]. The validation of this model was performed under the NB condition, however, it is believed that this validation can be extended to the WB (wideband) condition under the uncorrelated scattering assumption. This is a simple and computationally fast model, well suited for link level simulation. The originality in this model is the simulation of partially correlated radio channels as it is to be expected from realistic wireless scenarios. The advantage of the model is that it relies on findings already published

in the literature regarding SIMO radio channels. Consequently, a small set of parameters to fully characterise the communication scenario, namely the PDS (Power Delay Profile), the Doppler spectrum (with their phases uniformly distributed over $[0, 2\pi]$ and independent from one another) and two correlation matrices describing the correlation properties at both ends of the path, are necessary for the stochastic model. As of the writing of the thesis, the philosophy of the model has been accepted in the 3GPP standardisation. The outcome of the empirical validation indicates that the stochastic MIMO radio channel model renders the correlated propagation mechanisms appropriately in the spatial domain, and therefore has been validated in the NB condition. The measurement set-up, used to validate the MIMO model, only considered MEAs which were not under near-field's influences. Measurement scenarios of typical small terminals were not investigated in this study. For the polarization domain, two different methods of implementing the model were described depending on the nature of the propagation scattering. The scattering nature of the measured data limited the polarization investigation to only one method. This method used to model the polarization domain was positively validated.

A final contribution of the thesis is the performance evaluation of the MIMO technology presented in Chapter 6. The theoretical Shannon capacity results derived from measured and simulated data present the impact of the propagation properties of the radio channel on the performance of the MIMO technology. It was outlined that the quality of the MIMO technology is dependent on the elements in the MEA employed, the correlation properties of the MIMO radio channel, the BPR between the MEA elements and consequently the number of eigenvalues. Simulated capacity results at a mean SNR (Signal to Noise Ratio) per receive element of 30 dB indicate a high bit rate up to 25 b/s/Hz and 27 b/s/Hz at 10% and 90% of measurement paths respectively for a 4×4 MEA configuration, if water filling is used in picocell environments. For microcell environments, for the same percentage level a strong fluctuation of 16 b/s/Hz to 27 b/s/Hz can be achieved when spatial diversity is used. Therefore, combining polarization diversity with spatial diversity is recommended to design a robust and compact MIMO system. This can only be achieved if equal BPR and low correlation coefficient are present when designing a MIMO system.

It is important to emphasize that the MIMO technology works in two ways: the diversity MIMO and the information MIMO. At low SNRs, MIMO systems only provide a combined Tx and Rx diversity because only the strongest eigenvalue is excited and at high SNRs, the MIMO technology benefits fully from parallel subchannelling, i.e., all the eigenvalues are excited. Therefore, the MIMO technology is very well suited for adding diversity gain and increasing coverage, however at the expense of not providing a high bit rate for applications like for instance UMTS (limited space on the handset, typical low operating SNR). Note that multimode MEAs [143],[144] have brought interest and if the technology is there, this could solve the issue of the size requirement in a UMTS handset. When high peak data rate is considered, a combination of many decorrelated elements at both MEAs (with equal BPR) and large SNR is necessary. These conditions could be fulfilled in WLAN deployment scenarios. The coverage is

ensured with small cells with large operating SNRs, and the typical size of WLAN terminals, like laptops, make it possible to fit many elements in their frame. However, the indoor-to-indoor measurement campaign focused on UMTS frequency bandwidth and therefore did not address the frequency selectivity aspect of WLAN applications.

7.3   Further Work

The work presented in this thesis only focused on the radio propagation aspect of the MIMO technology and concentrated on a single user scenario. Also, one of the main assumptions for obtaining the high bit rate presented is based on the theoretical capacity formula of Shannon. Therefore, the natural evolution of this work would be to investigate the MIMO technology towards system implementation so that more realistic figures of bit rate values could be available where, for instance, the influence of a multi-user scenario, multi-cell scenario and directional interference would be considered.

Appendix A

Environments

This appendix presents the environment layouts which were investigated, with pictures taken during the measurement campaign.

Picocell

Figure A.1 illustrates the nokia environment. It emphasizes the open area office characteristic of this environment. Figure A.1 (ii) is a picture taken from far corner of Pos. 4 and provides a large view of the offices. The arrows represent the displacement of the slide at the MS. The circles numbered from 1 to 4 represent the dipole MEA and the half circles numbered from 5 to 8 represent the patch antenna and the arrows associated indicate the directivity of the patches.

Figure A.2 and Figure A.3 present the novi3 environment with two different locations of the BS, respectively. They both were on the first floor, while the MS was located alternatively on the ground or first floor. The picture in Figure A.2 (ii) was taken in the office at Pos. 4, the same office facing BS1, and the picture in Figure A.3 (ii) provides an overview of the large foyer with the *dragon* located at Pos. 8. Note, the RF trolley is next to the pillar.

Figure A.4 presents the fb7b2 building for the picocell configuration. The picture of Figure A.4 (ii) emphasizes the confine office space within this environment.

Figure A.5 and Figure A.6 present the airport layout and pictures from the open terminal area.

Microcell

Figure A.7 presents the frb7 building for the microcell configuration. This is the same indoor environment than for fb7b2, as shown in Figure A.4.

Figure A.8 presents the microcell novi2 experiment. Figure A.8 (i) indicates the different paths of the MS on the building plan with an arrow indicating the direction to the BS, 300 m away from the building. Each path is represented by a circled arrow to illustrate the rotation of the dipole used during the SUNBEAM project. Figure A.8 (ii) is a picture of the dual polarized antenna mounted on a mast.
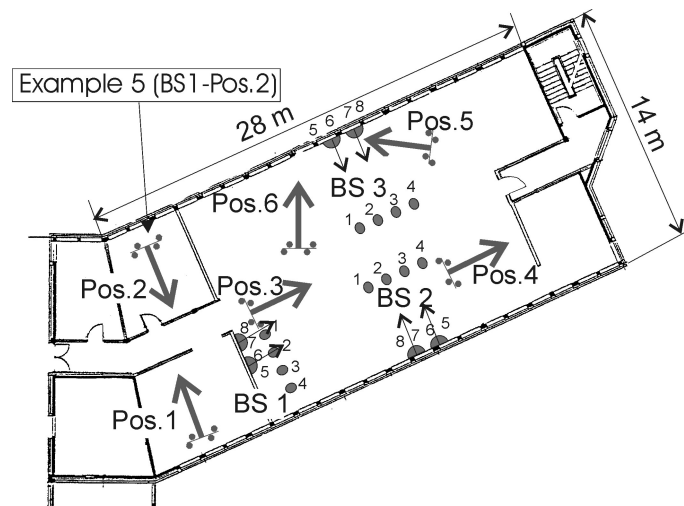
(i) Floor plan of the measured environment with the location of the MS and BS.

(ii) Picture of the environment from Pos.4.

Figure A.1: **nokia** *environment. Picocell. In total 18 measurement paths were investigated for this environment.*

(i) Floor plan of the measured environment with the location of the MS and BS on the first floor.

(ii) Picture of the environment of Pos.4.

Figure A.2: **novi3** environment. Picocell. In total 12 measurement paths were investigated for this environment with BS1 located on the second floor.

(i) Floor plan of the measured environment with the location of the MS on the ground floor and BS on the first floor.

(ii) Picture of the environment from Pos.2 (first floor) of Pos.8 (ground floor).

Figure A.3: **novi3** environment. Picocell. In total 12 measurement paths were investigated for this environment with BS2 located on the second floor.
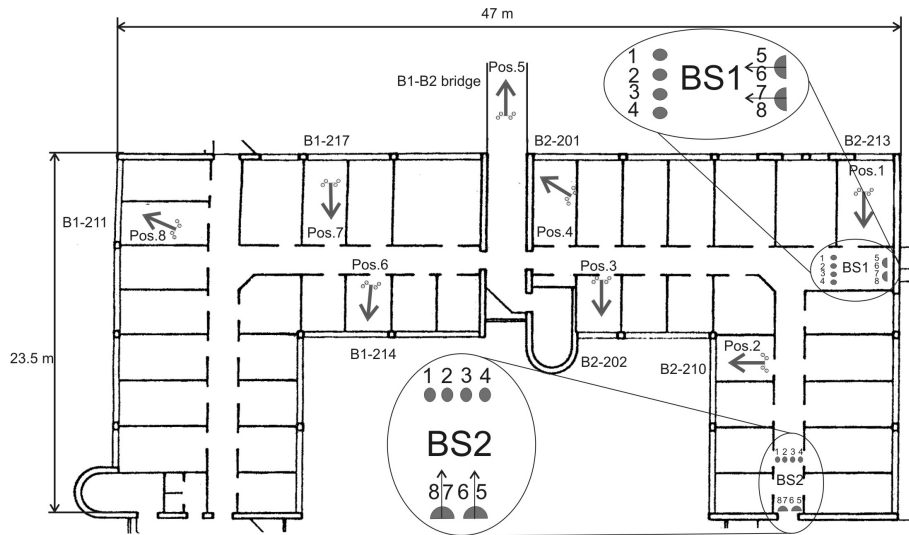
(i) Floor plan of the measured environment with the location of the MS and BS.

(ii) Picture of the environment of Pos.2.

Figure A.4: **fb7b2** environment. Picocell. In total 16 measurement paths were investigated for this environment.
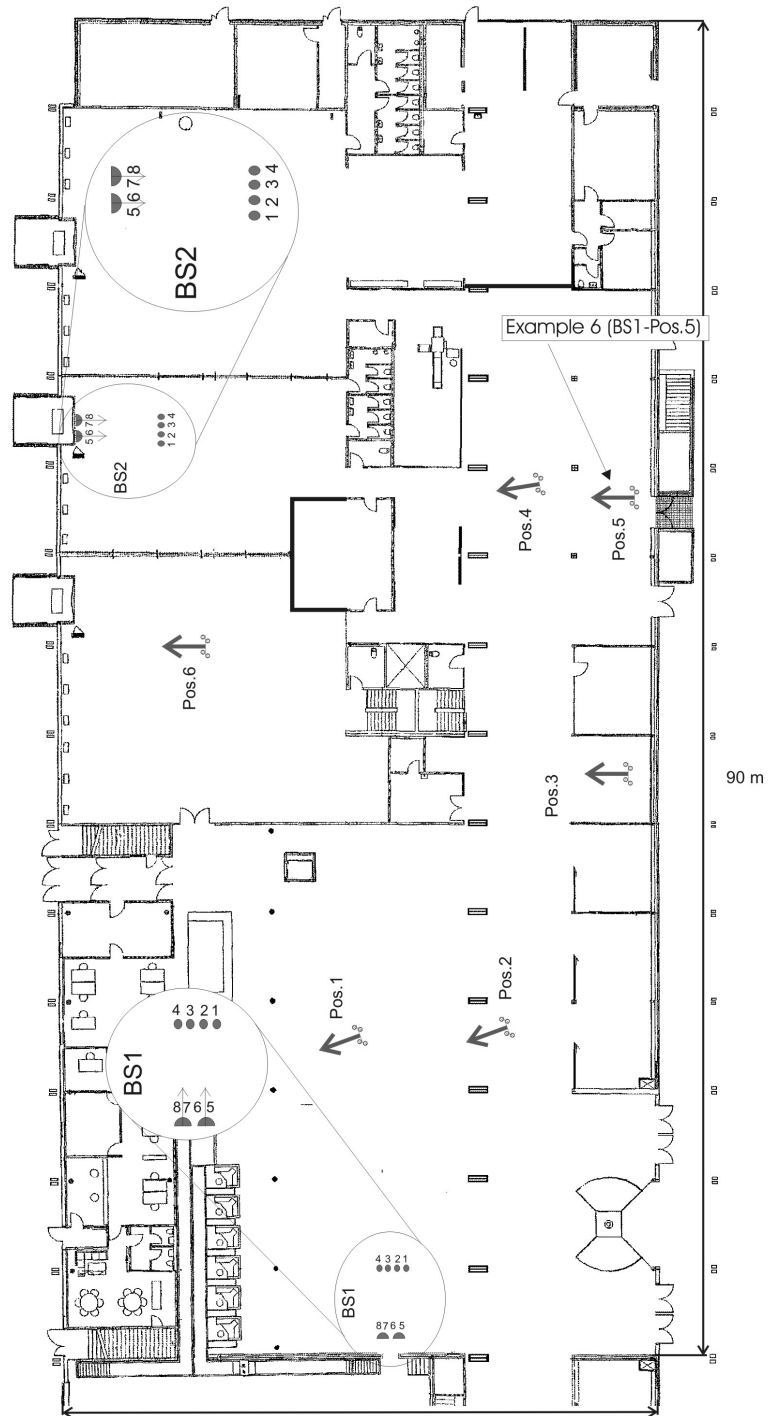
Figure A.5: **airport** environment. Picocell. Floor plan. In total 12 measurement paths were investigated for this environment. Two BS are represented on the same plan.

(i) Picture of the environment at Pos.6.

(ii) Picture of the environment at Pos.1 viewed from BS1.

Figure A.6: Pictures taken of the airport during the measurement campaign.
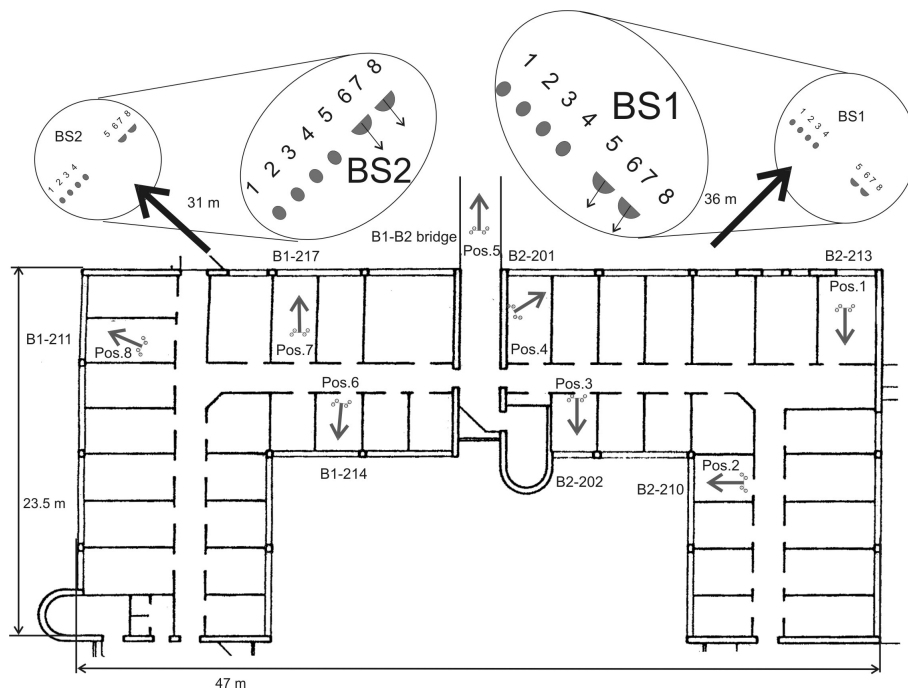
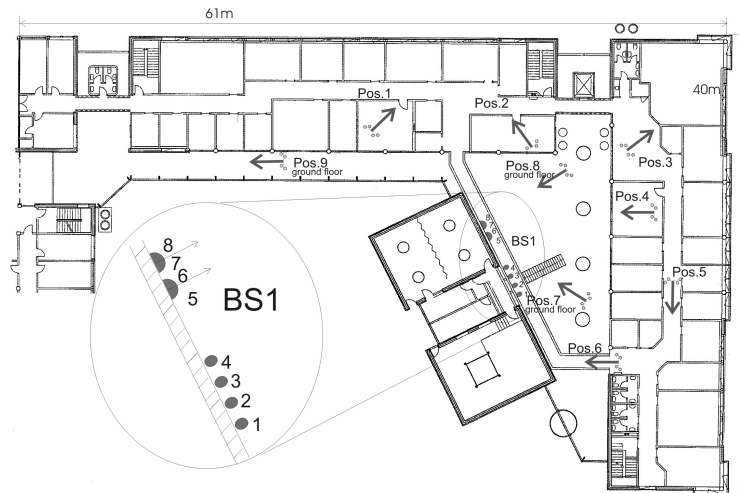(i) Floor plan of the measured environment with the location of the MS and BS.

(ii) Picture of the location Pos.3.

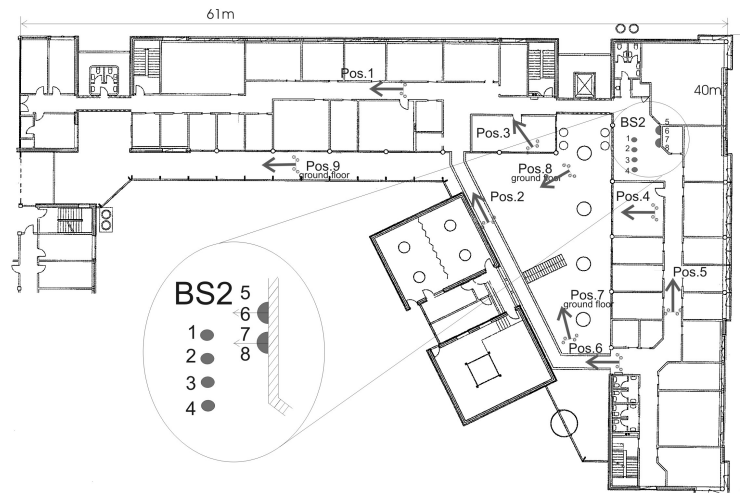Figure A.7: **frb7** environment. Microcell. In total 13 measurement paths were investigated for this environment.
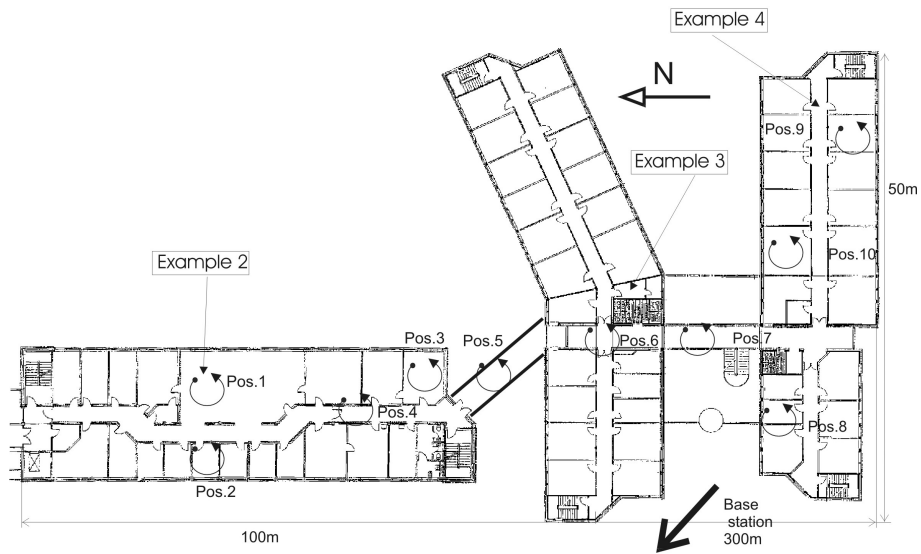
(i) Floor plan of the measured environment with the location of the MS and BS.
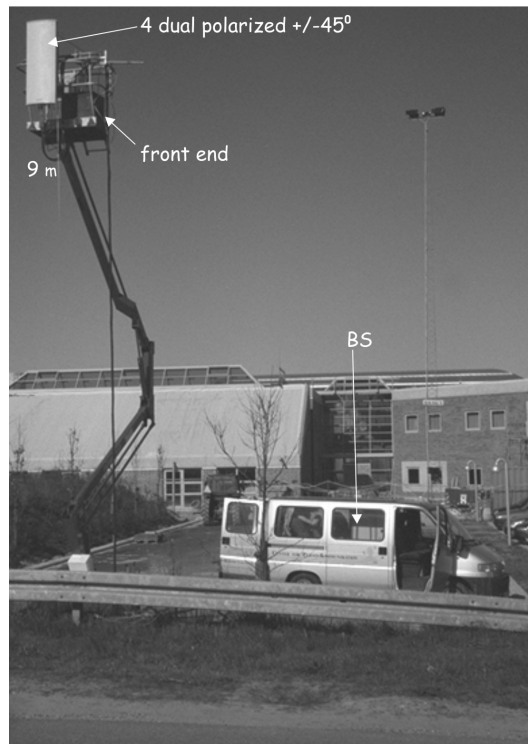
(ii) Dual polarized MEA mounted on a mast located on
a parking. The BS equipment is in the van.

Figure A.8: **novi2** environment. Microcell. 10 measurement paths out of a total of 15 are presented
in the floor plan.

Appendix B

Influence of the Compensated Radiation Pattern on the Correlation Coefficient

The interleaved MEA solution, described in Section 3.2.4 on page 33, provides an improvement in the shape of the radiation pattern when compared to the case of the original linear MEA. However, a question remains as to the influence of the new radiation pattern. It can be argued that the residual variation (within the region of 2 to 3 dB) of the radiation pattern observed in Figure 3.5(ii-b) can still influence the correlation coefficient. Therefore the conclusion whether the decorrelation observed on the measured data is mainly due to the spatial separation of the MEA elements or to a combination of both spatial and radiation pattern diversities is to be determined.

In order to investigate this, a model assuming scatterers uniformly distributed over $[0, 2\pi]$ is simulated to highlight the influence of the radiation pattern on the correlation coefficient value. Figure B.1 graphically depicts the concept of this analysis.

Scenario 1

Let us assume the auto-correlation function S_{11} of a Rayleigh signal s_1 recorded with a dipole having an omnidirectional radiation pattern. S_{11} represents a Bessel function. This function indicates that, for instance, at 0.4λ separation the correlation coefficient is 0. The auto correlation function S_{11} is defined as

$$S_{11}(X) = \mathbf{E}\left[s_1(t)s_1^*(t - X)\right] \ . \tag{B.1}$$

where t represents the temporal realisation of the channel wich is also related to the displacement of the MEA element and X is the spatial separation.

Scenario 2

Let us consider the Rayleigh signal s_2 recorded from a second dipole placed at 0.4λ from the first dipole. The cross-correlation S_{12} of s_1 and s_2 should give a correlation value of 0 if the radiation pattern was omnidirectional as shown in the dash lined curve. Any alteration in the correlation value due to the change in the radiation pattern would clearly be seen as shown with the solid line curve. The cross-correlation function S_{12} is defined as

$$S_{12}(X) = \mathsf{E}\left[s_1(t)s_2^*(t - X)\right] \ . \tag{B.2}$$

Figure B.2 illustrates the simulated results of the cross-correlation function of the signals received on the two elements of a MEA. Additionally, similar results are presented in Figure B.3 when a linear MEA using 0.4λ separation is simulated. Figure B.2 illustrates the differences between S_{11} to S_{14} when generated from an ideal case with omnidirectional antennas and when using the interleaved MEA. When using omnidirectional patterns, S_{11} to S_{14} can hardly be differentiated from S_{11} to S_{14} generated from the interleaved MEA.

Furthermore, Figure B.3, illustrating S_{11} to S_{14} generated from a linear MEA, highlights the impact of the squeeze in the radiation pattern and, consequently, the importance of reducing the mutual coupling effect. In view of these results, it can be concluded that the measured correlation behaviour is mainly due to the spatial separation between the elements and therefore determined by the radio channel. Consequently, the constraint in terms of omnidirectionality of the radiation pattern is fulfilled.
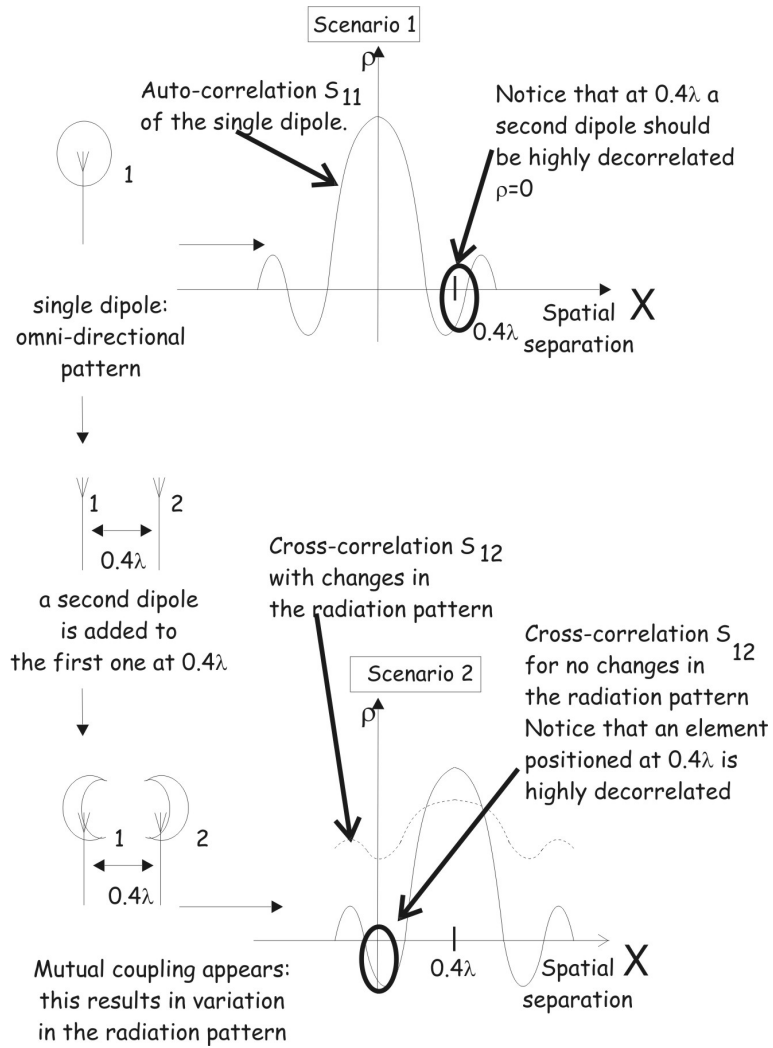
Figure B.1: *Graphical explanation of the potential influence of the radiation pattern on the correlation coefficient.*
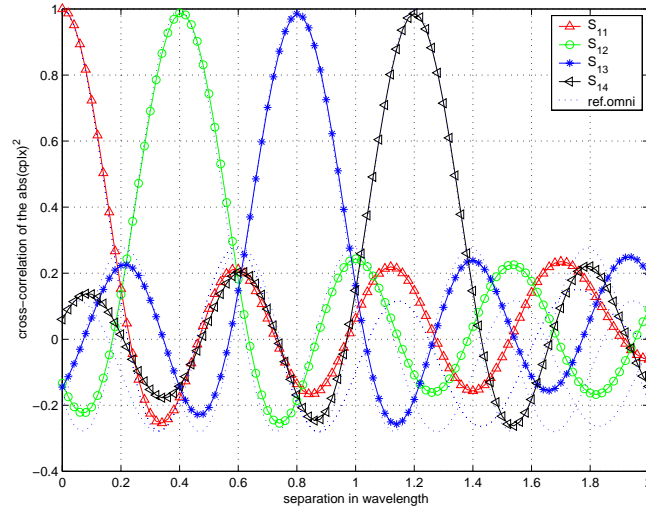
Figure B.2: Cross-correlation of the 4 elements of the interleaved MEA using Monte-Carlo simulations to show the influence of the new radiation pattern on the correlation coefficient.
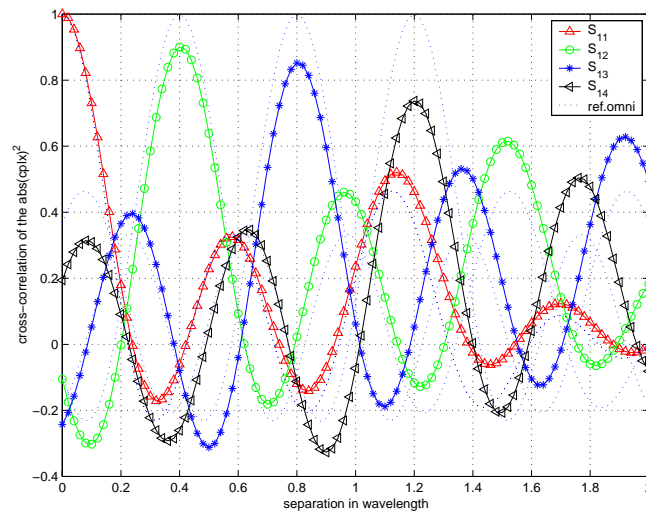
Figure B.3: Cross-correlation of the 4 elements of a linear MEA with 0.4λ separation using Monte-Carlo simulations to show the influence of the squeeze in the radiation pattern on the correlation coefficient.

Appendix C

Experimental Validation in the Polarization Domain

This appendix presents the validation procedure of the stochastic MIMO radio channel in the polarization domain. The outcome of the validation is presented in Chapter 5.

C.1 MIMO Structure Considering Polarization Diversity

The NB MIMO radio channel matrix $\mathbf{H}_{pola}$ including polarization diversity is constructed such that

$$\mathbf{H}_{pola} = \left[\begin{array}{cc} \mathbf{H}_{VV} & \mathbf{H}_{HV} \\ \mathbf{H}_{VH} & \mathbf{H}_{HH} \end{array} \right] \tag{C.1}$$

where $\mathbf{H}_{IJ}$ is a subchannel matrix considering the polarization I and J at the MS and at the BS, respectively. It is implicit that the index V represents the vertical polarization and H the horizontal polarization so $I, J \in \{H, V\}$.

$\mathbf{H}_{IJ}$ is defined as

$$\mathbf{H}_{IJ} = \left[\alpha_{I_i J_j} \right] \ i, j \in \{1, 2\} \ , \tag{C.2}$$

where $\alpha_{I_i J_j}$ is the complex NB transmission coefficient from element I_i at the MS to element J_j at the BS, as illustrated in Figure C.1. The implementation of the polarization diversity technique in the model is described in the flow chart in Figure C.2.
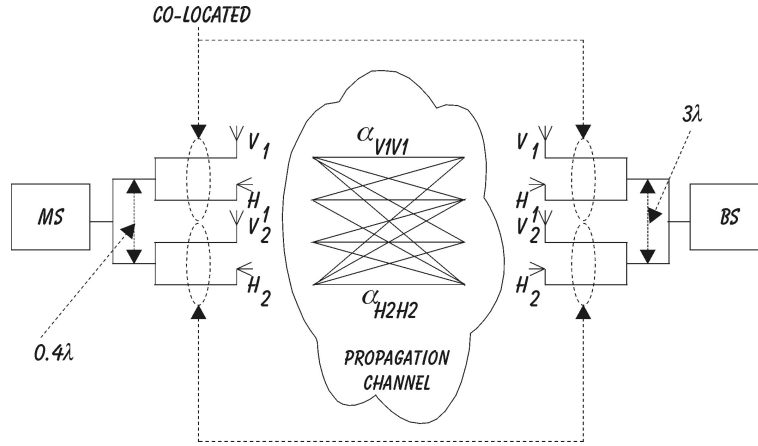
Figure C.1: Illustration of the MIMO radio channel case study considering colocated dual polarized elements.

C.2   Experimental Implementation of MIMO in the Polarization Domain

The validation of the model in the polarization domain was based on the METRA measurement data. As already mentioned in Chapter 3, at the MS, the measurement of one path was repeated using three sets of MEAs: vertical (V_{set}) , horizontal 1 (H_{set1}) and horizontal 2 (H_{set2}).
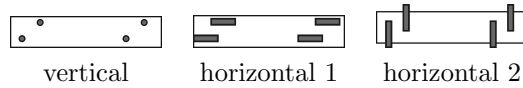
In the validation presented here, two linear MEA set-ups with 4-element each, later denoted as $Array_1$ and $Array_2$, are derived from these three measurement set, after post processing. $Array_1$ and $Array_2$ respectively combine V_{set} with H_{1set} and V_{set} with H_{2set} as shown below.

For each 4-element MEA, two dual polarized elements are colocated and the pairs are separated with 0.4λ as illustrated in Figure C.1.

At the BS, two dual polarised patch MEAs with a separation of 3λ were considered for the analysis. Recall that depending of the investigated environment, the patch MEAs were employed with different orientations.

MIMO measured   MIMO post-processed

vertical

$Array_1$

horizontal 1

vertical

$Array_2$

horizontal 2
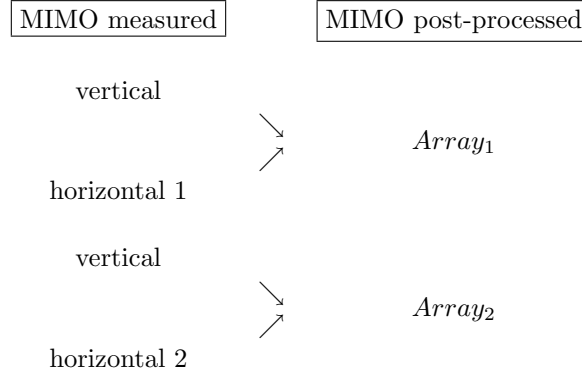
C.3 The Correlation Assumption with respect to Polarization

The correlation properties in the spatial domain of the MIMO radio channel are obtained by the Kronecker product of two independent correlation matrices defining the correlation properties at the MS and BS ends respectively. The underlying assumption of both (5.1) and (5.2) is that the correlation properties at a given end does not depend on the element used as reference at the other end, because all elements of a given end are experiencing the same power azimuth spread.

This assumption can be questioned when dual-polarized MEAs are considered. However, if the double dual-polarized set-up (dual-polarized MEAs at both ends) is split into four single-polarized MEAs, where a single polarization is considered at a time at each end, this philosophy can be applied again as explained in the following.

Therefore, the channel correlation matrix can be expressed as

$$\mathbf{R} = \left[\begin{array}{cc} \mathbf{R}_{VV} & \mathbf{R}_{HV} \\ \mathbf{R}_{VH} & \mathbf{R}_{HH} \end{array} \right] \tag{C.3}$$

where

$$\mathbf{R}_{IJ} = \left[\begin{array}{cc} \mathbf{R}_{IJ}^{ms,V} \otimes \mathbf{R}_{VV}^{bs} & \mathbf{R}_{IJ}^{ms} \otimes \mathbf{R}_{HV}^{bs} \\ \mathbf{R}_{IJ}^{ms} \otimes \mathbf{R}_{VH}^{bs} & \mathbf{R}_{IJ}^{ms,H} \otimes \mathbf{R}_{HH}^{bs} \end{array} \right] \tag{C.4}$$

with $\mathbf{R}_{IJ}^{ms,Q}$ being the matrix of the correlation coefficients $\rho_{ms,I_iJ_j}^{bs,Q_q}$ between elements I_i and J_j of the MS seen from an element of polarization Q and index q at the BS. $\mathbf{R}_{IJ}^{bs,Q}$ is equivalent at the BS. Q is omitted when the correlation coefficient mixes the polarizations at both ends.

The assumption of (5.2) mentioned earlier can be expressed as follows

$$\rho_{ms,V_iV_j}^{bs,V_q} \quad = \quad \left\langle \alpha_{V_i,V_q}, \alpha_{V_j,V_q} \right\rangle \tag{C.5}$$

$$\equiv$$

$$\rho_{ms,V_iV_j}^{bs,V_l} \quad = \quad \left\langle \alpha_{V_i,V_l}, \alpha_{V_j,V_l} \right\rangle \tag{C.6}$$

and

$$\rho_{ms,V_iV_j}^{bs,H_q} \quad = \quad \left\langle \alpha_{V_i,H_q}, \alpha_{V_j,H_q} \right\rangle \tag{C.7}$$

$$\equiv$$

$$\rho_{ms,V_iV_j}^{bs,H_l} \quad = \quad \left\langle \alpha_{V_i,H_l}, \alpha_{V_j,H_l} \right\rangle \tag{C.8}$$

Similar expressions can be written by switching the terms ms and bs in the previous relations.

At this stage, the question is whether this assumption can be extended to apply on elements differently polarized. This gives birth to two options:

- First option: *polarization-independent* definition

  Mathematically, this option leads to the following relations

  $$\rho_{ms,I_iJ_j} \quad = \quad \rho_{ms,I_iJ_j}^{bs,V_q} = \rho_{ms,I_iJ_j}^{bs,H_q} \tag{C.9}$$

  $$\rho_{bs,I_iJ_j} \quad = \quad \rho_{bs,I_iJ_j}^{ms,V_q} = \rho_{bs,I_iJ_j}^{ms,H_q} \tag{C.10}$$

  In this case, the generalised model described by relations (C.3) and (C.4) collapses to the original (5.7) since any correlation coefficient is independent of the polarization of a given reference element.

- Second option: *polarization-dependent* definition

  Such a dependency in the polarization would occur in a strong LOS situation; for instance, in the case where ideal dual polarized MEAs exhibiting high discrimination between the two polarizations are used then the correlation coefficient ρ_{II}^I between elements of similar polarization is estimated from an element which has the same polarization. A Rice type distribution occurs and therefore strong correlation exists ($\rho_{II}^I \cong 1$).
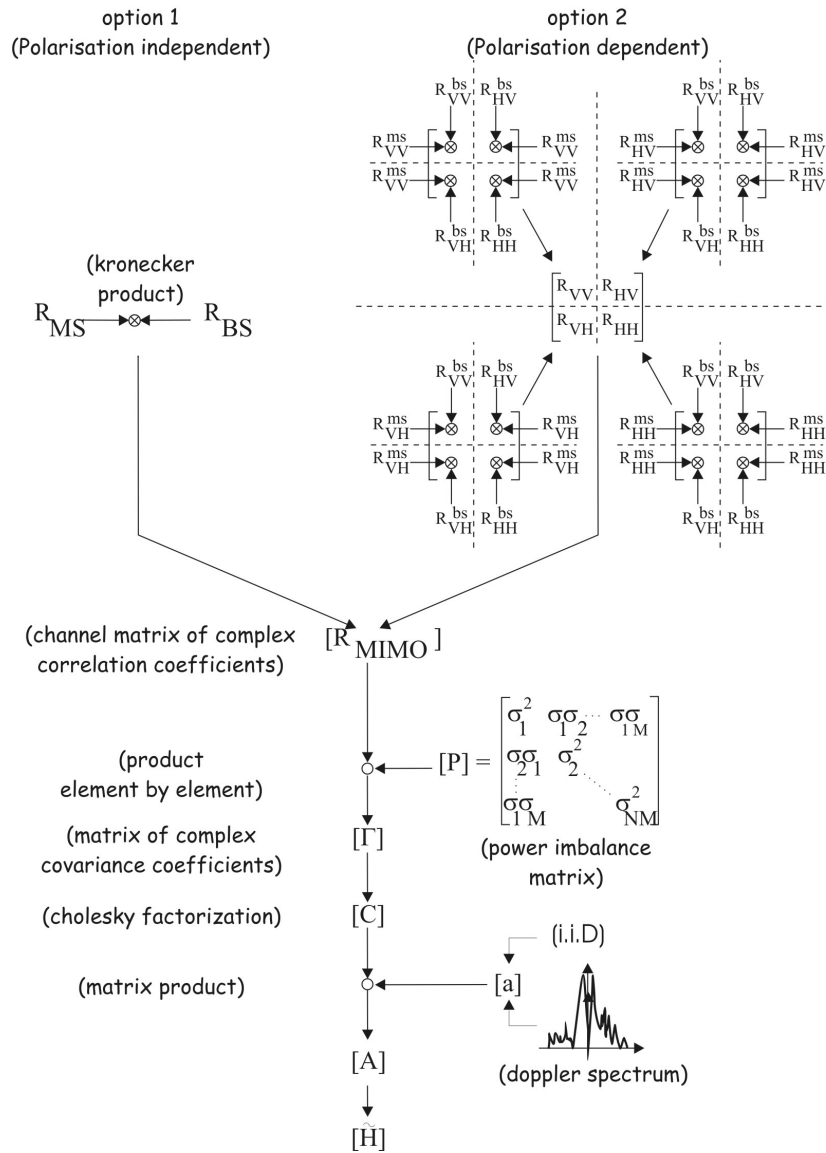
Figure C.2: Flow chart of the MIMO model considering polarization diversity.

However, in a case where the correlation coefficient is still computed between elements of same polarization, but is estimated from an element which has a different polarization, then the distribution is more of a Rayleigh type because the signal needs to be significantly scattered in order for the opposite polarized element to receive the energy from the element using another polarization. As a result, low correlation occurs ($\rho_{II}^J \to 0$).

This difference in the result, i.e., ρ_{II}^J either $\to 0$ or $\cong 1$, indicates that the correlation depends on the polarization, and (C.9) and (C.10) are thus no longer valid. Moreover, in this case, correlation coefficients ρ_{IJ} (for $I \neq J$) tend to zero as well.

Consequently, the matrix $\mathbf{R}$ would have a block structure where each block is defined as

$$\mathbf{R}_{II}^{ms,J} \otimes \mathbf{R}_{JJ}^{bs,I} \tag{C.11}$$

The rest of the model is identical to that of Section 5.2 as it is seen in Figure C.2.

C.4 Determination of the Model Option

In order to determine which option of the model to consider with respect to the METRA measurement data, the relations (C.9)-(C.10) are assessed.

The correlation coefficients $\rho_{ms}^{bs,ref}$ between the elements at the MS (or BS) have been estimated with respect to the elements (ref) at the BS (or MS). Then the difference

$$\Delta(\rho_{ms}^{bs,ref1}, \rho_{ms}^{bs,ref2}) = \rho_{ms}^{bs,ref1} - \rho_{ms}^{bs,ref2} \ , \tag{C.12}$$

has been computed and its cdf generated over all the measurement paths where the elements at the BS are $+90°/0°$ polarized. For the sake of simplicity this equation is calculated at the MS, but it is similar at the BS.

Figure C.3 presents the dependency of the correlation coefficient at the MS with respect to

- ☞ the vertical element only, i.e., $\left|\Delta\left(\rho_{ms}^{bs,V1}{}_{,v1v2}, \rho_{ms}^{bs,V2}{}_{,v1v2}\right)\right|$, (legend '○'),

- ☞ the horizontal element only, i.e., $\left|\Delta\left(\rho_{ms}^{bs,H1}{}_{,v1v2}, \rho_{ms}^{bs,H2}{}_{,v1v2}\right)\right|$, (legend '□'), and

- ☞ both the vertical and horizontal element
  at the BS, i.e., $\left|\Delta\left(\rho_{ms}^{bs,V}{}_{,v1v2}, \rho_{ms}^{bs,H}{}_{,v1v2}\right)\right|$, (legend '+').

All the cdfs exhibit a median smaller than 0.15 which is considered to be a positive result and supports the first option of the model, i.e., *polarization-independent*. This indicates that based on empirical results, the determination of the correlation

coefficient is independent of the polarization employed at the other end of the path. Therefore **option 1** is considered for evaluating the validity of the MIMO channel model in the polarization domain.

This analysis is performed with the METRA measured data which indicated a low *K-factor* (see Figure 4.2). It has not been possible to extract a path with a strong LOS which would illustrate option 2 and hence option 1 is still valid even in a LOS situation with the measured data. If high *K-factor* values had been present the conclusion could have been different.
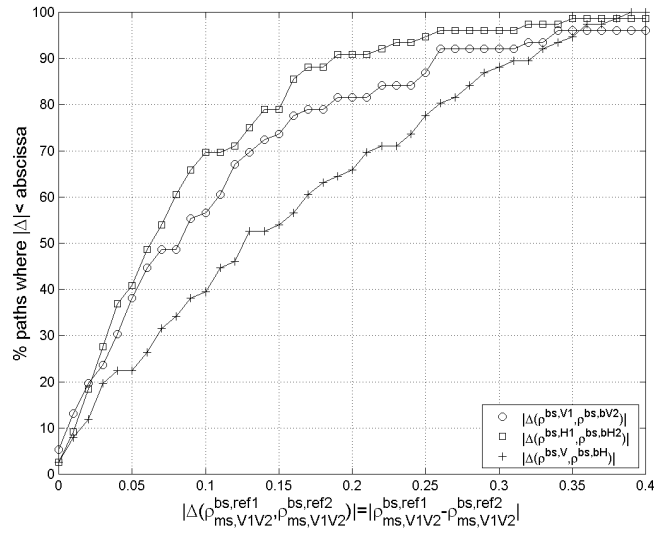
Figure C.3: *Assessment of relations (C.9)-(C.10). The cdfs present the dependency of the empirical correlation coefficient at the MS with respect to the BS elements.*

Appendix D

The CLEAN Algorithm

As presented in Chapter 3, MIMO radio channel sounding measurements were performed. The measured WB channel IR $\alpha_{mn}^{wb}(t, \tau_l)$, as such, cannot be used for analysis since the measurement system itself influences the recorded data. The goal in this appendix is to present an algorithm which is able to remove the influence of the system from the measured information.

There exist many techniques in the literature, like SAGE (Space-Alternating Generalized EM) [145] [5] based on the EM (Expectation Maximization) algorithm[146]. This algorithm works well, but entails a certain complexity. A simple algorithm called CLEAN, originally developed for processing astronomical images [112], has been used to estimate the dispersion of the radio channel [113] and [114]. The simplicity of the algorithm renders it attractive, but however with a limited temporal resolution [114].

The main philosophy behind the algorithm is that it subtracts iteratively the measured data from the known measurement equipment IR obtained by a *back-to-back* measurement $\alpha_{b2b}^{wb}(t, \tau_l)$. In order to keep the reading simple, the explicit time and delay (t, τ_l) dependencies are dropped.

The following are the steps of the algorithm in the data processing:

① Begin *iteration*

② Find the max of the measured IR α_{mn}^{wb}, $\alpha_{mn}^{max} = max(|\alpha_{mn}^{wb}|)$, where $max(.)$ gives the maximum value of the argument.

③ Align α_{b2b}^{max}, i.e., $max(|\alpha_{b2b}^{wb}|)$, to α_{mn}^{max}

④ Scale the amplitude and phase of α_{b2b}^{wb} to α_{mn}^{wb}, $scale = |\alpha_{mn}^{max}|e^{j\phi_{mn}^{max}}/|\alpha_{b2b}^{max}|e^{j\phi_{b2b}^{max}}$

⑤ Apply $\alpha_{mn}^{wb} - (\alpha_{b2b}^{wb}.scale)$ in the complex domain; as a consequence, one tap disappears.

⑥ Repeat the *iteration* until all the taps of the IR, 10 dB above the noise level, are found.

To understand and assess the quality of the CLEAN process, its limitation can be considered by using a well defined IR sequence, i.e., an IR which is constructed from the *back-to-back* measurement at different delay instants. From this known IR, it is possible to assess the quality of the CLEAN algorithm by computing the RMS of the relative error, σ_{error}, between the reconstructed IR and the original known IR. The RMS of the relative error σ_{error} is defined as

$$\sigma_{error} = \sqrt{\frac{1}{L} \sum_{l=1}^{L} \left(\frac{\alpha_l^{original} - \alpha_l^{reconstructed}}{\alpha_l^{original}} \right)^2} \, , \tag{D.1}$$

where l is the index of L discrete delays at the resolution of the measurement system, so that the lower σ_{error}, the better the estimation of the CLEAN algorithm.

As an example, a three tap IR profile with random complex amplitute and phase is generated, each tap being convolved by the *back-to-back* IR.

The RMS of the relative error is plotted in Figure D.1 and Figure D.2, for the case where the second tap is being shifted to the first tap from 1 to 4 samples. The limitation of the CLEAN algorithm is reached when a 1 or 2 sample distance exists between any two taps as shown in Figures D.1 (i) and D.1 (ii). The greater the tap separation compared to the resolution of the system, the lower the error in the CLEAN estimation as shown in Figures D.2 (i) and D.2 (ii). This is not surprising since the resolution of the measurement system is too low.

In conclusion, when the separation between 2 taps is higher than 2 samples the CLEAN algorithm provides good results, but otherwise the CLEAN algorithm is unreliable and should not be used.
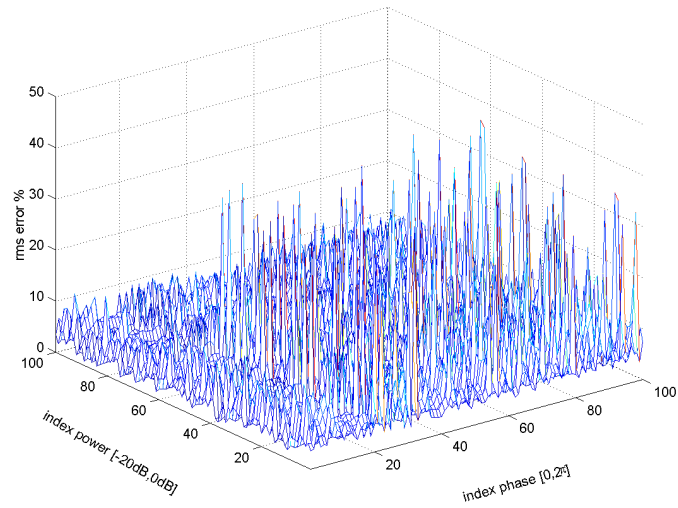
(i) 1 sample.
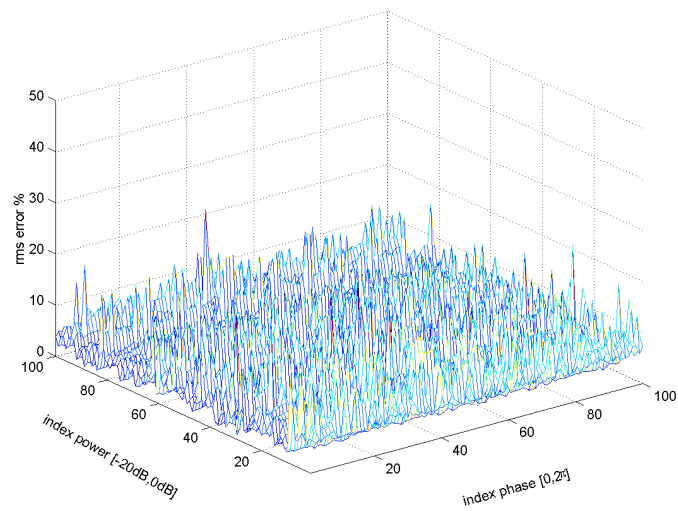
(ii) 2 samples.

Figure D.1: *RMS of the relative error plotted for different separation between the 1st and 2nd tap of a 3-tap complex channel IR profile.*
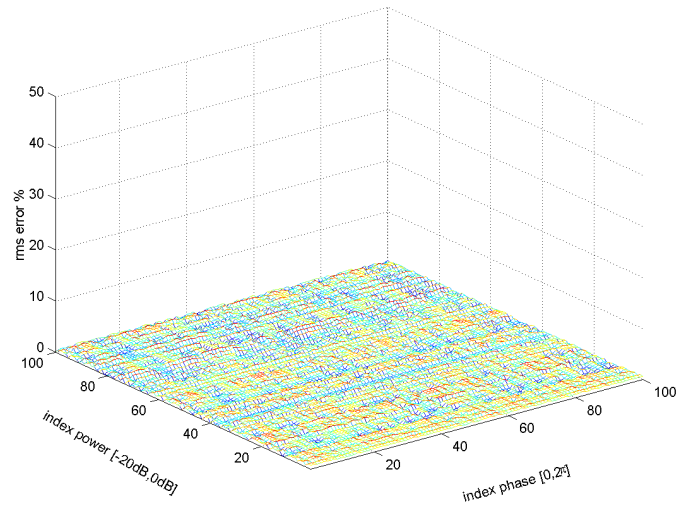
(i) 3 samples.
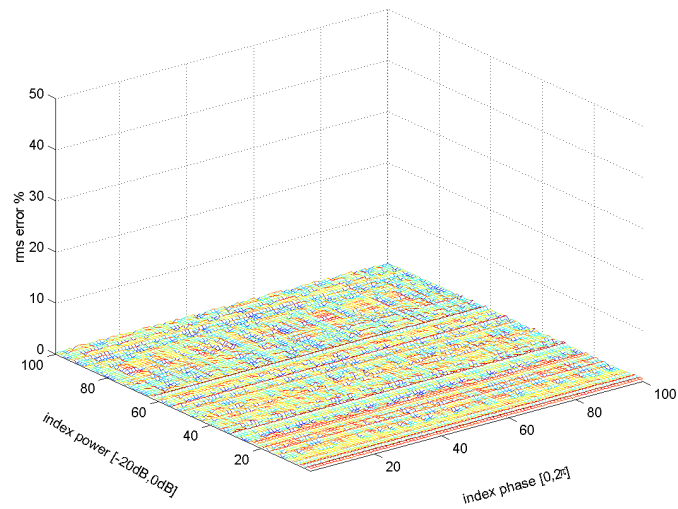
(ii) 4 samples.

Figure D.2: RMS of the relative error plotted for different separation between the 1st and 2nd tap of a 3-tap complex channel IR profile.

Appendix E

Extraction of the RMS Delay Spread

The measured WB channel $\alpha_{mn}^{wb}(t, \tau_l)$ data was recorded over the time and delay domains. The RMS delay spread, defined as the second central moment of the delay variable, is a well accepted measure of the channel time dispersion. The RMS delay spread $\sigma_{[X\ dB]}$ considers the delay range where the channel response is within $X\ dB$ of the peak value of the measured power delay profile. Its extraction based on [147, p. 205] is described below:

① The measured power IR between the mth antenna at the BS and the nth antenna at the MS, $|\alpha_{mn}^{wb}(t, \tau_l)|^2$, is first averaged over time to obtain $|\alpha_{mn\ mean}^{wb}(\tau_l)|^2$.

② Any recorded signal below $X\ dB$ of the maximum value of the measured average IR is disregarded for the estimation of the RMS delay spread $\sigma_{[X\ dB]}$.

③ The following calculation is applied to the average IR to obtain $\sigma_{[X\ dB]}$.

$$\tau_a = \frac{\sum\limits_{l=1}^{L} \tau_l |\alpha_{mn\ mean}^{wb}(\tau_l)|^2}{\sum\limits_{l=1}^{L} |\alpha_{mn\ mean}^{wb}(\tau_l)|^2}, \tag{E.1}$$

$$\sigma_{[X\ dB]} = \sqrt{\frac{\sum\limits_{l=1}^{L} (\tau_l - \tau_a)^2 |\alpha_{mn\ mean}^{wb}(\tau_l)|^2}{\sum\limits_{l=1}^{L} |\alpha_{mn\ mean}^{wb}(\tau_l)|^2}}, \tag{E.2}$$

where l is the index of L discrete delays at the resolution of the measurement system, τ_l is the delay value at index l, and τ_a is the average delay.

In a statistical characterisation, the RMS delay spread computation is repeated for all the measurement paths. For simplicity in reading the manuscript in Section 4.1 on page 50, $\sigma_{[X\ dB]}$ is referred to simply as $\sigma_{measured}$. Depending on the SNR of each measured data the threshold $X\ dB$ was choosen arbitraly.

Appendix F

Determination of the K-factor

The method used to estimate the K-factor is the one presented in [120]. In order to obtain the necessary amount of statistic to extract the K-factor, a 4×4 MEA topology is considered so that 16 measured envelopes are used to obtain the K-factor of one path. The method applied to the measured data is enumerated below.

① The received complex NB signal α_{mn}, of each of the 16 radio links, is normalized to its respective mean value m_{mn} so that the statistical nature of the measured path is not affected by a change in the mean value between the 16 sets of variables so that

$$m_{mn} = \frac{1}{T} \sum_{t=1}^{T} |\alpha_{mn}(t)| \ , \tag{F.1}$$

where T is the number of temporal realisations of the channel, then

$$\alpha_{mn}^{norm} = \frac{\alpha_{mn}}{m_{mn}} \ . \tag{F.2}$$

② All the α_{mn}^{norm} are grouped in one vector so that

$$\mathbf{V}^{norm} = \{|\alpha_{mn}^{norm}|^2\} \ . \tag{F.3}$$

③ The average of $\mathbf{V}^{norm}(t)$ is expressed as

$$G_a = \frac{1}{(16 \times T)} \sum_{t=1}^{16 \times T} V^{norm}(t) \tag{F.4}$$

④ The RMS fluctuation of $\mathbf{V}^{norm}$ about G_a is estimated so that

$$G_v = \sqrt{\frac{1}{(16 \times T)} \sum_{t=1}^{16 \times T} \left(V^{norm}(t) - G_a\right)^2}$$

(F.5)

⑤ The estimation of the *K-factor* is derived from

$$K = \frac{\sqrt{G_a^2 - G_v^2}}{G_a - \sqrt{G_a^2 - G_v^2}}$$

(F.6)

Appendix G

Correlation Results

G.1 Complex vs. Power Domain

The MIMO measurement data give the opportunity to consider the difference between three definitions of correlation coefficients: $|\rho_{env}|$, $|\rho_{pow}|$ and $|\rho_{cpx}|^2$.

The analysis is performed for both picocell and microcell environments. Figures G.1 presents the results of the investigation of the three correlation coefficient analyses. It consists of plotting the scatter diagrams of the different correlations with respect to their definition bases, i.e., $|\rho_{env}|$ vs. $|\rho_{pow}|$ and $|\rho_{env}|$ vs. $|\rho_{cplx}|^2$.

The analyses considers the computation of the correlation coefficient for vertical dipoles at the MS and at the BS only so that they exhibit the same omnidirectional radiation pattern. The knowledge of the *K-factor* is useful to classify the measurement correlation coefficient results, i.e., *K-factor* ≤ 2 and *K-factor* $\in [2, 6]$.

The Total Least Square Method [148, p. 384] is used to compute the regression line from the scatter plots assuming a function of the form $y = ax$. For both picocell and microcell environments, the relation $|\rho_{env}| = |\rho_{pow}|$ is justified since the slope of the regression line is about 1 in all cases for both the MS and the BS. The relation $|\rho_{pow}| = |\rho_{cplx}|^2$ is also justified in the situation where *K-factor* ≤ 2 for both picocell and microcell which is in agreement with [98] because the signal is considered Rayleigh distributed (see Section 2.7 on page 23).

When *K-factor* $\in [2, 6]$, the conclusion is different when the power correlation coefficient is directly taken from the square of the complex correlation and the *K-factor* is no considered (see equation (2.34) on page 24). A slight change appears in the picocell, i.e., 40% error for $|\rho_{cpx}|^2$ with respect to ρ_{pow}, at both the MS and BS as shown in Figures G.1 (v) and G.1 (vi) respectively. A more drastic change is noticeable for microcell, at the MS 80% error is seen in Figure G.1 (vii) at the MS while at the BS

(i) MS, *K-factor* ≤ 1, picocell.

(ii) BS, *K-factor* ≤ 1, picocell.

(iii) MS, *K-factor* ≤ 1, microcell.

(iv) BS, *K-factor* ≤ 1, microcell.

(v) MS, *K-factor* ∈ [2, 6], picocell.

(vi) BS, *K-factor* ∈ [2, 6], picocell.

(vii) MS, *K-factor* ∈ [2, 6], microcell.

(viii) BS, *K-factor* ∈ [2, 6], microcell.
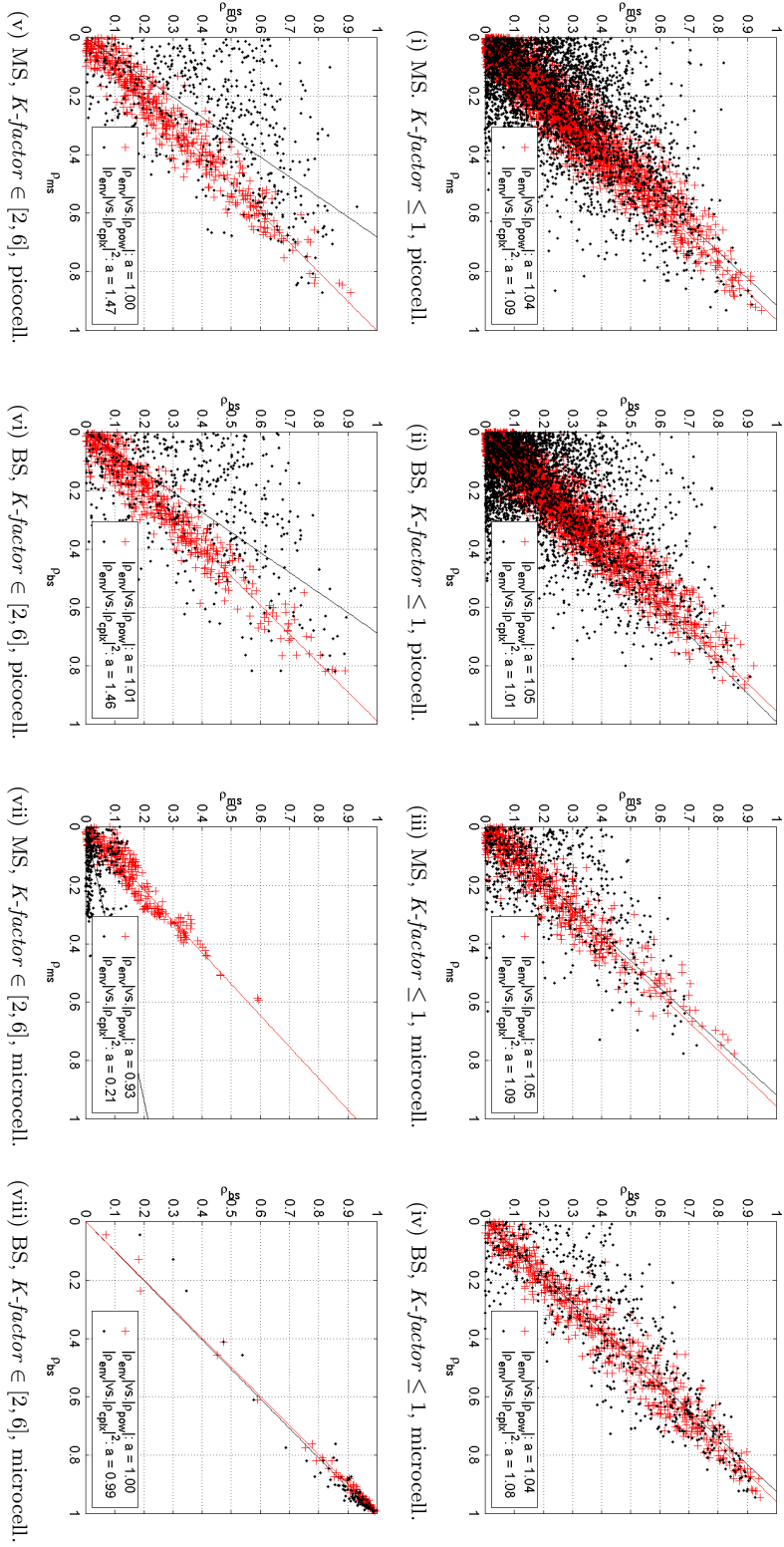
Figure G.1: $|\rho_{env}|$ Vs. $|\rho_{pow}|$ and $|\rho_{env}|$ Vs. $|\rho_{cplx}|^2$

there is a perfect match between $|\rho_{cpx}|^2$ and ρ_{pow} as seen in Figure G.1 (viii).

G.2 Spatial Domain

The empirical cdf of $\rho_{spatial\Delta}$ is performed for each of the 7 environments considering their respective number of paths. An example of the correlation coefficient for the picocell environment novi2 investigated during the METRA project is presented in Figure G.2.
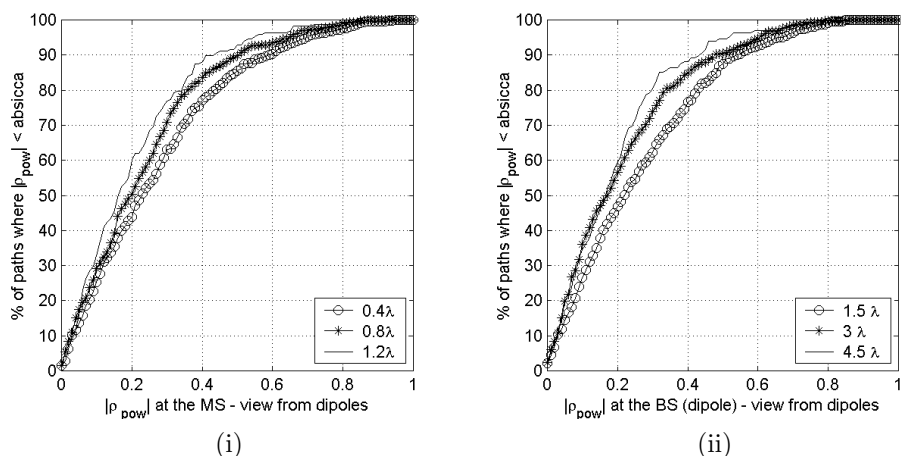
Figure G.2: Empirical cdf of the spatial power correlation coefficient for picocell novi2.

The results of the correlation analysis undertaken for all the investigated environments using the SUNBEAM and METRA measurement set-up are summarized in Table G.1 and in Table G.2 respectively. The tables present the correlation coefficient at 50% and 90% cdf level. These results are extracted in the same manner as in Figure G.2 for instance. As an example, for the first row/first column of Table G.1, "at 50% of the measurement paths the correlation coefficient at the MS is less than 0.14 for an antenna separation of 0.5λ". The spatial correlation coefficient is rather low at the MS and almost independent of the antenna spacing used.

cell	Environment	Percentage level	ant. sep. at the MS			ant. sep. at the BS		
			0.5λ	1λ	1.5λ	0.4λ	0.8λ	1.2λ
Microcell	novi2	50%	0.14	0.12	0.1	0.96	0.93	0.89
		90%	0.3	0.3	0.24	0.98	0.96	0.95

Table G.1: Summary of the percentile spatial correlation coefficient. SUNBEAM measurement set-up.

Cell	Environ ment	Percentage level	ant. sep. at the MS			ant. sep. at the BS		
			0.4λ	0.8λ	1.2λ	1.5λ	3.0λ	4.5λ
picocell	novi2	50%	0.21	0.2	0.19	0.2	0.18	0.18
		90%	0.59	0.5	0.4	0.58	0.5	0.45
	novi3	50%	0.2	0.18	0.18	0.19	0.2	0.18
		90%	0.6	0.45	0.4	0.55	0.4	0.4
	nokia	50%	0.2	0.2	0.2	0.18	0.18	0.18
		90%	0.5	0.4	0.5	0.4	0.4	0.4
	fb7b2	50%	0.18	0.18	0.18	0.25	0.2	0.2
		90%	0.45	0.4	0.4	0.6	0.5	0.5
	airport	50%	0.35	0.2	0.3	0.18	0.18	0.18
		90%	0.6	0.55	0.5	0.5	0.4	0.4
microcell	frb7 courtyard	50%	0.18	0.19	0.2	0.35	0.2	0.2
		90%	0.45	0.4	0.4	0.7	0.6	0.6
	frb7 parking	50%	0.2	0.2	0.2	0.6	0.3	0.3
		90%	0.5	0.4	0.4	0.7	0.7	0.7

Table G.2: Summary of the percentile spatial correlation coefficient. METRA measurement set-up.

Environment	Antenna orientation	Δ	Outage level	ρ_P	$\rho_{P\&S_\Delta}$	ρ_{S_Δ} (V)	ρ_{S_Δ} (H)
Picocell	$\pm45°$	3λ	50%	0.45	0.15	0.15	0.15
			90%	0.77	0.45	0.45	0.45
	$+90°/0°$	3λ	50%	0.15	0.15	0.2	0.2
			90%	0.4	0.4	0.5	0.5
Microcell (METRA)	$+90°/0°$	3λ	50%	0.13	0.13	0.4	0.4
			90%	0.4	0.4	0.7	0.75
Microcell (SUNBEAM)	$\pm45°$	1.5λ	50%	0.3	0.3	0.96	0.96
		3λ		0.3	0.3	0.93	0.92
		4.5λ		0.3	0.3	0.89	0.84
		1.5λ	90%	0.57	0.57	0.98	0.98
		3λ		0.57	0.57	0.96	0.97
		4.5λ		0.57	0.57	0.94	0.97

Table G.3: Summary of the different percentile correlation coefficient between at the BS for picocell and microcell environments.

G.3 Polarization, Joint Spatial-Polarization and Joint Pattern-Spatial-Polarization Domain

Table G.3 presents a summary of the value extracted from Figure 4.17 for picocell environment and Figure 4.18 for 50% and 90% of the cdf level.

The picocell results emphasize that the use of polarization diversity gives two degree of correlation depending of the orientation of the patch MEA. Measured data indicates that at 90% of the measurement paths a $\pm 45°$ MEA set-up could lead to a higher correlation value than for a $+90°/0°$ MEA set-up. However the $+90°/0°$ MEA set-up results in an unbalance BPR.

For picocell and microcell environment, the use of joint spatial-polarization diversity provide low correlation value as shown in Table G.3.

G.4 Joint Spatial-Polarization Properties

Having the measured data available, it is interesting to consider the relationship existing between $|\rho_{S_{\Delta i}}|$ and $|\rho_P|$ as was first done in [132] for the microcell scenario.

Figure G.3 (i) and (ii) represent the scatter diagrams where $|\rho_{S_{\Delta i}+P}|$ is plotted from both theoretical and empirical perspective. The correlation value are the results of an averaging over the number of reference elements. Figure G.3 (i) represents the picocell and Figure G.3 (ii) presents results for the microcell environment, the latter based on the SUNBEAM measurements. The theoretical values are obtained from the equation defined in [132] such that

$$|\rho_{S_{\Delta i}+P}| = |\rho_{S_{\Delta_i}}|.|\rho_P|$$

The diagonal line (regression line of one) represents the case where this equation is justified. The Total Least Square Method is used to compute the regression line from the scatter plots assuming a function of the form $y = ax$.

In the case of the picocell METRA measured data, the scattering medium is extremely complex and subsequently the individual spatial and polarization correlations are already low. Therefore their product provides an even lower value which results a large scatter diagram for values smaller than 0.5 and it is difficult to obtain a valuable regression line. For values higher than 0.5, the regression line is 0.7. For microcell scenarios, the scattering is more ideal to identify the spatial and polarization contribution independently. The regression lines calculated from the measured data for the different element spacing are higher than 0.9 which is in line with the work of [132].
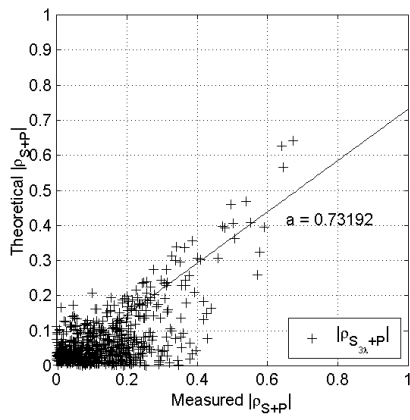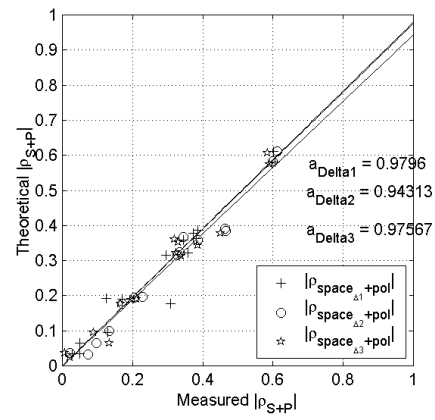
Figure G.3: Scatter diagram of the measured $|\rho_{spatial+xpol}|$ versus the theoretical $|\rho_{spatial+xpol}|$ for measurement using a $\pm 45°$ antenna patch in (i) picocell (METRA) and (ii) microcell (SUNBEAM).

Appendix H

The Beamforming Algorithm Applied to Square MEA

When a signal impinges the antenna elements under a certain angle θ, signal replicas exhibit phase differences from element to element. Considering the phase reference at the center of the MEA, the phase shift $\phi_m(t)$ between the element m of the square MEA and the reference can be expressed as

$$\phi_m(t) = \frac{2\pi d_m}{\lambda} sin\left[\theta(t)\right] \ , \tag{H.1}$$

where $\frac{d_m}{\lambda}$ is the normalized element distance from the phase center of the MEA to the array element m. Note that time, t, is directly related to the constant motion of the MEA.

The purpose of the DoA estimation is to find a steering matrix $\mathbf{W}(t)$ such that the received power is optimized depending on the signal angle of arrival. The lines of the steering matrix are the discretisation index ψ for a scanning from 0° to 360° and the columns the steering value for each MEA M elements. The steering matrix is constructed so that

$$\mathbf{W}_{\Psi \times M} \,|\, w_{\psi,m} = e^{j2\pi \frac{dk}{\Psi} sin\left[\frac{360}{\Psi}(\psi - 1)\frac{\pi}{180}\right]} \ , \tag{H.2}$$

$\mathbf{r}(t)$ is the vector containing the complex received signals samples for each instant t and is defined as

$$\mathbf{r}(t) = [r_m(t) \,|\, m \in \{1 \dots 16\}] \ . \tag{H.3}$$

The output $y_\psi(t)$ of the Fourier beamformer is given by a linear weighted sum of received complex signals for a discretisation ψ so that

$$y_\psi(t) = \mathbf{w}_\psi^H \mathbf{r}(t) \ , \tag{H.4}$$

Therefore the instantaneous power $P_\psi(t)$ can be expressed as

$$P_\psi(t) = |y_\psi(t)|^2 \tag{H.5}$$

$$= \left|\mathbf{w}_\psi^H(t)\mathbf{r}(t)\right|^2 \tag{H.6}$$

$$= \mathbf{w}_\psi^H \mathbf{r}(t)\mathbf{r}^H(t)\mathbf{w}_\psi \ , \tag{H.7}$$

So that the DoA analysis, i.e., the power $P(\theta)(t)$ at the beamformer output, is a result of an exhaustive search and is function of a certain angle of arrival θ so that

$$DoA \Rightarrow \theta \mid \max_{w_\psi} \ \left[|y_\psi(t)|^2 \ = \ \mathbf{w}_\psi^H \mathbf{r}(t)\mathbf{r}^H(t)\mathbf{w}_\psi\right] \ . \tag{H.8}$$

Bibliography

[1] *http://www.ahajokes.com/.*

[2] *http://www.umts-forum.org/.*

[3] *http://www.wlana.org/.*

[4] Sir William Stewart (chairman), *Mobile Phones and Health*, Independent Expert Group on Mobile Phones, 2000.

[5] K.I. Pedersen, *Antenna Arrays in Mobile Communications: Channel Modeling and Receiver Design for DS-CDMA Systems*, Ph.D. thesis, Alborg University, Denmark, 2000.

[6] R.B. Ertel, P. Cardieri, K.W. Sowerby, T.S. Rappaport, and J.H. Reed, "Overview of Spatial Channel Models for Antenna Array Communication Systems", *IEEE Personal Communications*, pp. 10–22, February 1998.

[7] H. Holma and A. Toskala, *WCDMA for UMTS Radio Access for Third Generation Mobile Communications*, Revised Edition, John Wiley & Sons, LTD., 2001.

[8] I.E. Telatar, "Capacity of Multi-Antenna Gaussian Channels", *AT&T-Bell Labs Internal Tech. Memo. (see http://mars.bell-labs.com/cm/ms/what/mars/index.html)*, June 1995.

[9] *http://www.ist-metra.org/.*

[10] Nokia, "MIMO Channels Model for Link-Level Simulations using Correlated Antennas", *Tech. Rep. 3GPP TSG R1-01-0260*, 2001.

[11] Nokia, "Discussion on the MIMO Channel Model", *Tech. Rep. 3GPP TSG R1-01-0702*, 2001.

[12] *http://www.3gpp.org/.*

[13] Lucent, Nokia, Siemens, and Ericsson, "A Standardized Set of MIMO Radio Propagation Channels", *Tech. Rep. 3GPP TSG R1-01-1179*, 2001.

[14] *http://www.ist-imetra.org/.*

[15] G.J. Foschini, "Layered Space-Time Architecture for Wireless Communication in a Fading Environment When Using Multi-Element Antennas", *Bell Labs Technical Journal*, vol. 1, no. 2, pp. 41–59, Autumn 1996.

[16] G.G. Raleigh and J.M. Cioffi, "Spatio-Temporal Coding for Wireless Communication", *IEEE Transactions on Communications*, vol. 46, no. 3, pp. 357–366, March 1998.

[17] J.B. Andersen, "Array Gain and Capacity for Known Random Channels with Multiple Element Arrays at Both Ends", *IEEE Journal on Selected Areas in Communications-Wireless Communication Series*, vol. 18, no. 11, pp. 2172–2178, 2000.

[18] G.D. Golden, C.J. Foschini, R.A. Valenzuela, and P.W. Wolniansky, "Detection Algorithm and Initial Laboratory Results Using V-BLAST Space-Time Communication Architecture", *Electronics Letters*, vol. 35, no. 1, pp. 14–16, January 1999.

[19] L. Schumacher, L. T. Berger, and J. Ramiro-Moreno, "Recent Advances in Propagation Characterisation and Multiple Antenna Processing in the 3GPP Framework", *accepted for publication in URSI*, 2002.

[20] J.P. Kermoal, L. Schumacher, K.I. Pedersen, P.E. Mogensen, and F. Frederiksen, "A Stochastic MIMO Radio Channel Model with Experimental Validation", *Accepted for publication in the IEEE J. Select. Areas Commun.*, August 2002.

[21] L. Hérault, "Final project report", *tech. rep., European IST-1999-10741, Project ASILUM*, March. 2002.

[22] T. Zwick, D. Hampicke, J. Maurer, A. Richter, G. Sommerkorn, R.S. Thomä, and W. Wiesbeck, "Results of double-directional channel sounding measurements", *IEEE 51st Vehicular Technology Conference Proceedings, VTC 2000-Spring Tokyo*, vol. 3, pp. 2497 –2501, 2000.

[23] M. Steinbauer, A.F. Molisch, and E. Bonek, "The Double-Directional Radio Channel", *IEEE Antennas and Propagation Magazine*, vol. 43, no. 4, pp. 51–63, August 2001.

[24] R. Stridh and B. Ottersten, "Spatial Characterization of Indoor Radio Channel Measurements at 5 GHz", *in Proceedingsof First IEEE Sensor Array and Multichannel Signal Processing Workshop, Boston, MA, USA*, March 2000.

[25] D.P. McNamara, M.A. Beach, P. Karlsson, and P.N. Fletcher, "Initial characterisation of multiple-input multiple-output (MIMO) channels for space-time communication", *in Proceedings of 4th European Personal Mobile Communications Conference EPMCC 2001, Vienna, Austria*, Feb. 2001.

[26] Motorola, "Correlation Measurements: Variability, Wide Band and Narrow Band Effects", *Tech. Rep. 3GPP TSG R1-01-0919*, 2001.

[27] Motorola, "Propagation Modeling for Multi-Antenna Simulations", *Tech. Rep. 3GPP TSG R1-01-1221*, Nov. 2001.

[28] S. Mayrargue (Editor), "Smart Antennas IST Cluster-Year 2000 Report version 2", *IST Mobile Communications Summit 2001*, 9-12 September 2001, http://quadromsl.com/mcs2001/congreso.nsf.

[29] C.C. Martin, J.H. Winters, and N.R. Sollenberger, "Multiple-input multiple-output (MIMO) radio channel measurements", *IEEE-VTS 52nd Fall VTC Vehicular Technology Conference*, vol. 2, pp. 774 –779, 2000.

[30] P. Kyritsi and D.C. Cox, "Propagation characteristics of horizontally and vertically polarized electric fields in an indoor environment: simple model and results", *IEEE VTS 54th Vehicular Technology Conference. VTC 2001 Fall.*, vol. 3, pp. 1422–1426, 2001.

[31] J. Kivinen, P. Suvikunnas, D. Perez, C. Herrero, K. Kalliola, and P. Vainikainen, "Characterisation System for MIMO channels", *in Proceedings of 4th International Symposium on Wireless Personal Multimedia Communications WPMC'01*, September 2001.

[32] Qualcomm, "MIMO Channel Measurement Results", *Tech. Rep. 3GPP TSG R1-01-1305*, 2001.

[33] *http://www.ist-saturn.org/.*

[34] *http://www.ist-asilum.org/.*

[35] D.P. McNamara, M.A. Beach, and P.N. Fletcher, "Experimental investigation of the temporal variation of MIMO channels", *Vehicular Technology Conference, VTC 2001 Fall. IEEE VTS 54th*, vol. 2, 2001.

[36] M.A. Beach, D.P. McNamara, P.N. Fletcher, and P. Karlsson, "MIMO-a solution for advanced wireless access?", *IEE Conf. Publ. Eleventh International Conference on Antennas and Propagation*, vol. 1, no. 480, 2001.

[37] P. Laspougeas, P. Pajusco, and J.-C. Bic, "Radio propagation in urban small cells environment at 2 GHz: experimental spatio-temporal characterization and spatial wideband channel model", *IEEE-VTS Fall VTC Vehicular Technology Conference*, vol. 2, 2000.

[38] R. Stridh, B. Ottersten, and P. Karlsson, "MIMO channel capacity of a measured indoor radio channel at 5.8 GHz", *Conference on Signals, Systems and Computers*, vol. 1, 2000.

[39] E. Zollinger (editor), "Wideband Directional Channel Model And Measurement Campaign", *IST-1999-10741 Deliverable 2.1*, 2000, www.ist-asilum.org.

[40] A.F. Molisch, M. Steinbauer, M. Toeltsch, E. Bonek, and R.S. Thomä, "Capacity of MIMO systems based on measured wireless channels", *IEEE Journal on Selected Areas in Communications*, vol. 20, no. 3, pp. 561–569, April 2002.

[41] M. Steinbauer, A.F. Molisch, A. Burr, and R. Thoma, "MIMO Channel Capacity Based on Measurement results", *European conference on Wireless Technology ECWT2000*, pp. 52–55, October 2000.

[42] T. Neubauer and P. C. F. Eggers, "Simultaneous Characterization of Polarization Matrix Components in Pico Cells", *Vehicular Technology Conference. VTC 1999 - Fall*, vol. 3, pp. 1361–1365, september 1999.

[43] P.C.F. Eggers, I.Z. Kovács, K. Olesen, and G.Kuijpers, "Measurements of wideband multi-element transmit-receive diversity channels in the UMTS-band", *Vehicular Technology Conference, VTC 2000 - Fall*, vol. 4, pp. 1683–1689, 2000.

[44] W.A. Th. Kotterman, G.F. Pedersen, K. Olesen, and P. Eggers, "Correlation properties for radio channels from multiple base stations to two antennas on a small handheld terminal", *Vehicular Technology Conference. VTC 2002 - Fall.*, vol. 1, pp. 462–466, 2002.

[45] C.C. Martin, J.H. Winters, and N.R. Sollenberger, "MIMO radio channel measurements: performance comparison of antenna configurations", *IEEE VTS 54th VTC Fall Vehicular Technology Conference.*, vol. 2, pp. 1225–1229, October 2001, Atlantic City, NJ, USA.

[46] M.J. Gans, N. Amitay, Y. S. Yeh, H. Xu, T.C. Damen, R.A. Valenzuela, T. Sizer, R. Storz, D. Taylor, W.M. MacDonald, C. Tran, and A. Adamiecki, "Outdoor blast measurement system at 2.44 GHz: calibration and initial results", *IEEE Journal on Selected Areas in Communications*, vol. 20, no. 3, pp. 570–583, April 2002.

[47] D. Chizhik, G.J. Foschini, M.J. Gans, and R.A. Valenzuela, "Keyholes Correlations and Capacities of Multielement Transmit and Receive Antennas", *IEEE Transactions on Wireless Communications*, vol. 1, no. 2, pp. 361–368, April 2002.

[48] P. Kyritsi, *Mutiple Element Antenna Systems in an Indoor Environment*, Ph.D. thesis, Standford University, USA, 2001.

[49] P. Kyritsi, P.W. Wolniansky, and R. A. Valenzuela, "Indoor BLAST measurements", *Multiaccess, Mobility and Teletraffic for Wireless Communications, Kluwer Academic Publishers*, vol. 5, pp. 49–60, 2000.

[50] J.W. Wallace and M.A Jensen, "Measured characteristics of the MIMO wireless channel", *IEEE VTS 54th Vehicular Technology Conference,VTC 2001 Fall*, vol. 4, pp. 2038 –2042, 2001.

[51] J.W. Wallace and M.A. Jensen, "Statistical characteristics of measured MIMO wireless channel data and comparison to conventional models", *IEEE VTS 54th Vehicular Technology Conference, VTC 2001 Fall.*, vol. 2, pp. 1078 –1082, 2001.

[52] M. Stoytchev and H. Safar, "Statistics of the MIMO radio channel in indoor environments", *IEEE VTS 54th Vehicular Technology Conference. VTC 2001 Fall*, vol. 3, 2001.

[53] M.T. Ivrlač, T.P. Kurpjuhn, C. Brunner, and W. Utschick, "Efficient Use of Fading Correlations in MIMO Systems", *IEEE VTS 54th VTC Fall Vehicular Technology Conference.*, vol. 2, pp. 2763–2767, October 2001, Atlantic City, NJ, USA.

[54] Texas Instruments, "Parameters Values for the Spatial Channel Model", *Tech. Rep. 3GPP TSG R1-01-1132*, 2001.

[55] Qualcomm, "Update on MIMO Channel Measurement Results", *Tech. Rep. 3GPP TSG R1-02-0143*, 2001.

[56] K. Sakaguchi, J.-I. Takada, and K. Araki, "ANovel Architecture for MIMO Spatio-Temporal Channel Sounder", *Special Issue on Signals, Systems and Electronics Technology*, pp. 436–441, 2002.

[57] K. I. Pedersen, J.B. Andersen, J.P. Kermoal, and P. Mogensen, "A Stochastic Multiple-Input-Multiple-Output Radio Channel Model for Evaluation of Space-Time Coding Algorithms", *IEEE Vehicular Technology Conference VTC 2000 Fall, Boston, USA*, vol. 2, pp. 893–897, September 2000.

[58] G. German, Q. Spencer, L. Swindlehurst, and R. Valenzuela, "Wireless indoor channel modeling: statistical agreement of ray tracing simulations and channel sounding measurements", *Proceedings of the IEEE International Conference on Acoustics, Speech, and Signal Processing*, vol. 4, pp. 2501 –2504, 2001.

[59] A. Burr, "Evaluation of capacity of indoor wireless MIMO channel using ray tracing", *2002 International Zurich Seminar on Broadband Communications Access Transmission Networking.*, pp. 28_1 –28_6, February 2002.

[60] P.F. Driessen and G.J. Foschini, "On the Capacity Formula for Multiple Input-Multiple Output Wireless Channels: A Geometric Interpretation", *IEEE Transactions on Communications*, vol. 47, no. 2, pp. 173–176, February 1999.

[61] D.S. Shiu, G.J. Foschini, M.J. Gans, and J.M. Kahn, "Fading Correlation and Its Effects on the Capacity of Multielement Antenna Systems", *IEEE Transactions on Communications*, vol. 48, no. 3, pp. 502–513, March 2000.

[62] IMST-GmbH, "Microcell Wideband Channel Model", *Tech. Rep. 3GPP TSG R1-01-0992*, 2001.

[63] A.M. Sayeed, "Modeling and capacity of realistic spatial MIMO channels", *IEEE ICASSP'2001*, vol. 4, pp. 2489–2492, May 2001.

[64] A. Burr, "Channel Capacity Evaluation of Multi-Element Antenna Sytems Using a Spatial Channel Model", *COST 259 TD(00)006*, January 2000, Valencia, Spain.

[65] T. Svantesson, "A physical MIMO radio channel model for multi-element multi-polarized antenna systems", *IEEE VTS 54th Vehicular Technology Conference, VTC 2001 Fall*, vol. 2, pp. 1083 –1087, 2001.

[66] R.S. Thomä, D. Hampicke, A. Ritcher, and G. Sommerkorn, "Measurement and Identification of Mobile Radio Propagation Channels", *IEEE Instrumentation and Measurement Technology Conference*, pp. 1163–1170, May 2001, Budapest, Hungary.

[67] M. Stege, J. Jelitto, M. Bronzel, and G. Fettweis, "A multiple input-multiple output channel model for simulation of Tx- and Rx-diversity wireless systems", *IEEE VTC'2000 Fall Conf.*, vol. 2, pp. 833–839, September 2000.

[68] D-S. Shiu, G.J. Foschini, M.J. Gans, and J.M. Kahn, "Fading Correlation and its Effect on the Capacity of Multi-Element Antenna Systems", *IEEE International conference on Universal personal communications. ICUPC'98*, vol. 1, pp. 429–433, October 1998.

[69] Y. Kai, M. Bengtsson, B. Ottersten, D.P. McNamara, P. Karlsson, and M.A. Beach, "A Wideband Statistical Model for NLOS Indoor MIMO Channels", *IEEE Vehicular Technology Conference VTC'02 Spring*, May 2002, Birmingham, AL, USA.

[70] Lucent Technologies, "Further Link Level Results for HSDPA using Multiple Antennas", *Tech. Rep. 3GPP TSG R1-00-1386*, November 2000.

[71] D. Gesbert, H. Bölcskei, D. Gore, and A. Paulraj, "MIMO wireless channels: capacity and performance prediction", *GLOBECOM '00, IEEE Global Telecommunications Conference, San Francisco, USA, 2000*, vol. 2, pp. 1083–1088, November 27-December 1 2000.

[72] A. Sibille, "Keyholes and MIMO Channel Modelling", *COST 273 TD(01)017*, October 2001, Bologna, Italy.

[73] MIMO Rapporteur, "MIMO Discussion Summary", *Tech. Rep. 3GPP TSG R1-02-0181*, 2001.

[74] Lucent, "MIMO System Level Channel Model", *Tech. Rep. 3GPP TSG R1-02-0548*, 2002.

[75] L.M. Correia (Editor), *Wireless Flexible Personalised Communications. COST 259: European Co-operation in Mobile Radio Research*, Wiley, 2001.

[76] Lucent Technologies, "Proposal for a Unified Spatial Channel Model", *Tech. Rep. 3GPP TSG R1-01-0722*, 2001.

[77] Siemens, "Channel Model for Tx diversity Simulations using Correlated Antennas", *Tech. Rep. 3GPP TSG R1-00-1067*, 2000.

[78] *http://www.3gpp2.org/.*

[79] P. C. F. Eggers, "Angular Dispersive Mobile Radio Environments Sensed by Highly Directive Base Station Antennas", *IEEE Proc. PIMRC'95*, vol. 2, pp. 522–526, September 1995.

[80] B.H. Fleury, "First- and Second-Order Characterization of Direction Dispersion and Space Selectivity in the Radio Channel", *IEEE Transactions on Information Theory*, vol. 46, no. 6, September 2000.

[81] W. C. Y. Lee, "Effects on Correlation Between Two Mobile Radio Base-Station Antennas", *IEEE Transactions on Vehicular Technology*, vol. 22, no. 4, pp. 130–140, November 1973.

[82] F. Adachi, M.T. Feeney, A.G. Williamson, and J.D. Parsons, "Crosscorrelation Between the Envelopes of 900 MHz Signals Received at a Mobile Radio Base Station Site", *IEE Proceedings*, vol. 133, Pt. F, no. 6, pp. 506–512, October 1986.

[83] J. Salz and J.H. Winters, "Effect of Fading Correlation on Adaptive Arrays in Digital Mobile Radio", *IEEE Transactions on Vehicular Technology*, vol. 43, no. 4, pp. 1049–1057, November 1994.

[84] K.I. Pedersen, P.E. Mogensen, and B.H. Fleury, "Spatial Channel Characteristics in Outdoor Environments and their Impact on BS Antenna System Performance", *VTC'98, Ottawa, Canada*, pp. 719–724, May 1998.

[85] J. B. Andersen and K.I. Pedersen, "Angle-of-Arrival Statistics for Low Resolution Antennas", *IEEE Transactions on Antennas and Propagation*, vol. 50, no. 3, pp. 391–395, March 2002.

[86] L. Schumacher, K.I. Pedersen, and P.E. Mogensen, "From Antenna Spacing to Theoretical Capacities—Cuidelines for Simulating MIMO Systems", *Proceedings of 13th IEEE International Symposium on Personal Indoor Mobile and Radio Communications, Lisbon, Portugal*, September 2002.

[87] D. Chizhik, G.J. Foschini, and R.A. Valenzuela, "Capacities of multi-element transmit and receive antennas: Correlations and Keyholes", *Electronics Letters*, vol. 36, no. 13, pp. 1099–1100, June 22 2000.

[88] J. B. Andersen, "Constraints and Possibilities of Adaptive Antennas for Wireless Broadband", *Proc. International Conference on Antennas and Propagation, ICAP, Manchester, UK*, vol. 1, pp. 220–225, April 2001.

[89] J.B. Andersen, "Antenna Arrays in Mobile Communications - Gain, Diversity, and Channel Capacity", *IEEE Antennas and Propagation Magazine*, vol. 42, no. 2, pp. 12–16, April 2000.

[90] C.E. Shannon, "Communication in the Presence of Noise", *Proceedings of the IRE and waves and electrons*, pp. 10–21, January 1949.

[91] S. Haykin, *Communication Systems*, Prentice Hall International, third edition, 1994.

[92] P. Kyritsi, D.C. Cox, R. A. Valenzuela, and P.W. Wolniansky, "Effect of Antenna Polarization on the Capacity of a Multiple Element System in an Indoor Environment", *Accepted for publication in the IEEE J. Select. Areas Commun.*, August 2002.

[93] R.G. Vaughan, *Antenna Diversity in Landmobile Communications*, Ph.D. thesis, Alborg University, Denmark, 1985.

[94] P.C.F. Eggers, J. Toftgård, and A.M. Oprea, "Antenna Systems for Base Station Diversity in Urban Small and Micro Cells", *IEEE Journal on Select Areas in Communications*, vol. 11, no. 7, pp. 1046–1057, September 1993.

[95] Jr. W. C. Jakes, *Microwave Mobile Communications*, John Wiley and Sons, Inc, 1974.

[96] W. C. Y. Lee, *Mobile Communications Engineering*, McGraw-Hill Book Company, 1982.

[97] J.A. McFadden, "The Correlation Function of a Sine Wave Plus Noise after Extreme Clippings", *IRE Trans. on Inf. Theory*, pp. 82–83, June 1956.

[98] J.N. Pierce and S. Stein, "Multiple Diversity with Nonindependent Fading", *Proceedingsof the IRE*, pp. 89–104, January 1960.

[99] P.C.F. Eggers, "Envelope Correlation Coefficients of Rayleigh Fading Signals Corrupted by Additive Gaussian Noise", *COST 231 TD(96) 02*, 24-26 January 1996, Belfort.

[100] *http://www.era.co.uk/tsunami/tsunami2.htm/*.

[101] *http://www.project-sunbeam.org/*.

[102] J.P. Kermoal, P.E. Mogensen, S.H. Jensen, J. B. Andersen, F. Frederiksen, T. B. Sørensen, and K.I. Pedersen, "Experimental Investigation of Multipath Richness for Multi-Element Transmit and Receive Antenna Arrays", *IEEE Vehicular Technology Conference VTC 2000 Spring, Tokyo, Japan*, vol. 3, pp. 2004–2008, may 2000.

[103] J.P. Kermoal, L. schumacher, P.E. Mogensen, and K.I. Pedersen, "Experimental Investigation of Correlation Properties of MIMO Radio Channels for Indoor Picocell Scenarios", *IEEE Vehicular Technology Conference VTC 2000 Fall, Boston, USA*, vol. 1, pp. 14–21, september 2000.

[104] F. Frederiksen, P. Mogensen, K.I. Pedersen, and P. Leth-Espensen, "A "Software" Testbed for Performance Evaluation of Adaptive Antennas in FH GSM and Wideband-CDMA", *Conference Proceeding of the 3rd ACTS Mobile Communication Summit, Rhodes, Greece*, vol. 2, pp. 430–435, June 8-11 1998.

[105] J. D. Parsons, *The Mobile Radio Propagation Channel*, Pentech Press, 1992.

[106] P. Mogensen, "Preliminary Results from Short-term Measurements in Urban Area", *COST 231 TD(90)-88*, October 1990, Paris, France.

[107] P.C.F. Eggers and J.B. Andersen, "Measurements of Complex Envelopes of Mobile Scenarios at 450 MHz", *IEEE Transactions on Vehicular Technology*, vol. 38, no. 2, pp. 37–42, May 1989.

[108] C. A. Balanis, *Antenna theory*, Wiley, second edition, 1982.

[109] C. Icheln, J. Ollikainen, and P. Vainikanen, "Reducing the Influence of Feed Cables on Small Antenna Measurements", *Electronics Letters*, vol. 35, no. 15, pp. 1212–1214, 22nd July 1999.

[110] *AWAS for windows, version 1.0*, Artech House, Inc, 1995.

[111] Troels B. Sorensen, *Intelligent Distributed Antenna Systems (IDAS), Assessment by measurement and simulation*, Ph.D. thesis, Alborg University, Denmark, 2002.

[112] B.D. Jeffs and D. Elsmore, "Maximally sparse reconstruction of blurred star field images", *ICASSP-91, International Conference on Acoustics, Speech, and Signal Processing*, vol. 4, 1991.

[113] T. Korhonen, *Measuring and Estimating Instantaneous Wideband Radio Channel by Regularized Convolution*, Ph.D. thesis, Helsinki University Of Technology, Finland, 1999.

[114] Q.H. Spencer, B.D. Jeffs, M.A. Jensen, and A.L. Swindlehurst, "Modeling the Statistical Time and Angle of Arrival Characteristics of an Indoor Multipath Channel", *IEEE Journal on Selected Areas in Communications*, vol. 18, no. 3, March 2000.

[115] R.H.T. Bates and M.J. McDonnell, *Image Restoration and Reconstruction*, Claredon press, Oxford University press, 1986.

[116] P.C.F. Eggers, "Super Resolution and Deconvolution of Angular Power Spectra", *IEEE PIMRC*, pp. 801–805, Sept. 1997.

[117] A. A. M. Saleh and R. A. Valenzuela, "A Statistical Model for Indoor Multipath Propagation", *IEEE Journal on Selected areas in communications*, vol. 5, no. 2, pp. 128–137, February 1987.

[118] P. C. F. Eggers, "Internal Note on variance substraction," Tech. Rep., 1995.

[119] J. B. Andersen, T. S. Rappaport, and S. Yoshida, "Propagation Measurements and Models for Wireless Communications Channels", *IEEE Communications Magazine*, vol. 33, no. 1, pp. 42–49, January 1995.

[120] L.J. Greenstein, D.G. Michelson, and V. Erceg, "Moment-Method Estimation of the Ricean *K*-Factor", *IEEE Communications Letters*, vol. 3, no. 6, pp. 175–176, June 1999.

[121] M.B. Knudsen, *Antenna Systems for Handsets*, Ph.D. thesis, Alborg University, Denmark, 2001.

[122] R.J. Mailloux, *Phased Array Antenna Handbook*, Artech House, 1994.

[123] J. Liberti, "Measuring and Modelling Spatial Radio Channels for Systems", *Proc. 1998 IEEE Antennas and Propagation Society Int'l. Symposium, Atlanta, USA*, June 1998.

[124] K. Kalliola, *Experimental Analysis of Multidimensional Radio Channels*, Ph.D. thesis, Helsinki University, Finland, 2002.

[125] E. Hecht, *Optics*, Addison-Wesley Publishing Company, second edition, 1987.

[126] O. Nørklit, *Adaptive Antennas in Mobile Communication*, Ph.D. thesis, Alborg University, Denmark, 1996.

[127] B.D.Van Veen and K.M. Buckley, ""Beamforming: A Versatile Approach to Spatial Filtering"", *IEEE ASSP Magazine*, pp. 4–24, April 1988.

[128] H. Dam, "Smart Antennas in GSM System," M.S. thesis, Alborg University, Denmark, 1995.

[129] A.V. Oppenheim and R.W. Schafer, *Discrete-Time Signal Processing*, Prentice Hall Processing Series, 1989.

[130] E.C. Ifeachor and B.W. Jervis, *Digital Signal Processing: A Practical Approach*, Addison-Wesley Publishers Ltd., 1993.

[131] J.C. Liberti and T.S. Rappaport, *Smart Antennas for Wireless communications: IS-95 and Third Generation CDMA Applications*, Prentice Hall PTR, 1999.

[132] P.C.F. Eggers, J. Toftgård, and A.M. Oprea, "Antenna Systems for Base Station Diversity in Urban Small and Micro Cells", *IEEE Journal on Selected Areas in Communications*, vol. 11, no. 7, pp. 1046–1057, September 1993.

[133] R.B. Ertel, P. Cardieri, K.W. Sowerby, T.S. Rappaport, and J.H. Reed, "Overview of Spatial Channel Models for Antenna Array Communication Systems", *IEEE Personal Communications*, pp. 10–21, February 1998.

[134] T. Rappaport J. Liberti, "A Geometrically Based Model for Line-Of-Sight Multipath Radio Channels", *IEEE Proc. Vehicular Technology Conference (VTC96)*, May 1996.

[135] O. Nørklit and J. Bach Andersen, "Diffuse Channel Model and Experimental Results for Antenna Arrays in Mobile Environments", *IEEE Trans. on Antennas and Propagation*, vol. 46, no. 6, June 1998.

[136] K.I. Pedersen and P.E. Mogensen, "Simulation of Dual-Polarized Propagation Environments for Adaptive Antennas", *IEEE Proc. Vehicular Technology Conference, Amsterdam, Netherlands*, September 1999.

[137] L. Schumacher, J.P. Kermoal, F. Frederiksen, K.I. Pedersen, A. Algans, and P.E. Mogensen, "MIMO Channel Characterisation", *IST Project IST-1999-11729 METRA Deliverable 2*, February 1999.

[138] MIMO Rapporteur, "MIMO Conference Call Summary", *Tech. Rep. 3GPP TSG R1-02-0141*, 2001.

[139] Y. Kai, M. Bengtsson, B. Ottersten, D.P. McNamara, P. Karlsson, and M.A. Beach, "Second order statistics of NLOS indoor MIMO channels based on 5.2 GHz measurements", *IEEE Global Telecommunications Conference GLOBE-COM '01*, vol. 1, 2001.

[140] T. Klingenbrunn and P. Mogensen, "Modelling Cross-Correlated Shadowing in Network Simulations", *Proc. IEEE Vehicular Technology Conference*, September 1999.

[141] T. Klingenbrunn and P. Mogensen, "Modelling Frequency Correlation of Fast Fading in Frequency Hopping GSM Link Simulations", *Proc. IEEE Vehicular Technology Conference*, September 1999.

[142] J. G. Proakis, *Digital Communications*, Mc Graw-Hill International, third edition, 1995.

[143] T. Svantesson, "An antenna solution for MIMO channels: the multimode antenna", *ASILOMAR'2000*, vol. 2, pp. 738–742, November 2000.

[144] T. Svantesson, *Antennas and Propagation from a Signal Perspective*, Ph.D. thesis, Chalmers University of Technology, Sweden, 2001.

[145] B.H. Fleury, M. Tschudin, R. Heddergott, D. Dahlhaus, and K.I. Pedersen, "Channel Parameter Estimation in Mobile Radio Environments Using the SAGE Algorithm", *IEEE Journal on Selected Areas in Communications*, vol. 17, no. 3, March 1999.

[146] T. K. Moon, "The Expectation - Maximization Algorithm", *IEEE Signal Processing Magazine*, pp. 47–59, November 1996.

[147] M. P. M. Hall, L. W. Barclay, and M. T. Hewitt, *Propagation of Radiowaves*, The Institution of Electrical Engineers, 1996.

[148] T. K. Moon and W. C. Stirling, *Mathematical Methods and Algorithms for Signal Processing*, Prentice Hall, 2000.